Extraction of G_E^n at $Q^2 = 1$ (GeV/c)^2 from Measurements of $^3\overrightarrow{He}(\overrightarrow{e}, e')$.

Ge Jin

Chengdu, China

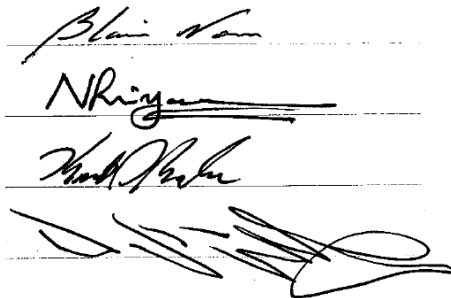M.S. Physics, University of Virginia, May 2008

B.S. Physics, Peking University, July 2005

A Thesis presented to the Graduate Faculty of

of the University of Virginia in Candidacy for the Degree of

Doctor of Philosophy

Department of Physics

University of Virginia

May 2011

JIN, GE Ph.D. April 2011. Nuclear Physics

Extraction of G_E^n at $Q^2 = 1$ (GeV/c)² from Measurements of ${}^3\overrightarrow{He}(\overrightarrow{e},e')$

Advisor of Dissertation: Blaine E. Norum

Abstract

The neutron electric form factor, G_E^n, is extracted for the first time at $Q^2 = 1$ (GeV/c)² from polarized ${}^3\overrightarrow{He}(\overrightarrow{e},e')$ measurements in Hall A at Jefferson Lab. By getting the ratio of asymmetries in longitudinal and transverse quasi-elastic ${}^3\overrightarrow{He}(\overrightarrow{e},e')$, the electric and magnetic contributions can be seperated. The proton and neutron contributions to the ${}^3He$ quasi-elastic response functions are calculated in PWIA by Salme' *et al.*, and the neutron electric form factor can be extracted. This method of inclusive scattering becomes feasible for the first time due to the falloff of the other form factors at high Q^2 while G_E^n keeps increasing in units of the dipole form factor. Approximately 20% uncertainty is achieved in the extraction largely contributed by the statistical uncertainties from 3 days of data-taking. All aspects of the measurement will be discussed in this thesis including theoretical model, experiment setup and the details in the analysis.

Acknowledgements

At the time when this thesis is about to finish, I would like to express my gratitude to many of those who gave me great help in the work of this thesis.

First, I would like to express my sincere gratitude to Professor Blaine Norum for his excellent advising and the research opportunities he gave me. I benefited a lot from his style of advising, which is to let the students find their own motivation and their ways to do research in the ocean of the national labs. From Brookhaven to JLab I was put into the labs with the local scientists, and I had to push myself to obtain knowledge from those who knew best about the local details. This attitude of seeking up information will be valuable in my life time. Another way I fully appreciate about his advising is the idea of innovation, and the preference of new physics and techniques over repeating previous attempts. He mentioned to me to look at the "shape", or trend in physics first before paying too much attention to the details of the magnitudes. It is also something I truly believe, that the "shape" is something that could lead to great discoveries. The encourage from him to work on this unprecedented method of the extraction of G_E^n examplified his ideology of scientific research. He is wise in evaluating about what to work on and how to work. He gave me great room and freedom to develop the research as I would like to and the research turned out to be successful and useful for future developments.

Second, I would like to express great gratitude to JLab Staff Scientist Doug Hig-

inbotham. Doug gave me a lot of advising in detail, and also a lot in the overall planning. For things in detail, he was once thinking about my optics calibration when taking a shower. For the overall planning, he put the effort to pursuade me and my advisor to believe that this extraction of G_E^n was feasible, something we thought impossible to do. I learned many useful tricks in the detector calibration from him. He tries to understand physics in a simple picture first before heavy calculations are involved, which is a fast and really efficient way to grasp the basic and most important ideas. The problem-solving skills I learned from him are valuable in my future career, no matter what I do.

Third, I would like to thank my student collaborators Miha Mihovilovic, Yawei Zhang and Ellie Long, and postdocs Bryan Moffit, Vince Sulkosky and Aidan Kelleher, as well as the Run Coordinators in my experiment. We worked together for the experiment, and these friends donated their biggest effort in the experiment running and its analysis. My analysis could not be finished without their effort.

I should especially thank Jin Huang for his help in many parts of my analysis. Jin Huang understands physics and software very well, and he helped me a lot with my early stage of optics calibration, and also many things in the analysis afterwards. Although he is just a graduate student like me, he taught me many greatly useful things.

Another group of people deserving my especially thanks is the Transversity Group. They set up the helium target and the BigBite Spectrometer, and ran their experi-

ment smoothly, which benefited my experiment. People in my experiment have been borrowing analysis methods and results from them. They definitely helped in the finish of the thesis.

Well, there are many people who gave me all kinds of help in the analysis. K. Slifer and D. Dutta showed me ways for my radiative correction; S. Sirca and S. Riordan have discussed with me about my G_E^n extraction; J.P. Chen hinted to me about my calibration and told me what to believe and what not to believe in data; G. Salme' gave me his theoretical research and worked with me about my extraction; Y. Qiang told me about target stuff and optics calibratino; X. Qian told me how to work on BigBite, and he influenced me by his attitude of working; many more, still thinking...

Finally, I would like to thank my wife Qiqi for her support and remarkable "impatience". Qiqi is a good girl, very good and hard to find. She was impatient because she wanted us to have a good future. It is fine, since I can be patient to finish my work. So her push helped in the finish of this thesis.

Contents

List of Tables

List of Figures

Chapter 1

Physics Motivation

1.1 Introduction

The electromagnetic form factors are very interesting topics from both theoretical and experimental perspectives. Historically, the neutron was considered a point-like particle until the measurement of its magnetic moment. It was found that protons and neutrons have magnetic moments different from point-like spin 1/2 particles. The magnetic moment μ of a point-like spin 1/2 particle is

$$\mu = g\left(\frac{e}{2m}\right)\frac{\hbar}{2} \tag{1.1}$$

where g is the the g-factor with its value close to 2 for a spin 1/2 particle, e and m are the charge and mass of the particle, respectively, and $\hbar$ is the Planck's constant divided by 2π.

Experiments determined that the proton magnetic moment is $\mu_p = 2.79\mu_N$ and the neutron magnetic moment is $\mu_n = -1.91\mu_N$. Here, $\mu_N = \frac{e\hbar}{2M_p}$ is the nuclear magneton. μ_p and μ_n are different from the classically predicted μ_N or 0, demonstrating that protons and neutrons are not point-like particles.

Electric and magnetic form factors G_E and G_M are used to describe the nucleon structure, in that they are closely related to the charge and magnetic moment distributions of a nucleon. G_E and G_M can be approximately considered as the Fourier transforms of the nucleon charge and magnetization densities when the 4-momentum transfer square Q^2 is much lower than the mass of the pion squared. Quantum Chromodynamics (QCD) can make rigorous predictions of the values of G_E and G_M at large Q^2, but it becomes problematic in the low Q^2 regime. Phenomenological models were developed to describe the data in the low energy regime.

For decades experimentalists have been actively measuring G_E and G_M of the proton and neutron using various methods. Of the all 4 nucleon form factors: G_M^p, G_M^n, G_E^n and G_E^p, the measurement of G_E^n is the most difficult due to its small value and the non-existance of free neutrons in nature. Previous methods of measuring G_E^n include the Rosenbluth separation and semi-inclusive neutron tagging (e.g. $A(e, e'n)$). Quasi-elastic inclusive measurements of the neutron electric form factor G_E^n have been tried before but they yielded uncertaintiess comparable to the extracted quantity.

The experiment described in this dissertation used the unprecedented method of a quasi-elastic inclusive $^3\vec{H}e(\vec{e}, e')$ measurement to extract G_E^n at Q^2=0.95 (GeV/c)^2.

Reasonable results were obtained within the theoretical model of the Plane Wave Impulse Approximation (PWIA). This measurement was parasitic on Jefferson Lab experiment E05102, running between April 2009 and June 2009. The extraction within PWIA is based on the calculation by G. Salme' *et al.* [4]. With meaningful physical quantities extracted a new method is discovered for future measurements.

1.2 Theoretical Background

1.2.1 Unpolarized Scattering Amplitude, Rosenbluth Formula

Following *Quarks* & *Leptons* by F. Halzen and A.D. Martin [5], the electron current density j^μ can be expressed as

$$j^\mu = -e\overline{\psi}\gamma^\mu\psi \tag{1.2}$$

where ψ is the wave function of the electron. The easiest case is *e-e* scattering, or Möller scattering, shown in fig 1.1.

The transistion amplitude written in terms of the electromagnetic current is

$$T_{fi} = -i \int j_\mu^1(x)(\frac{1}{q^2})j_2^\mu(x)d^4x \tag{1.3}$$

where $q = p_A - p_C$ is the 4-momentum transfer.

When it comes to nucleons, with their internal structure, the current density can no longer be written as eq. (1.2), which is the current density of a point-like particle.
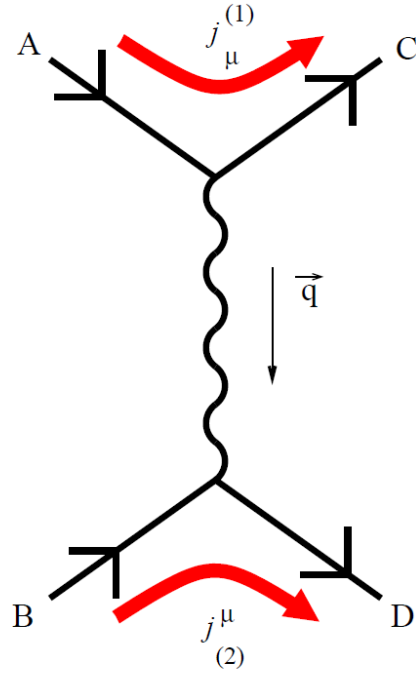
Figure 1.1: Feynman diagram of Möller scattering. Incoming electrons are A and B and outgoing electrons are C and D.

Instead, the Lorentz invariant current is

$$J^\mu = \overline{\psi}\left[F_1(q^2)\gamma^\mu + \frac{\kappa}{2M}F_2(q^2)i\sigma^{\mu\nu}q_\nu\right]\psi \tag{1.4}$$

where κ is the anomalous magnetic moment, $\sigma^{\mu\nu} = \frac{i}{2}(\gamma^\mu\gamma^\nu - \gamma^\nu\gamma^\mu)$, M is the mass of the nucleon, F_1 and F_2 are independent form factors, and the transistion amplitude

is defined as

$$T_{fi} = -i \int j_\mu^1(x)(\frac{1}{q^2})J_2^\mu(x)d^4x. \tag{1.5}$$

F_1 and F_2 are called the Dirac and Pauli form factors, respectively. When q approaches 0, the form factors behave as

$$F_1^p(q^2 = 0) = 1, F_1^n(q^2 = 0) = 0 \tag{1.6}$$

$$F_2^p(q^2 = 0) = 1, F_2^n(q^2 = 0) = 1 \tag{1.7}$$

With such nucleon currents the differential cross section for electron-nucleon scattering can be written as

$$\frac{d\sigma}{d\Omega}\bigg|_{lab} = \frac{\alpha^2}{4E^2 \sin^4 \frac{\theta}{2}} \frac{E'}{E} \left[\left(F_1^2 - \frac{\kappa^2 q^2}{4M^2}F_2^2 \right) \cos^2 \frac{\theta}{2} - \frac{q^2}{2M^2}(F_1 + \kappa F_2)^2 \sin^2 \frac{\theta}{2} \right] \tag{1.8}$$

where θ is the electron scattering angle. E and E' are the incoming and outgoing electron energy, respectively. Eq (1.8) is called the Rosenbluth formula, based on which Rosenbluth separation method is used in form factor measurements, as mentioned in the section 1.3.1. One can denote the point-like particle scattering cross section as the Mott cross section $\frac{d\sigma}{d\Omega}|_{Mott}$, e.g., $e - e$ scattering cross section, and calculation gives:

$$\frac{d\sigma}{d\Omega}\bigg|_{Mott} = \frac{\alpha^2}{4E^2 \sin^4 \frac{\theta}{2}} \tag{1.9}$$

Electromagnetic Sachs form factors, G_E and G_M, are linear combinations of F_1

and F_2:

$$G_E = F_1 + \frac{\kappa^2 q^2}{4M^2} F_2 \tag{1.10}$$

$$G_M = F_1 + \kappa F_2 \tag{1.11}$$

The new form factors allow the Rosenbluth equation (1.12) to be written as

$$\frac{d\sigma}{d\Omega}\bigg|_{lab} = \frac{d\sigma}{d\Omega}\bigg|_{Mott} \frac{E'}{E} \left[\frac{G_E^2 + \tau G_M^2}{1 + \tau} + 2\tau G_M^2 \tan^2 \frac{\theta}{2} \right] \tag{1.12}$$

where

$$\tau = -q^2/4M^2 = Q^2/4M^2 \tag{1.13}$$

and the four-momentum transfer square is defined as $Q^2 = -q^2 = -q^\mu q_\mu$.

Equation (1.12) allows the experimental separation of G_E and G_M by changing θ, the electron scattering angle, while keeping Q^2 constant, and measuring the change in cross section.

1.2.2 Polarized Scattering Amplitude

General Formulism of Asymmetry

When the target nucleon and the incident electron are both polarized, the polarization interference changes the cross section by a few percent typically. Donnelly and Raskin [6][7] developed the formalism for the double-polarization cross section. In the Born approximation, the polarized cross section is the sum of the unpolarized part Σ and

the polarized part Δ. The total helicity-dependent cross section can therefore be written as

$$\sigma = \Sigma + h\Delta \tag{1.14}$$

where $h = \pm 1$ indicates the electron helicity.

The asymmetry in the cross sections is defined as

$$A = \frac{\sigma_+ - \sigma_-}{\sigma_+ + \sigma_-} = \frac{\Delta}{\Sigma} \tag{1.15}$$

where the denominator is given by

$$\Sigma = \sigma_{Mott}(v_L R_L + v_T R_T) \tag{1.16}$$

and the numerator is given by

$$\Delta = -\sigma_{Mott}(\cos\theta^* v_{T'} R_{T'} + \sin\theta^* \cos\phi^* v_{TL'} R_{TL'}) \tag{1.17}$$

Here θ^* and ϕ^* are the azimuthal and polar angles of the target polarization vector with respect to the direction of the three-momentum transfer $\vec{q}$, as shown in fig 1.2. The R's are nuclear response functions and the v's are kinematics factors defined as:

$$v_L = \frac{Q^4}{|\vec{q}|^4} \tag{1.18}$$

$$v_T = \frac{1}{2}\frac{Q^2}{|\vec{q}\,|^2}\tan^2\frac{\theta}{2} \tag{1.19}$$

$$v_{T'} = tan\frac{\theta}{2}\sqrt{\frac{Q^2}{|\vec{q}\,|^2}+\tan^2\frac{\theta}{2}} \tag{1.20}$$

$$v_{TL'} = -\frac{1}{\sqrt{2}}\frac{Q^2}{|\vec{q}\,|^2}\tan\frac{\theta}{2}. \tag{1.21}$$
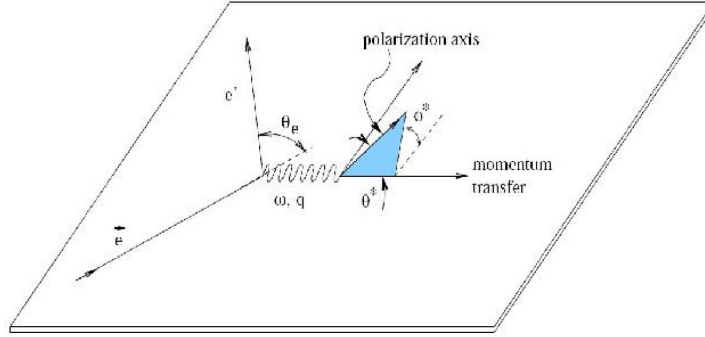
Figure 1.2: e-N scattering; target spin direction is with respect to $\vec{q}$ and the scattering plane.

Thus, the asymmetry can be expressed as

$$A = \frac{\Delta}{\Sigma} = -\frac{\cos\theta^* v_{T'}R_{T'} + \sin\theta^*\cos\phi^* v_{TL'}R_{TL'}}{v_L R_L + v_T R_T} \tag{1.22}$$

Equation (1.22) applies to composite nuclei as well as individual nucleons. When $\theta^* = 0$, the target spin is parallel to $\vec{q}$. The term with $R_{TL'}$ vanishes, leaving only $R_{T'}$ term. The corresponding asymmetry is called the transverse asymmetry, or $A_{T'}$. When $\theta^* = \pm\pi/2$, the target spin is perpendicular to $\vec{q}$. The term with $R_{T'}$ vanishes, leaving only $R_{TL'}$ term. The corresponding asymmetry is called the

transverse-longitudinal asymmetry, or $A_{TL'}$.

Nucleon Response Functions

Single nucleon response functions can be written as functions of form factors G_E and G_M

$$R_L = (1+\tau)G_E^2 \tag{1.23}$$

$$R_T = 2\tau G_M^2 \tag{1.24}$$

$$R_{T'} = 2\tau G_M^2 \tag{1.25}$$

$$R_{TL'} = 2\sqrt{2\tau(1+\tau)}G_M G_E \tag{1.26}$$

where τ is defined in eq. (1.13).

Hence, eq. (1.22) can be written as [7]

$$A = \frac{\Delta}{\Sigma} = -\frac{\cos\theta^* v_{T'} 2\tau G_M^2 + \sin\theta^* \cos\phi^* v_{TL'} 2\sqrt{2\tau(1+\tau)}G_M G_E}{v_L(1+\tau)G_E^2 + v_T 2\tau G_M^2} \tag{1.27}$$

Nuclei response functions can have forms similar to those of nucleons by replacing the nuclear mass and nuclear form factors by the nucleon masses and form factors. However, it is more complicated to express nuclear response functions as simple combinations of nucleon form factors, due to the lack of precise calculation of the Nucleon-Nucleon interaction.

1.3 Previous G_E^n Measurements

1.3.1 Rosenbluth Separation

By eq. (1.12) experimentalists can vary the beam energy and electron scattering angle θ to keep Q^2 constant, and by measuring the change of the cross section as a function of θ, they can extract the electromagnetic form factors. Equation (1.12) can be written as eq. (1.28):

$$\frac{d\sigma}{d\Omega} = \left.\frac{d\sigma}{d\Omega}\right|_{Mott} \left(A(Q^2) + B(Q^2) \tan^2 \frac{\theta}{2} \right) \tag{1.28}$$

where $A(Q^2)$ and $B(Q^2)$ are combinations of proton and neutron electromagnetic form factors.

An early experiment was performed at DESY in 1971 on a deuteron target [8]. A fit was performed to the results of this experiment, which is the well-known Galster parameterization:

$$G_E^n(Q^2) = -\frac{\mu_n \tau}{1 + 5.6\tau} G_D(Q^2) \tag{1.29}$$

where μ_n is the neutron magnetic moment and τ is defined in eq. (1.13). The dipole form factor $G_D(Q^2)$ takes the form

$$G_D(Q^2) = \frac{1}{\left(1 + \frac{Q^2}{\Lambda^2}\right)^2} \tag{1.30}$$

with $\Lambda^2 = 0.71\ (\text{GeV}/\text{c})^2$.

Platchkov improved the experiment at $0.4 < Q^2 < 18 fm^{-2}$ (197.327 MeV $=$ fm^{-1}) with estimated statistical accuracy between 2-6% [1]. However, the model-dependence (such as relativistic effects, meson exchange currents, and the deuteron wave-function) amplifies the final error to 20%. Results of this measurement are shown in fig. 1.3.
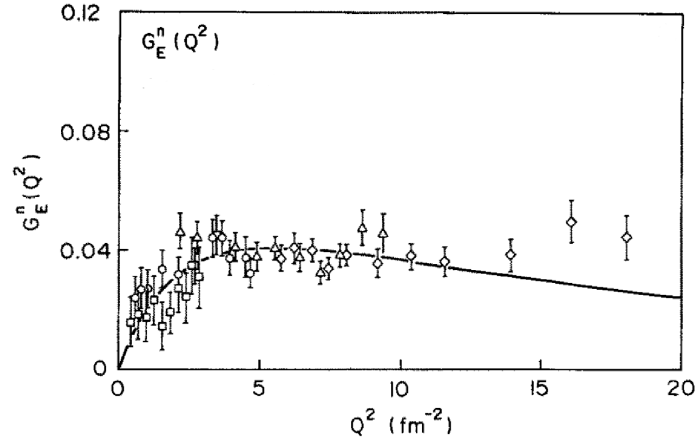
Figure 1.3: A measurement of G_E^n on a deuteron target by Platchkov *et al.* [1]. The symbols and the solid line represent the results of an analysis based upon the Paris potential, where squares, circles, triangles, and diamonds correpsond to beam energies of 200, 300, 500, and 650 MeV, respectively.

The Rosenbluth separation is very useful at lower values of Q^2 (i.e., $Q^2 < 1(GeV/c)^2$). At large Q^2 the magnetic contribution dominates both $A(Q^2)$ and $B(Q^2)$ so it becomes difficult to isolate G_E^n using only measurements of the cross section.

1.3.2   Polarization Transfer

The polarization of a recoiled nucleon produced by a longitudinal polarized electron beam can be expressed as [9],

$$I_0 P_x = -2\sqrt{\tau(1+\tau)} G_E G_M \tan(\theta/2) \tag{1.31}$$

$$I_0 P_z = \frac{E_{beam} + E_{e'}}{M} \sqrt{\tau(1+\tau)} G_M^2 \tan^2(\theta/2) \tag{1.32}$$

where P_x is the polarization component perpendicular to the momentum transfer in the scattering plane, P_z is the polarization component along the momentum transfer. τ is defined in eq (1.13). M is the mass of the nucleon, θ is the scattering angle of the electron, E_{beam} is the initial energy of the beam, and $E_{e'}$ is the energy of the scattered electron.. $I_0 = \left(A(Q^2) + B(Q^2)\tan^2\frac{\theta}{2}\right)$ as in eq (1.28).

In the one-photon-exchange approximation $P_x = P_z = 0$ unless the beam is polarized. Hence, the ratio of G_E/G_M can be obtained by

$$\frac{G_E}{G_M} = -\frac{P_x}{P_z} \frac{E_{beam} + E_{e'}}{2M} \tan(\theta/2) \tag{1.33}$$

Since G_M is more precisely obtained by other measurements, G_E^n can be extracted from this ratio.

The first measurement by this means was done by Eden *et al.* [10] for $d(\vec{e}, e\vec{n})p$ at $Q^2 = 0.255$ (GeV/c)^2. The result was $G_E^n = 0.066 \pm 0.036 \pm 0.009$, where the

uncertainties are separated into statistical and systematic. While the statistical uncertainties dominated in this measurement, this measurement showed the feasibility of high-precision measurements at the MIT-Bates laboratory or at JLab by improving the statistics.

1.3.3   Semi-inclusive $^3\vec{H}e(\vec{e}, e'n)$

This method is represented by eq. (1.22) or eq. (1.27). The asymmetry in the cross sections of $^3\vec{H}e(\vec{e}, e'n)$ with opposite beam helicity states is bigger than that of $^3\vec{H}e(\vec{e}, e')$, due to the fact that the neutron is tagged and the two protons have the opposite spin in the S wave component of the ^{3}He nucleus. Thus, the relative error is decreased. This semi-inclusive method avoids the complication of the proton contribution in the ^{3}He response functions, whereas it needs additional work on the neutron detector.

The extraction of G_E^n by the semi-inclusive method is based on the Plane-Wave Impulse Approximation (PWIA), which will be elaborated on in the last chapter. PWIA treats reacting nucleons as "quasi-free" in interaction with spectator nucleons. Research has shown evidence [11] that spin-dependent final-state interactions (FSI) and Meson Exchange Currents (MEC) become diminishing small for $Q^2 > 0.3$ (GeV/c)^2.

The first measurement of semi-inclusive $^3\vec{H}e(\vec{e}, e'n)$ was made at Mainz by Meyerhoff *et al.* [12]. At $Q^2 = 0.31$ (GeV/c)^2, they found $G_E^n = 0.035 \pm 0.012 \pm 0.005$. Later improved experiments were performed at higher Q^2 and uncertaintiess were reduced.

The most advanced semi-inclusive measurement of G_E^n at JLab was done in experiment E02013 in which Riordan *et al.* [13] measured G_E^n at $1.72(GeV/c)^2 < Q^2 < 3.41$ $(\text{GeV/c})^2$ and got the results shown in table 1.1.

Table 1.1: Measurements $^3\vec{H}e(\vec{e}, e'n)$ by Riordan *et al.* at JLab. The form factor ratio $g_n = \mu_n G_E^n / G_M^n$

Q^2 (GeV/c)^2	$g_n \pm stat \pm syst$	$G_E^n \pm stat \pm syst$
1.72	$0.273 \pm 0.020 \pm 0.030$	$0.0236 \pm 0.0017 \pm 0.0026$
2.48	$0.412 \pm 0.048 \pm 0.036$	$0.0208 \pm 0.0024 \pm 0.0019$
3.41	$0.496 \pm 0.067 \pm 0.046$	$0.0147 \pm 0.0020 \pm 0.0014$

1.3.4   Inclusive $^3\vec{H}e(\vec{e}, e')$

The measurement of G_E^n by inclusive $^3\vec{H}e(\vec{e}, e')$ has so far been the most difficult one due to the lack of theoretical calculations and its narrow useful kinematic range. A ^{3}He nucleus contains 2 protons and a neutron. The Nucleon-Nucleon potential theory predicts that the ground-state ^{3}He wave-function is dominated by the spatically symmetric S-state ($\approx$88%) with small admixtures of D-state ($\approx$12%), mixed-symmetry S'-state ($\approx$1.5%), and more complicated configurations (fig. 1.4). The spins of the 2 protons cancel each other in the S-state, leaving the neutron spin to stand out and ^{3}He to be an effective neutron target. Theoretical work with different models and approximations has been performed to calculate the proton contribution to the polarization of the ^{3}He nucleus. Averaging over available calculations [14] gives nucleon

polarizations in $^3\vec{H}e$ of $P_n = 0.86 \pm 0.02$ for neutrons and $P_p = -0.028 \pm 0.004$ for protons, with the remainder of the spin residing in the orbital motion.

Blankleider and Woloshyn [15] calculated the spin-dependent momentum distribution of the nucleons in a ^{3}He nucleus using the closure approximation and a Faddeev wave-function based upon a separable expansion of the Reid soft-core potential. Based on this calculation the first inclusive $^3\vec{H}e(\vec{e}, e')$ measurement was done at the MIT-Bates laboratory by C.E. Jones-Woodward *et al.* in the 80's, with asymmetries shown in fig. 1.5. A subsequent measurement by Thompson *et al.* [16] was also performed at the MIT-Bates laboratory. Table 1.2 summarizes results of inclusive $^3\vec{H}e(\vec{e}, e')$ measurements.
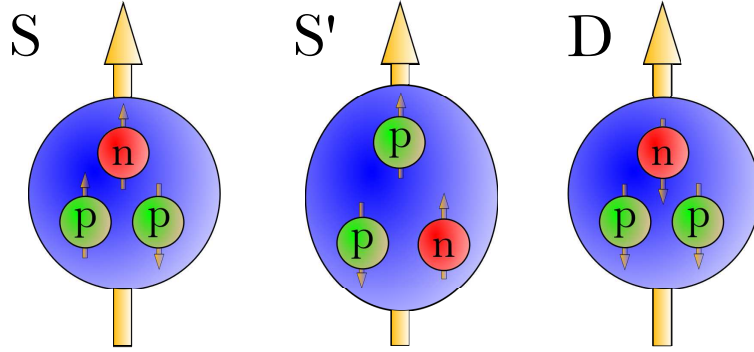
Figure 1.4: Spin structure of ground-state ^{3}He nuclei. The Nucleon-Nucleon potential theory predicts that the ground-state ^{3}He wave-function is dominated by the spatically symmetric S-state ($\approx$88%) with small admixtures of D-state ($\approx$12%), mixed-symmetry S'-state ($\approx$1.5%), and more complicated configurations. Averaging over available world calculations [14] gives the nucleon polarizations in $^3\vec{H}e$ to be $P_n = 0.86 \pm 0.02$ for neutrons and $P_p = -0.028 \pm 0.004$ for protons, with the remainder of the spin residing in orbital motions. Note that the elliptical shape of the S'-state is just a demonstration of the coupling between spin and orbital wave functions
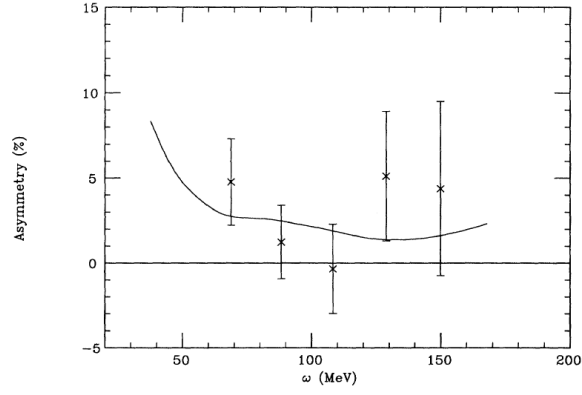
Figure 1.5: Experimental A(ω) by Jones-Woodward *et al.* [2] and Faddeev calculation. The solid line is the best fit. Error bars contain only statistics.

Table 1.2: Previous measurements of $^3\vec{H}e(\vec{e}, e')$ aiming at measuring G_E^n. The errors are expressed in the order of statistical and sysmatic.

θ_e (deg)	Q^2 $(\mathrm{GeV/c})^2$	ω (MeV)	Transverse-longitudinal asymmetry $A_{TL'}$ (%)	G_E^n	Reference
102	0.16	58-161	+2.4±1.3±0.4	+0.070±0.100 ±0.035	[2]
90	0.20	70-160	+1.75±1.2±0.31	+0.044±0.074	[16]

Considerably larger uncertainties are associated with these measurements due to 2 reasons:

1)the overwhelming proton contribution in transverse-longitudinal asymmetry $A_{TL'}$ due to the comparatively small neutron electric form factor G_E^n at low Q^2, and

2)insufficient theoretical support in the extraction.

Theoretical advances and increased Q^2 values made the extraction of G_E^n presented in this dissertation feasible. The theoretical work was conducted by Salme' *et al.* [4]. The relatively high Q^2=0.95 $(\mathrm{GeV/c})^2$ makes the contribution from the neutron in the ^{3}He response functions much more pronounced, thus reducing the effect from the contribution of the protons.

1.3.5 World Data

With various methods applied, a selected world data of G_E^n is shown in fig. 1.6. The parameterizations of proton and neutron form factors done by J.J. Kelly is shown in fig. 1.7 [3]. Details of this parameterization will be introduced in the last chapter.
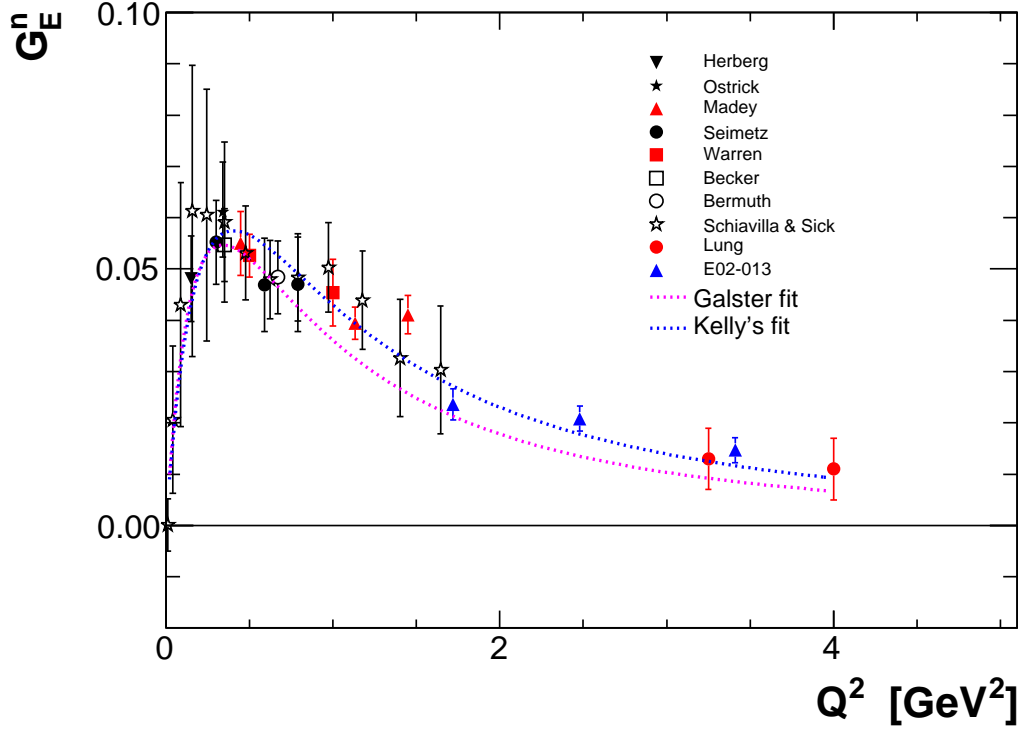
Figure 1.6: Selected world data of G_E^n vs Q^2.
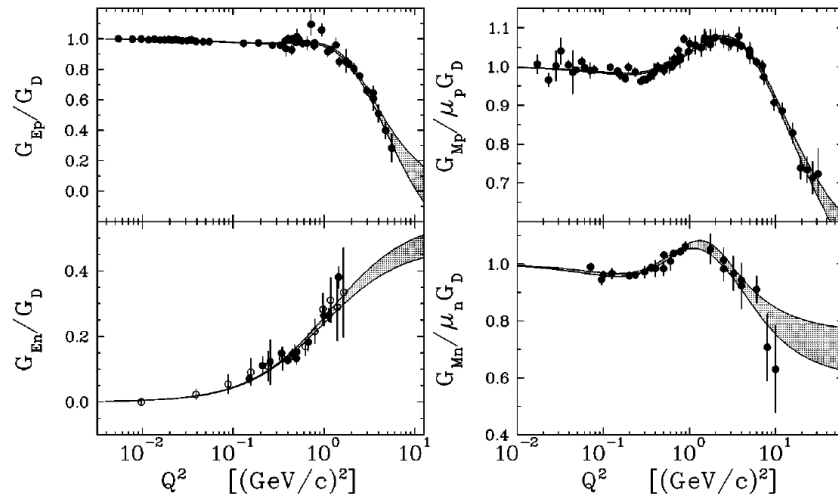
Figure 1.7: Selected world data of all four form factors divided by the dipole form factor G_D at different Q^2, together with J.J. Kelly's parameterization[3]

Chapter 2

Experimental setup

2.1 Jefferson Lab and Hall A

The Experiment E05102 was undertaken during May and June of 2009 in Jefferson
Lab. Jefferson Lab (JLab), or Thomas Jefferson National Accelerator Facility (TJ-
NAF), formally known as Continuous Electron Beam Accelerator Facility (CEBAF),
is a medium energy electron accelerator laboratory located in Newport News, Vir-
ginia. The lab is funded by the Department of Energy (DOE). The accelerator is
capable of delivering high quality electron beam up to 6 GeV and is being upgraded
to 12 GeV delivery. The electron beam is accelerated in the super-conducting linear
accelerators (LINAC's) and dissipated into 3 experimental halls. An aerial view of
JLab is shown in fig. 2.1.

E05102 was conducted in Hall A. The central detector elements of Hall A are

two High Resolution Spectrometers (HRS) designed for high resolution detection of electrons or protons both spatially and kinematically. The schematic cross section of Hall A with one of the HRS's in the (fictitious) 0° position is shown in fig. 2.2.

Figure 2.1: Aerial view of JLab
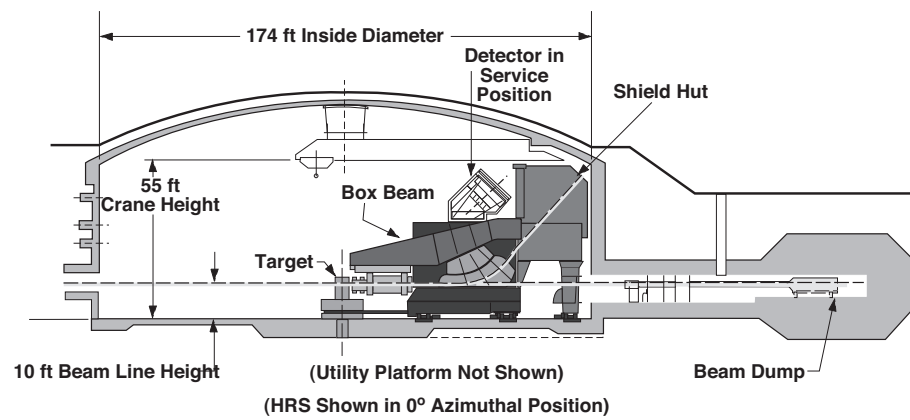
Figure 2.2: Schematic cross section of Hall A with one of the HRS's in the (fictitious) 0° position.

2.2 Quasi-Elastic Family of Experiments and Their Kinematics

The quasi-elastic family of experiments consisted of 3 independent experiments which shared the beam, target, and detectors. The overall layout of the quasi-elastic family experiments is shown in fig. 2.3. The 3 experiments are:
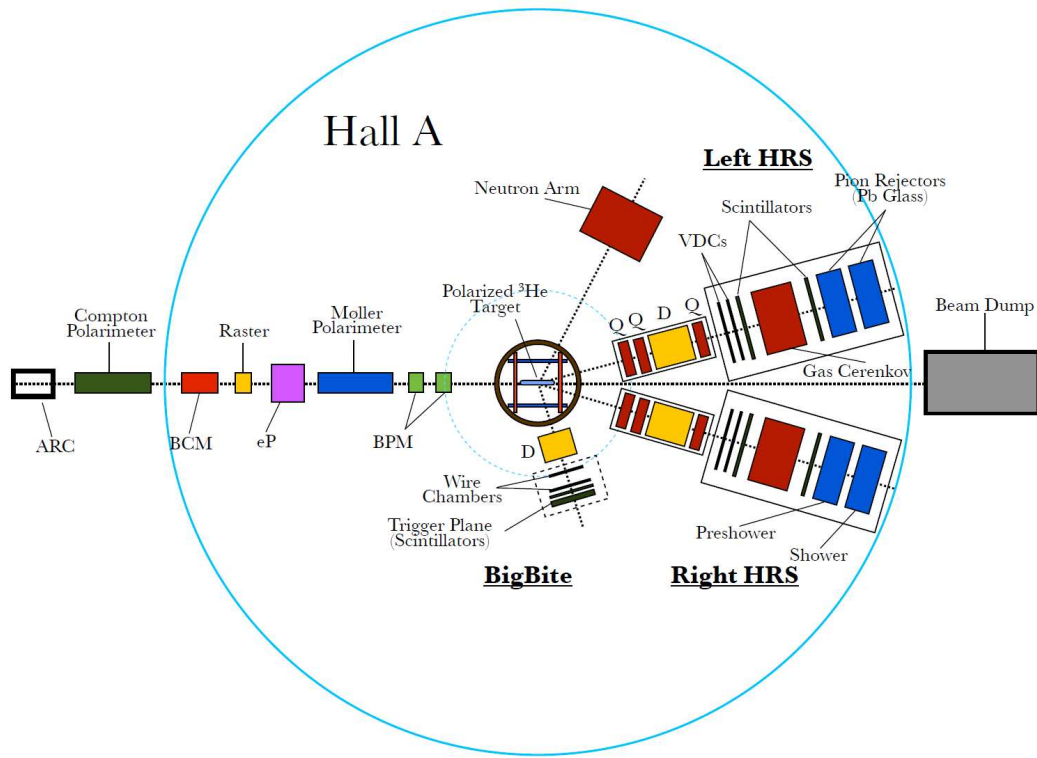
Figure 2.3: Layout of all detectors used in the quasi-elastic experiments. The detectors include: a pair of HRS's, a BigBite spectrometer used for proton and deuteron detection in E05102, and a neutron detector used for neutron detection in E08005.

1)E05015, or Ay for short: a measurement of the Target Single-Spin Asymmetry

in Quasi-Elastic $^3\vec{H}e(e, e')$. This experiment focuses at studying asymmetries caused by the Two-Photon Exchange effects. The direction of the target polarization was vertical, or perpendicular to the scattering plane in this measurement. This polarization configuration should supposedly produce a zero asymmetry in the yields of the two HRS's by the mechanism of One-Photon Exchange.

2)E05102, or e'd for short: a measurement of the A_x and A_z Asymmetries in the quasi-elastic $^3\vec{H}e(\vec{e}, e'd)$. Here the A_x and A_z refer to the decomposed asymmetries when the target polarization is parallel or perpendicular to the three-momentum transfer vector, or $\overrightarrow{q}$. This experiment measures $^3\vec{H}e(\vec{e}, e'd)p$ or $^3\vec{H}e(\vec{e}, e'p)$ channels aiming at studying the ^{3}He structure itself instead of using it as an effective neutron target. The asymmetries in the yields at different beam helicity states would indicate the weight of different components (S, S' and D waves) in the ^{3}He ground-state wave-function.

3)E08005, or e'n for short: a measurement of the Beam Helicity Spin Asymmetry in the Quasi-Elastic $^3\vec{H}e(\vec{e}, e'n)$ Reaction. This experiment measures the asymmetries in the coincident scattered electron-neutron events in order to study the neutron electric form factor by tagging neutrons, and to test the validity of the Plane-Wave Impluse Approximation in the extraction of neutron form factors.

E05015 ran independently between Apr 24th, 2009 and May 12th, 2009. It only used a pair of HRS's for detecting electrons. Its kinematics settings are in table 2.1

E05102 and E08005 ran simultaneously proceeding E05015. They shared the same

Table 2.1: E05015, or Ay experiment kinematics

Beam energy (GeV)	HRS-L angle(°)	HRS-R angle(°)
1.245 (1st pass)	17	17
2.425 (2nd pass)	17	17
3.606 (3rd pass)	17	17

target and beam, while E05102 used the HRS-L for electron detection and the BigBite for coincident proton and deuteron detection, and E08005 used the HRS-R for electron detection and the neutron detector for coincident neutrons. Kinematics of E05102 and E08005 are in table 2.2 and table 2.3 respectively.

Table 2.2: E08005 e'n experiment kinematics

Beam energy (GeV)	HRS-L angle(°)	BigBite angle(°)
2.425 (2nd pass)	14.5	75
2.425 (2nd pass)	14.5	82
2.425 (2nd pass)	12.5	82

Table 2.3: E05102 e'd experiment kinematics

Beam energy (GeV)	HRS-R angle(°)	Neutron detector angle(°)
2.425 (2nd pass)	16	54
2.425 (2nd pass)	18	54

However, the kinematics of interest in this thesis are different from the proposed settings above. The measurement was done during the last 2 days of the experiment for testing purposes with kinematics in table 2.4. It only used the HRS-R and its floor plan is shown in fig. 2.4.

Table 2.4: Kinematics of this thesis for measurement of G_E^n

Beam energy (GeV)	HRS-R angle($°$)
3.606 (3rd pass)	17
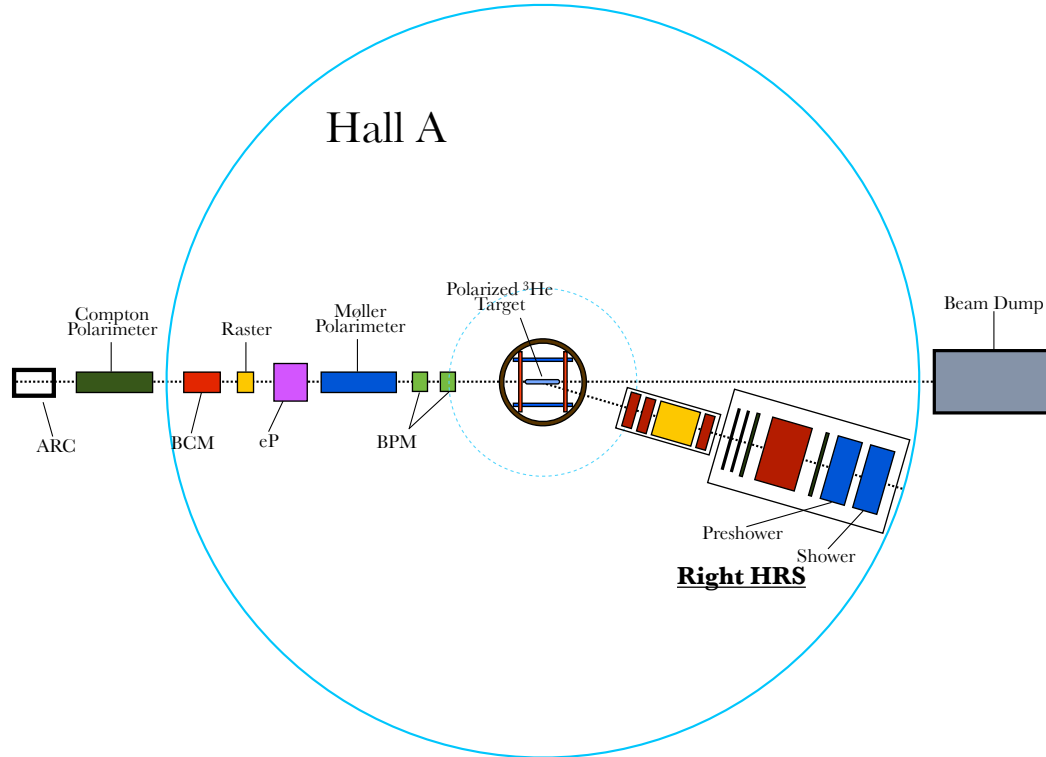
Figure 2.4: Detectors and beamline only used in the measurement of G_E^n .

2.3 Polarized Electron Source

The electrons in CEBAF are injected into the accelerator from either a thermionic or a polarized gun. The polarized source evolved from its ancestor in the Stanford Linear Accelerator Center (SLAC) [17]. The cathode is created by growing layers of various GaAs combinations, as shown in fig. 2.5. The strained GaAs cathode is illuminated by a 1497 MHz gain-switched diode laser operated at 780 nm. The strain creates a gap in the different sub-levels of the $P_{2/3}$ electrons in the valance bands of GaAs. By turning the left-handed circularly polarized laser to the proper frequency, electrons from the $P_{3/2}$ m=3/2 state can be excited to the $S_{1/2}$ m=1/2 level of the conduction band. From there the electrons diffuse to the surface and escape into the surrounding vacuum.
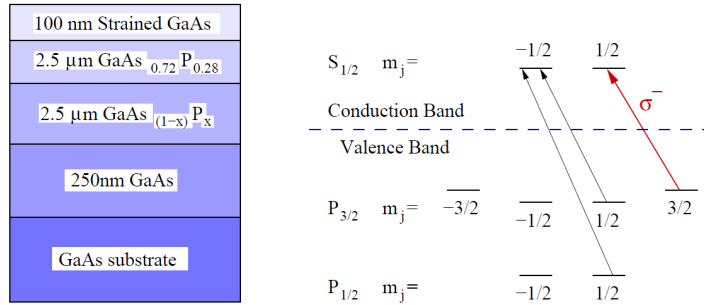
Figure 2.5: Structure of the strained GaAs cathode and the energy levels.

Since the polarized electrons are produced by shining the circularly polarized laser on a GaAs photocathode, the helicity of the electrons produced is determined by the spin direction of the photons. A Pockel's cell gives out a phase retardation by the

voltage applied on it. In the experiment the high voltage in a Pockel's cell changed at a frequency of 30 Hz and the beam helicity changed at this frequency by the phase change of the spin direction of the photons (or the circular polarization direction of the laser beam) illuminating the photo cathode.

2.4   Accelerator
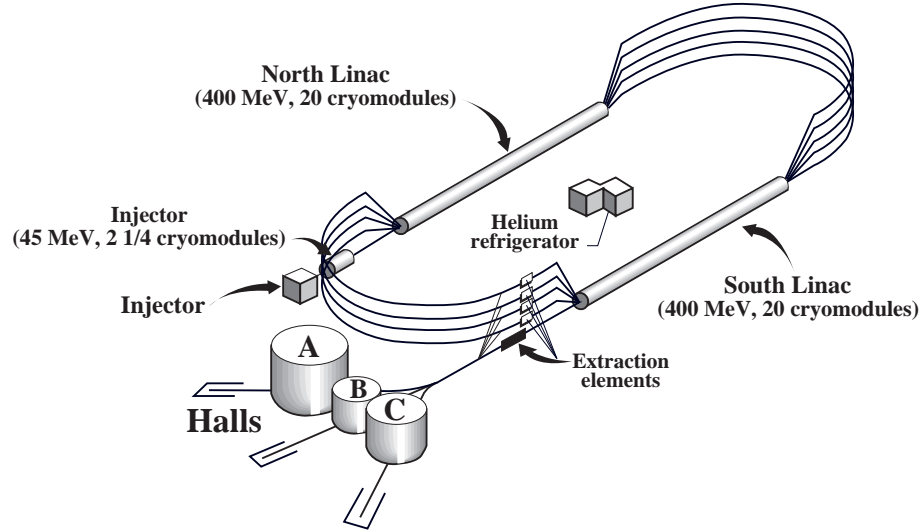
Figure 2.6: Demonstration of JLab accelerator

The layout of the accelerator in JLab is in fig. 2.6. JLab operates a radio frequency (RF) electron accelerator that recirculates the beam up to five times through two super-conducting linear accelerators (Linac): the North Linac and the South Linac. Each Linac accelerates the beam by 0.4 GeV. The electron beam is delivered from the electron injector into the Linac, and after passing the Linacs and the recirculation arcs, it can be extracted and delivered into any of the three experimental halls, or be

kept running in the accelerator for additional acceleration. In each pass the energy of the beam is increased by 0.8-1.2 GeV. A maximum of 5 circulations in the Linacs, or an energy of around 6 GeV can be achieved in the current setting. The electrons in the beam keep their spin uniformly parallel or anti-parallel to their momentum.

There is a Half-Wave Plate (HWP) installed before the beam is split into the 3 halls. The HWP can change the beam phase by π, or flips its helicity. The measured beam-helicity asymmetry (asymmetric cross sections at different beam helicity states) should flip sign and keep the same magnitude when there is a half-wave phase shift in the electron beam. Some systematic errors can be erased to the first order in this way by using the average of the magnitudes of the two asymmetry measurements when the half-wave plate is in and out.

2.5   Beamline

As shown in fig. 2.7, Hall A beamline starts at the Arc section (for beam energy measurement, in the next subsection) and proceeds into Compton beam polarimeter, two beam current monitors (BCM) between which is located an Unser monitor (for absolute beam current measurement), a fast raster, the eP device for beam energy measurement, a Møller beam polarimeter, and a number of beam position monitors (BPM). The beam then hits the polarized ^{3}He target at the center of the hall before being stopped at the beam dump.
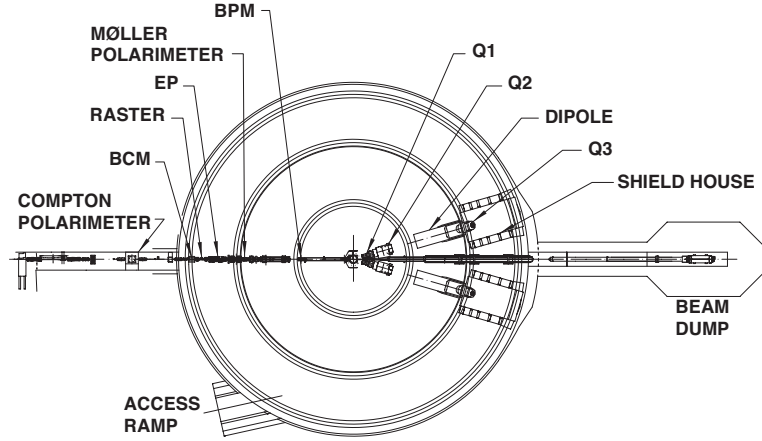
Figure 2.7: Schematic layout of Hall A, indicating the location of the Compton and the Møller Polarimeters, the raster, the EP energy measurement device, the beam current and position monitors (BCM and BPM's), and the beam dump. Also shown are the High Resolution Spectrometer components (Q1, Q2, dipole, Q3 and the shield house). Note that the EP energy measurement device and the Compton Polarimeter were not used in this experiment.

2.5.1 Beam Energy Measurement

The beam energy was measured by the Arc method (fig. 2.8) [18] in this experiment. The Arc method is based on the principle that the electron trajectories are bent in a magnetic field, and its curvature of bending is affected by the momentum of the electron and the strength of the magnetic field. Specifically eight dipoles are used to generate the magnetic field in Hall A. When the beam travels in the dipole field, the beam momentum (p in GeV/c) is related to the field integral of the eight dipoles ($\int \vec{B} \cdot \vec{dl}$ in Tm) and the net bending angle through the Arc section (θ in radians) by [19]

$$pc = k\frac{\int \vec{B} \cdot \vec{dl}}{\theta} \tag{2.1}$$

where $k = 0.299792$ GeV rad $\mathrm{T}^{-1}\mathrm{m}^{-1}$, c is the speed of the light. The nominal bending angle in the Arc section is $34.3°$.
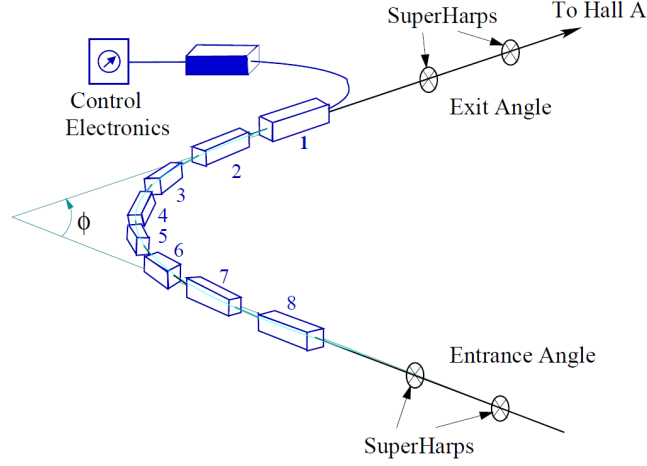
Figure 2.8: Arc section of the beamline.

The Arc method has an uncertainty of less than 0.01% relatively [19] for beam with energy 4.0 GeV (the beam energy is 3.6 GeV in this thesis). During the experiment, the beam energy has been continuously monitored by the Tiefenbach method, which uses the beam position monitors (BPM's) in the Arc to provide the bending angles through the Arc. The relative uncertainty of the Tiefenbach method is in general less than 0.05%.

2.5.2   Beam Position Measurement

Two beam position monitors (BPM's) are employed to determine the position and the direction of the beam. These are each composed of a four-wire strip-line antenna system and are located 7.52 m and 1.29 m upstream from the target. The standard

difference-over-sum technique is then used to determine the relative position of the beam to within 100 μm for currents above 1 μA. [20] Their absolute positions are calibrated by using a set of wire scanners known as the harps.

The BPM's average their positions over 0.3s time periods and record the positions in the EPICS data system at 1 Hz frequency. They also record positions event by event in the CODA data system.

2.5.3   Beam Current Measurement

The complete beam current monitoring system (BCM) is located 25 meters upstream of the target and consists of 2 RF cavities and an Unser Monitor between the cavities. The 2 RF cavities are cylindrical high-Q waveguides tuned to the frequency of the beam. They produce a voltage output proportional to the beam current. The Unser monitor is a Parametric Current Transformer and provides a direct measurement and absolute calibrations of the 2 RF cavities.[21]

The RF cavity outputs are converted into DC voltage levels and then converted into proportional frequency signals. These signals are later fed to 200 MHz VME scalars. The scalar readings accumulate during the run, resulting in a number proportional to the time-integrated voltage level, a direct representation of the total beam charge.

Scalar outputs are calibrated by the calibration runs performed every 2-3 months. After the calibration the charge of a data-taking run can be determined down to a

current of 1 μA with an accuracy of less than 0.5% (Hall A NIM paper [19]).

The beam intensity asymmetry refers to the fact that the intensity of the circulaly polarized laser is different at different helicity states. The extracted physical yields should be normalized by the beam charge at each helicity state, and this correction erases the raw asymmetry dependence on the asymmetry of beam intensity to the first order.

2.5.4　Beam Polarimetry

Two methods are typically used in the measurement of beam polarization in Hall A: the Møller measurement and the Compton measurement. Typically the beam polarization is around 75-90%. The Compton measurement was not used for analysis during this experiment.

Møller Polarimeter

The Møller polarimeter uses a ferromagnetic foil magnetized in a magnetic field of about 24 mT along its plane as a target of polarized electrons. The beam polarization is measured by the beam-helicity asymmetry of the scattering process $\vec{e}^- + \vec{e}^- \rightarrow e^- + e^-$. Theoretically the scattering process has cross section [22]

$$\sigma \propto [1 + \sum_{i=X,Y,Z} (A_{ii} \cdot P_i^{target} \cdot P_i^{beam})], \tag{2.2}$$

where $i = X, Y, Z$ defines the projections of the polarizations. The analyzing power A depends on the scattering angle in the CM frame, θ_{CM}. Assuming that the beam direction is along the Z-axis and that the scattering happens in the ZX plane:

$$A_{ZZ} = -\frac{\sin^2 \theta_{CM} \cdot (7 + \cos^2 \theta_{CM})}{(3 + \cos^2 \theta_{CM})^2}, A_{XX} = -\frac{\sin^4 \theta_{CM}}{(3 + \cos^2 \theta_{CM})^2}, A_{YY} = -A_{XX} \quad (2.3)$$

The Møller measurement provides a statistical accuracy of about 0.2% for about one hour of data taking, and about 3% systematic uncertainty. The measurement is invasive and must be performed separately from an experiment.

Compton Polarimeter

The Compton polarimeter measures the beam polarization by the beam-helicity asymmetry in the Compton scattering, i.e., a circularly polarized photon beam being scattered on the electron beam. Its uncertainty is quoted to be less than 1% statistically with 30 mins running. [23] Due to the improper functioning of the Compton polarimeter in Experiment E05102, the Compton polarimetry was not used in the analysis so far.

2.5.5 Raster

High intensity electron beam tends to overheat and destroy the glass target cell. To prevent this from happening a fast raster was used, which is a set of transverse magnetic field driven at 18 kHz to deviate the beam at a couple of millimeters while

the beam passes through. The deviation is proportional to the current generating the magnetic field, which gives a way to calibrate the raster position by the current fed into the device. The beam rastered was used during reaction with the ^{3}He target cell or the reference cells (glass cell identical to the production target cell, for reference measurements). The rastered beam is not used with carbon foils (no overheating concerns).

2.6 High Resolution Spectrometer (HRS)

2.6.1 Standard Characteristics

Two identical HRS's were used in E05102 experiment to detect scattering electrons up to 4 GeV/c. They are named as Left HRS, or HRS-L meaning the HRS is to the left of the beam when facing the downstream direction of the beam, and Right HRS, or HRS-R which is defined in the similar way. After coming out of the target, the scattered electrons pass a pair of superconducting $\cos(2\theta)$ quadrupoles, a 6.6m long dipole magnet, and a third superconducting $\cos(2\theta)$ quadrupole. The second and third quadrupoles of each spectrometer are identical in their design and construction. The cross section of an HRS is shown in fig. 2.9 and their standard characteristics are in table 2.5 [19]. The parameters in this table describe the performance of the HRS's in the ideal case. In a real experiment the performance of the HRS's are not as good as this ideal case.

The trajectory of a particle in the HRS is bent and shifted by the magnetic field inside the HRS, and the original trajectory of the particle needs to be reconstructed from its final trajectory in the Verticle Drift Chambers (VDC's) located downstream of an HRS. This process is called the optics reconstruction and will be elaborated in the next chapter.

Table 2.5: Main design characteristics of the Hall A High Resolution Spectrometers. The resolution values are for the FWHM (Full-Width at Half-Max).

Configuration	QQD_nQ Vertical bend
Bending angle	45°
Optical length	23.4 m
Momentum range	0.3 - 4.0 GeV/c
Momentum acceptance	$-4.5\% < \delta p/p < +4.5\%$
Momentum resolution	1×10^{-4}
Dispersion at the focus (D)	12.4 m
Radial linear magnification (M)	-2.5
D/M	5.0
Angular range HRS-L	12.5° - 150°
HRS-R	12.5° - 130°
Angular acceptance: Horizontal	±30 mrad
Vertical	±60 mrad
Angular resolution : Horizontal	0.5 mrad
Vertical	1.0 mrad
Solid angle at $\delta p/p = 0$, $y_0 = 0$	6 msr
Transverse length acceptance	±5 cm
Transverse position resolution	1 mm

The detector package after the HRS-R is described below, as shown in fig. 2.10.

The detector package of the HRS-R includes:
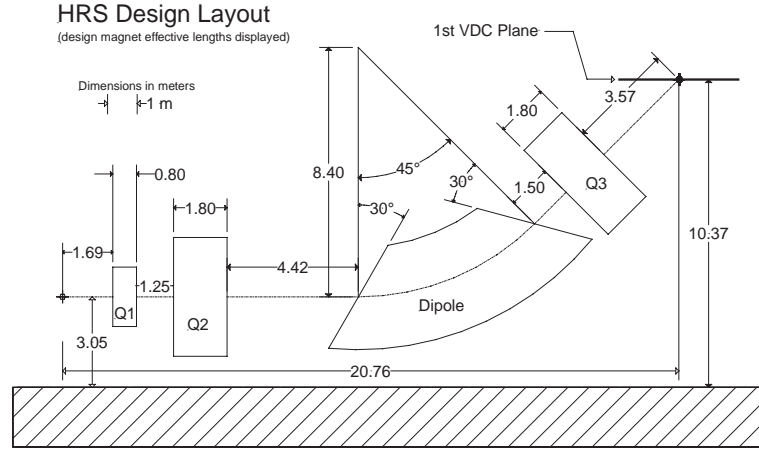
Figure 2.9: HRS layout, including the quadrupoles and dipoles, and the first VDC tracking detector.

1)a pair of Vertical Drift Chambers (VDC's) to determine the trajectory of a particle;

2)two scintillator planes (S1 and S2) to generate the trigger and the time-of-flight information;

3)a Gas Cherenkov detector for e^-/π^- separation;

4)a Preshower and a Shower for additional e^-/π^- separation.

The main configurations the detector package in the HRS-L always include two VDC's and the scintillator planes. In E05102 the Pion Rejectors (Pb Glass) and the Gas Cerenkov detector were included in the detector package of the HRS-L.

2.6.2   Vertical Drift Chambers (VDCs)

Each VDC chamber is composed of two wire planes, separated by about 335 mm. The active area of the chamber is 2118 mm × 288 mm. The wires in each plane
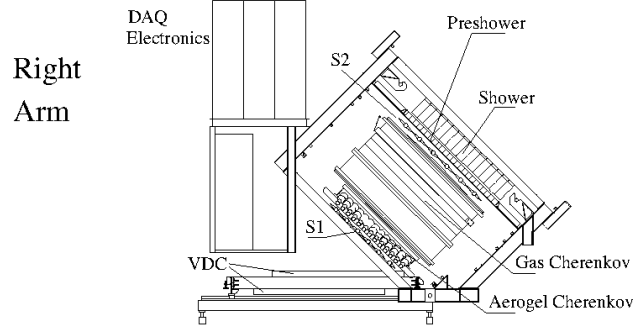
Figure 2.10: A sideview of a standard HRS-R detector stack. The aerogel Cerenkov detector was not used in this measurement.

are oriented vertically to one another, and the planes lie in the laboratory horizontal plane. The nominal particle trajectory is at 45° with respect to the wire plane, as shown in fig. 2.11. Gas filled in VDC's is a mixture of argon (62%) and ethane (38%).

When a high voltage ($\sim$4.0 kV) is applied to the wires in the wire plane, an electric field is generated inside the chambers. Particles passing through the chambers ionize the medium gas through an avalanche process. The ionized electrons are finally collected at the wires and a signal is therefore shaped at LeCroy amplifier-discriminator cards 2735DC, and then routed and fed into a Fastbus LeCroy Time-Digital Converter (TDC) module. The TDC measures the arrival time of the clustered ionized electrons on the wires. The difference of this arrival time and the time of the event (measured by the scintillator planes S1 and S2) is actually the drift time of the ionized electrons, and it gives out an indication of the position of the particle hitting the drift chambers. When two sets of positions from the two chambers are obtained, the velocity and the
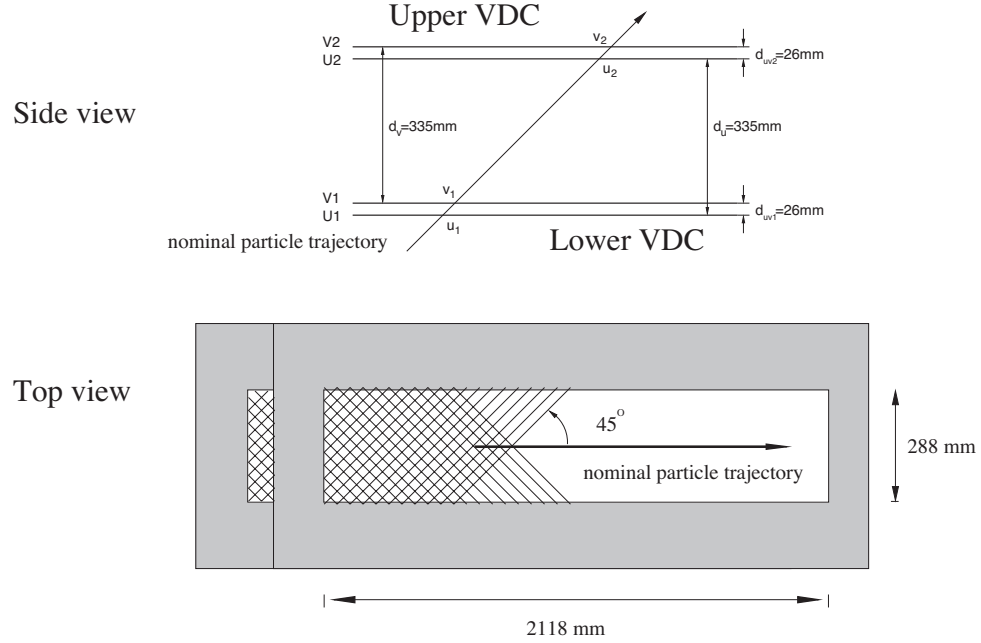
Figure 2.11: Layout of VDC and its nominal particle trajectory.

direction of the track can be calculated. The nominal spatial resolution of the VDC's

is ∼200 μm.

2.6.3 Scintillator

Scintillators are made of plastic (5 mm BC408) and provide triggers in the HRS

system. When a charged particle passes through a scintillator, it deposits energy in

the scintillator. The energy is turned into the light signals. Two scintillator planes

(S1 and S2) are located 1.5 m and 3.5 m downstream of the center of the focal

plane and are perpendicular to the nominal incident ray. Each plane is composed of

6 overlapping scintillator paddles with a photo-multiplier (Burle 8575) attached to either side of the paddle. The time resolution of the photo-multiplier is approximately σ=30 ns. If a photo-multiplier fires (a particle comes in to generate a recordable signal), it triggers the data acquisition system (DAQ) and let the signal from TDC be recorded.

2.6.4 Gas Cherenkov Detector

Cherenkov radiation happens when a high energy charged particle travels faster than the speed of light c/n in the medium. The emitted Cherenkov light forms a light cone with an apex angle $\theta_c = \cos^{-1}(1/(\beta n))$. The Hall A Gas Cherenkov detector is mounted between the scintillator planes S1 and S2. It is filled with CO_2 with index of refraction n=1.00041, which gives a threshold of $p_{min} = 17$ MeV/c for electrons and $p_{min} = 4.8$ GeV/c for pions (and more for heavier particles). The electron identification efficiency is at 99% at this threshold [19]. The Cherenkov light is reflected by 10 spherical mirrors , each focused at a photo-multiplier tube (PMT) located at the side of the detector box.

The Aerogel Detector (index of refraction 1.015) is sometimes used in combination with the Gas Cerenkov detector, but not in this measurement.

2.6.5   Shower Detector

The shower detector (fig. 2.12) on each HRS provides an additional e^-/π^- separation. It consists of 2 layers, called the preshower and the shower. The blocks in both layers in the HRS-L and in the first layer in the HRS-R are perpendicular to the particle tracks. The blocks in the second layer of the HRS-R are parallel to the tracks. In HRS-R, the first layer is composed of 48 blocks of TF1 lead glass and the second layer is composed of 80 blocks. Both layers of the HRS-L are composed of 34 lead glass blocks. PMTs are attached to both ends of the glass blocks to collect light.

High energy particles such as electrons or photons can create cascade when interacting with lead glass, thus deposit energy which is converted into light and heat eventually. Most of pions in the experiment only pass straight through the lead glass and deposit much less energy than electrons. (Due to their greater mass, pions are not as sharply accelerated as electrons when they encounter electromagnetic fields, and do not emit as much bremsstrahlung radiation. Thus pions of a given energy penetrate the medium far more deeply than electrons, since the energy loss of electrons and pions is primarily due to the decelaration by this mechanism.) Plotting the energy deposition of the preshower and the shower provides an effective way to identify electrons and pions. In the experiment this separation can be shown in fig. 4.1.

HRS-L
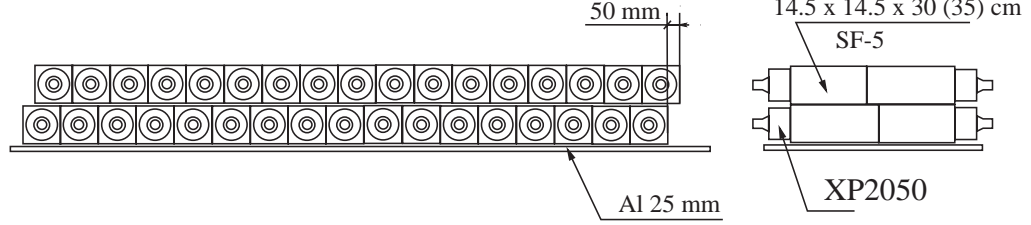
HRS-R
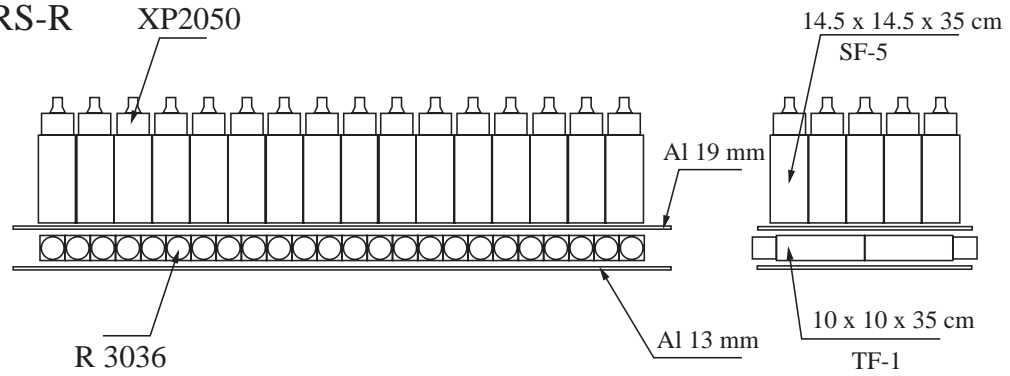
Figure 2.12: Schematic layout of part of the shower detectors in HRS-L (top) and HRS-R (bottom). Particles enter from the bottom of the figure.

2.7 Trigger System

The triggers in E05102 (with HRS-L and BigBite) were:

- T1: triggers each time when E plane (the BigBite scintillator plane with 3 cm thickness) is hit;

- T2: triggers each time when dE plane (the BigBite scintillator plane with 3 mm thickness) is hit; complementary to T1;

- T3: main HRS-L single trigger, triggers when HRS scintillator planes S1 OR S2 is hit;

- T4: supplementary HRS-L single trigger, triggers when Cerenkov AND (S1 OR

S2) are hit;

- T5: coincidence of T1 AND T3;

- T6: coincidence of T2 AND T3;

- T8: 1024 Hz pulser.

The triggers in E08005 (with HRS-R and the neutron detector) were:

- T1: main HRS-R single trigger, triggers when HRS scintillator planes S1 OR S2

is hit;

- T2: supplementary HRS-R single trigger, triggers when Cerenkov AND (S1 OR

S2) are hit;

- T8: 1024 Hz pulser.

When the event rate (number of events per second) is high, the DAQ system can not record all the events. Cummulative events pile up in the time windows of the DAQ, causing each signal to be indistinguishable. To prevent this from happening, selected number of events are recored by the DAQ. The events are thus selected, or prescaled by a prescale factor p_{type} at the trigger supervisor, which means that on average one event is recorded every p_{type} events.

The DAQ livetime is defined as

$$LT = \frac{\text{number of events recorded by DAQ}}{\text{number of events fed to DAQ}} \tag{2.4}$$

The livetime gives an indication of the percentage of the events recorded, and it is used to correct the yield of each helicity state, as shown in eq. (4.4) of Chapter 4.

2.8   Polarized ^{3}He Target

Polarized ^{3}He target was used in E05102 as an effective neutron source. The spin
directions of the 2 protons in the S state of the ^{3}He wave-function are anti-parallel
and cancel each other, leaving most of the polarization of the ^{3}He nucleus carried by
the neutron. The polarization technique is Rb-K (rubidium-potassium) hybrid optical
pumping. An average polarization of 55% was achieved during the experiment.

2.8.1   Optical Pumping and Spin Exchange

The energy levels of an atom in a magnetic field can be denoted by $N^{2S+1}L_J$, where N
is the electron shell, S the electron spin, L is the oribital angular momentum, and J is
the total angular momentum, J=L+S. Right-handed circular polarized light induces
transitions in Rb atoms from $5^2S_{1/2}$ (m=-1/2) ground state to $5^2P_{1/2}$ (m=1/2). The
excited electrons decay to m=-1/2 and m=1/2 states with equal probability, but only
states with m=-1/2 are stimulated again, which makes m=1/2 states overwhelming.
The N_2 gas is mixed with Rb vapor in order to absorb the photons emitted from the
decay process and therefore increase the pumping efficiency. The process above is
called the optical pumping, as illustrated in fig. 2.13

Another alkali metal element, K, is used to collide with Rb and transfer polar-
ization in order to decrease the time needed for polarization (or "spin-up time"). In
this scnerio Rb and K atoms undergo spin-exchange collisions with each other and
the ^{3}He atoms, thus help ^{3}He atoms be polarized faster (fig. 2.14). The spin-up time

without K is around 15 hours, whereas the spin-up time with K is 3-5 hours less.
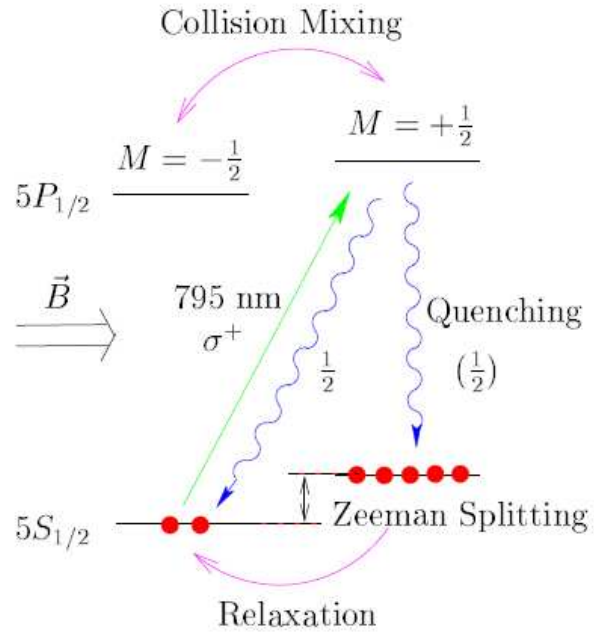
Figure 2.13: Optical pumping of Rb by circularly polarized light.
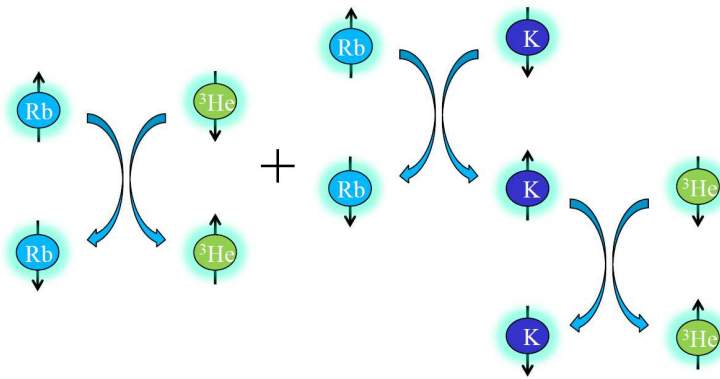
Figure 2.14: Spin exchange scheme of Rb, K, and ^{3}He atoms.

2.8.2 Taget Setup

The target cell (fig. 2.15) is made of alunimosilicate glass and is filled with ^{3}He gas at 10 atm at room temperature. The target cell in E05102 experiment is 40 cm long and 1.9 cm in diameter. The end windows are approximately 120 μm thick and the side wall is approximately 1 mm thick. The pumping chamber (where Rb, K and ^{3}He atoms are polarized and exchange polarization) is above the target cell, and is connected with the target cell by a thin pipe. Polarized Rb and K atoms condense on the wall of the thin pipe, leaving few atom escaping into the target cell.

Figure 2.16 shows the schematic layout of the ^{3}He target system. There are 2 pairs of Helmholtz coils to provide the main magnetic holding field in the pumping chamber. The pumping chamber is mounted inside an oven heated at 170°C to vaporize the Rb. A set of 3 laser beams is used for polarization in 3 directions. The Nuclear Magnetic Resonance (NMR) system consists of one pair of pick-up coils on either side of the target cell and a pair of RF coils at the top and the bottom of the scattering chamber. The electron paramagnetic resonance (EPR) system shares the RF coils with the NMR system and uses a photodiode and related optics to collect the EPR light signal.

2.8.3 Taget Polarimetry: NMR and EPR

Two methods are used in the ^{3}He target system for polarimetry: the Nuclear Magnetic Resonance (NMR) and the Electron Paramagnetic Resonance (EPR).
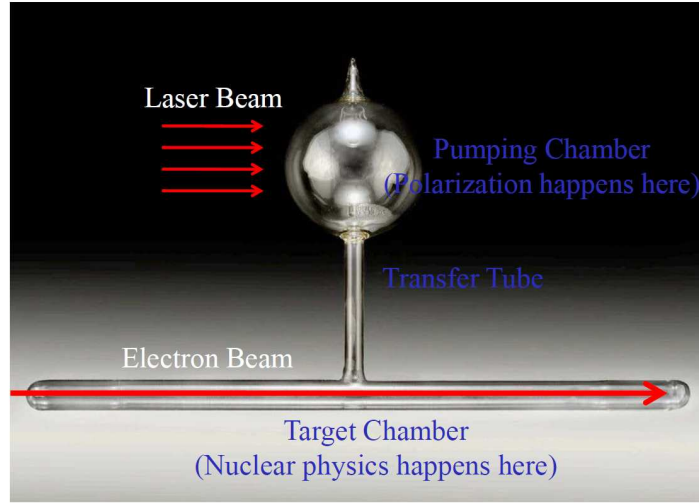
Figure 2.15: Target cell and pumping chamber.

NMR

In an NMR measurement a set of nuclei is placed into a radio frequency magnetic field. When certain conditions are met, resonance happens and there is a measurable signal proportional to the target polarization.

In the classic model, a nuclei is polarized and is put in a holding field $\vec{H}_0$ with the same direction as the direction of the nuclei spin. A perpendicular rotating field $\vec{H}_1$ is then applied with frequency ω_0. The nuclei process is described by eq. (2.5):

$$\frac{d\vec{M}}{dt} = \gamma \vec{M} \times (\vec{H}_0 + \vec{H}_1) = \gamma \vec{M} \times \vec{H}_e \tag{2.5}$$

where $\vec{M}$ and γ are the magnetic moment and gyromagnetic ratio of the nuclei, respectively, and $\vec{H}_e$ is the total magnetic field.

In the frame rotating with $\vec{H}_1$ at angular frequency $\omega_0 \hat{k}$, and if $\vec{H}_0$ is set along the
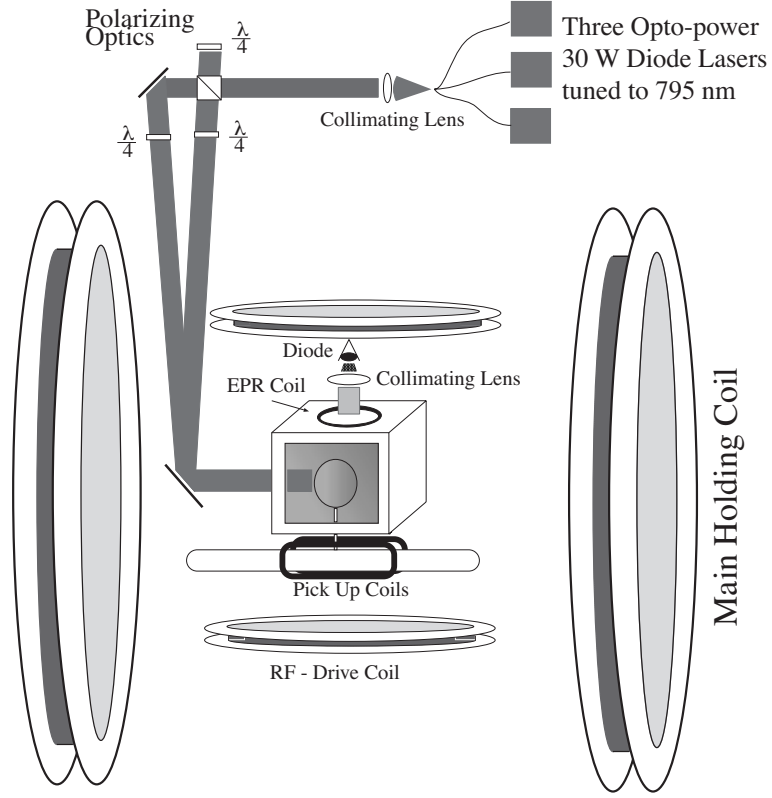
Figure 2.16: Schematic layout of the ^{3}He target system. Only one set of Helmholtz coils is shown.

z axis, the effective magnetic field

$$\vec{H}_e = (\vec{H}_0 - \frac{\omega_0}{\gamma})\hat{k} + \vec{H}_1\hat{i'} \tag{2.6}$$

Initially the holding field $\vec{H}_0$ is smaller than $\frac{\omega_0}{\gamma}$, and the effective field $\vec{H}_e$ is almost parallel to $-\hat{k}$. $\vec{H}_0$ is then swept through resonance till $H_0 > \frac{\omega_0}{\gamma}$. At resonance $(H_0 = \frac{\omega_0}{\gamma})$ the effective field $\vec{H}_e = \vec{H}_1\hat{i'}$. The whole process is in an adiabatic fast passage (AFP), i.e., the sweep can not be too fast to fail the adiabatic process, nor can it be too slow to be affected by the spin relaxation.

In the experiment the holding field is scanned back and forth from 25 G to 32 G. 28.06 G is the resonance condition. When resonance happens, the magnetic flux in the pick-up coils gets to its maximum value, which is proportional to the magnitude of the ^{3}He polarization. And the NMR readouts are calibrated by AFP signals from an identical water sample.

EPR

The Electron Paramagnetic Resonance polarimetry (EPR) measures the shift in the electron energy levels when a nuclei is placed in a magnetic field, the so-called Zeeman effect. In E05102 the shift in K nuclei was studied. In the polarized ^{3}He cell the Zeeman effect has two shifts: the shift due to the spin exchange mechanism and the shift due to the classical magnetic field of the polarized ^{3}He. Again an adiabatic fast passage process (AFP) is used to isolate the shift from the magnetic field of the polarized ^{3}He, in which the direction of the spin of ^{3}He is changed by changing the frequency of the applied field while keeping the magnitude of the holding field constant.

After the isolation the energy shift (represented by shift in the resonance frequency $\Delta\nu_{He}$) produced by the polarized ^{3}He is proportional to the density and polarization of the ^{3}He nucleus:

$$\Delta\nu_{He} = \frac{d\nu_{EPR}}{dB}Cn_{He}\mu_{He}P_{He} \tag{2.7}$$

where $\frac{d\nu_{EPR}}{dB}$ is the coefficient obtained from other experiments, C is a dimensionless

quantity depending on the shape of the sample, and n_{He} is the density of the ^{3}He

nucleus, μ_{He} the magnetic moment of ^{3}He nuclei, P_{He} the average polarization of the

^{3}He sample. When the sample is spherical, as in the case of the pumping chamber in

this experiment,

$$\Delta\nu_{He} = \frac{8\pi}{3}\frac{d\nu_{EPR}}{dB}\kappa_0\mu_{He}P_{He} \tag{2.8}$$

where κ_0 is a constant depending on temperature. Typically in the experiment a

polarization of 52% responds to approximately 16 MHz.

2.9 Hall A Data Acquisition System (DAQ)

Hall A uses the CODA (CEBAF Online Data Acquisition System) to record the data

streams. Three types of data are recorded: 1)the CODA events from the detectors

and beam helicity signal; 2)the Experimental Physics and Industrial Control System

(EPICS) [24] data which are slow, real-time information about the accelerator and

the target; 3)the scalar events read from the trigger supervisor.

The data were first written on a local disk and later kept in the Mass Storage

System (MSS) for long-term storage.

Chapter 3

Optics Calibration

The optics reconstruction of a detector stands for a mapping of the trajectory of a particle at the focal plane to its trajectory when it comes out from the target. The approach of optics reconstruction and the calibration procedures are introduced in this chapter.

3.1   Coordinate Systems

The trajectory of a particle can be described in different coordinate systems demonstrated in the following subsections. A more detailed description of the coordinate systems can be found in the technical notes by Nilanga Liyanage [25].

3.1.1 Hall Coordinate System

Figure 3.1 shows the convention of the Hall A coordinate system. In this system $\hat{z}$ points beam downstream, $\hat{y}$ is vertically up and $\hat{x}$ is to the right of the beam. The origin is defined as the center of the hall (not necessarily the target center).
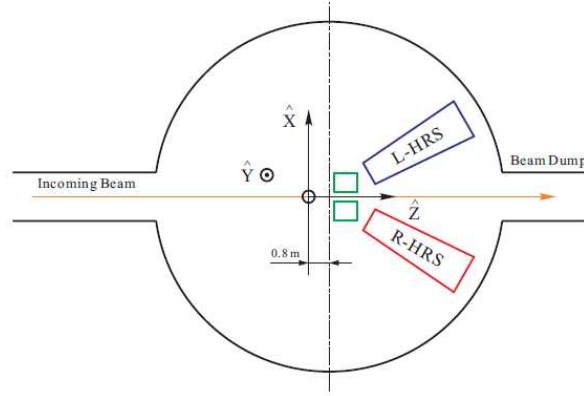
Figure 3.1: Hall A coordinate system (top view).

3.1.2 Target Coordinate System (TCS)

Figure 3.2 shows the target coordinate system. As shown in the figure, $\hat{z}$ is parallel to the spectrometer central ray, $\hat{y}$ is horizontal and points to the left the spectrometer central ray, and $\hat{x}$ points vertically down. The origin of the coordinate system is a point on the $\hat{z}$ axis and it is away from the sieve plate by the surveyed sieve distance (usually around 1 m). Ideally the spectrometer central ray should cross the hall center. Realistically it does not, and the deviation is surveyed to be the spectrometer mispointing. This mispointing is taken into account in the optics calibration. The θ

(θ_{tg}) is the out-of-(scattering)-plane angle, and the ϕ (ϕ_{tg}) is the in-(scattering)-plane angle.

The y_{tg} refers to the position of the trajectory along the $\hat{y}$ direction in the TCS. It is directly associated with the z_{react}, or the position of the reaction along the beamline:

$$z_{react} = -(y_{tg} + D)\frac{\cos(\arctan\phi_{tg})}{\sin(\theta_0 + \arctan\phi_{tg})} + x_{beam}\cot(\theta_0 + \arctan\phi_{tg}) \qquad (3.1)$$

where D is the horizontal displacement of the spectrometer axis from its ideal position, and the spectrometer central angle is denoted by θ_0.

θ_{tg} and ϕ_{tg} describe the outgoing direction of a particle, and they are calibrated with the positions of the sieve holes (y_{sieve} and x_{sieve}). A sieve plate is a blocking metal plate with rows and columns of holes to denote the positions of the penetrating trajectories; it will be introduced in the next section.

$$y_{sieve} = y_{tg} + L\phi_{tg} \qquad (3.2)$$

$$x_{sieve} = x_{tg} + L\theta_{tg} \qquad (3.3)$$

where L is the distance from Hall center to the sieve plane.
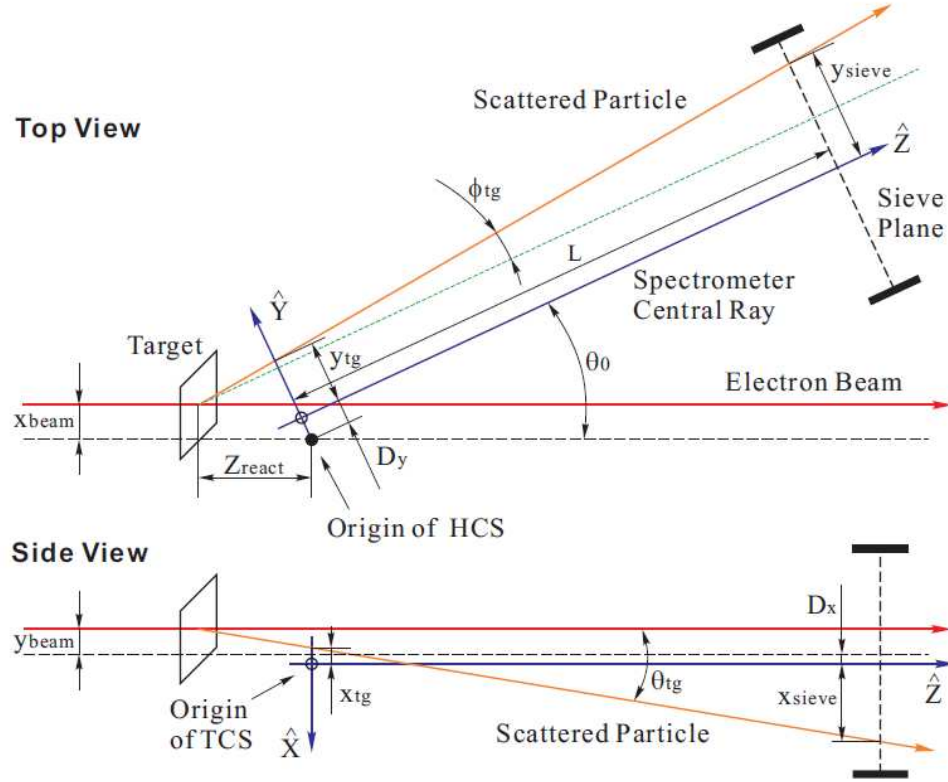
Figure 3.2: Target coordinate system (top and side view).

3.1.3 Detector Coordinate System (DCS)

Figure 3.3 shows the detector coordinate system. It defines the position and direction of the trajectory of a particle at the VDC planes by the detector coordinate variables x_{det}, y_{det}, θ_{det} and ϕ_{det}.

3.1.4 Focal Plane Coordinate System (FCS)

The focal plane coordinate system (fig. 3.4) is obtained by rotating the DCS around its $\hat{y}$ axis by an angle ρ, which is the angle between local central ray and the $\hat{z}$ axis

Top View
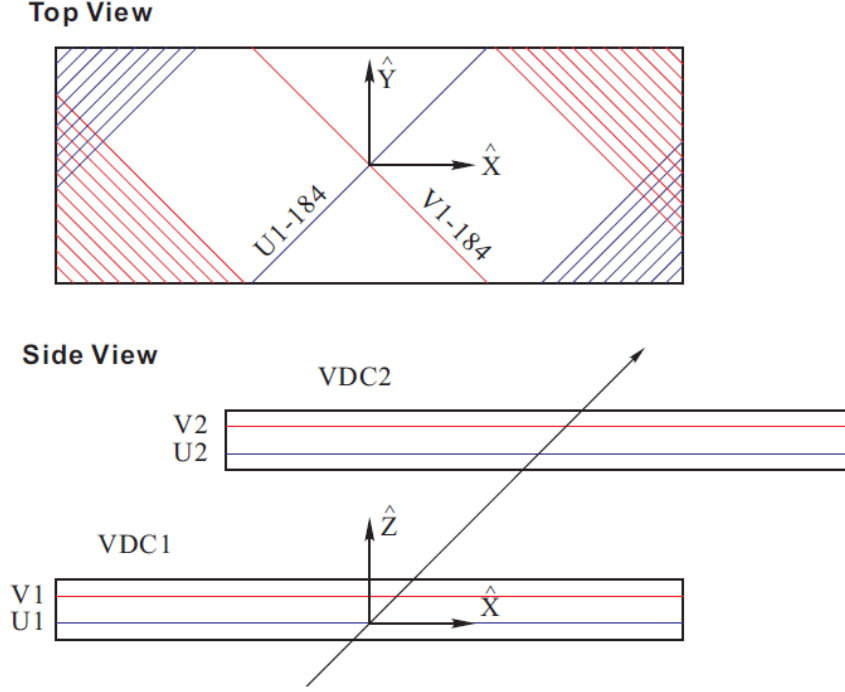
Side View

Figure 3.3: Detector coordinate system (top and side view).

of the DCS. As a result the $\hat{z}$ axis of the FCS rotates as a function of the relative

momentum $\frac{\Delta p}{p_0} = \frac{p-p_0}{p_0}$. ($p_0$ is the momentum setting of the HRS, p is the momentum

of a particle, $\Delta p = p - p_0$.) FCS is served as a bridge between DCS and TCS to make

the converging process faster in the calibration.

3.2 Matrix Approach

The detector variables (x_{det}, y_{det}, θ_{det} and ϕ_{det}) are corrected for any detector offsets

to obtain the focal plane variables (x_{fp}, y_{fp}, θ_{fp} and ϕ_{fp}). In practice, the matrix
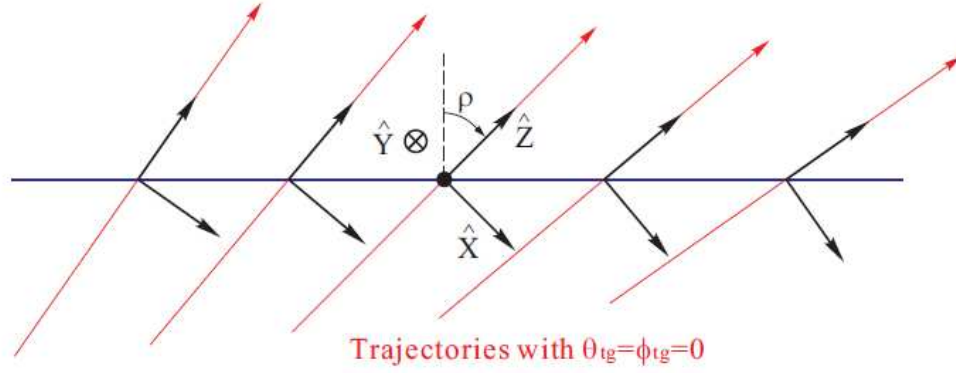
Figure 3.4: Focal coordinate system.

approach connects the focal plane variables with the target coordinate variables according to[1]

$$y_{tg} = \sum_{j,k,l} Y_{jkl}\theta_{fp}^{j}y_{fp}^{k}\phi_{fp}^{l}, \tag{3.4}$$

$$\theta_{tg} = \sum_{j,k,l} T_{jkl}\theta_{fp}^{j}y_{fp}^{k}\phi_{fp}^{l}, \tag{3.5}$$

$$\phi_{tg} = \sum_{j,k,l} P_{jkl}\theta_{fp}^{j}y_{fp}^{k}\phi_{fp}^{l}, \text{ and} \tag{3.6}$$

$$\delta = \sum_{j,k,l} D_{jkl}\theta_{fp}^{j}y_{fp}^{k}\phi_{fp}^{l}, \tag{3.7}$$

where the tensors $Y_{jkl}, T_{jkl}, P_{jkl}$ and D_{jkl} are polynomials in x_{fp}. For example,

$$Y_{jkl} = \sum_{i=0}^{m} C_{i}x_{fp}^{i}. \tag{3.8}$$

Mid-plane symmetry of the spectrometer requires that $(k + l)$ is odd for Y_{jkl} and

---

[1]The superscripts denote the power of each focal plane variable.

P_{jkl}, while $(k+l)$ is even for D_{jkl} and T_{jkl}.

3.3   Extended Target Correction

The basic matrix approach ignores the dependence of the reconstruction of the target variables on the beam $x4$ and y position, and the spectrometer angle. This is a reasonable approximation on a short target. However, with a 40 cm long target used in E05102, an extended target correction must be used to take into account the dependence on the beam position. The dependence on the vertical position of the beam is non-trivial, whereas the dependence on the horizontal position of the beam and on the spectrometer angle vanishes to the first order. The class module THaExtTgtCor in the Hall A Standard Analyzer contains the non-trivial dependence:

$$\frac{d\theta_{tg}}{dx_{tg}} = -0.61 \tag{3.9}$$

$$\frac{d\delta_{tg}}{dx_{tg}} = 1/5.18 \tag{3.10}$$

where x_{tg} represents the height of the beam. The dependence on y_{tg} vanishes to the first order. The dependence on the beam position has been taken into account in the optimization program.

3.4   Optimization Procedures

The optimization was undertaken by Jin Huang's C++ optimization code, LOptic-sOpt [26]. This code uses ROOT class TMinuit to achieve the minimum quadratic variance defined as $\sigma^2 = \Sigma(x - x_{nominal})^2$. Iterations have been done over the optimization of the four target variables and the final σ^2 converge within 8%.

Events are selected for optimization. Selected events are cut out graphically from focal plane plots, and an ASCII file $tree2ascii$ extracts the variables of the sampled events from the ROOT tree and writes them into an ASCII file. It is highly desirable that the graphical cuts shall be made narrow to avoid the noisy or low-quality events, since a small number of low-quality events will magnificently affect the σ^2 by their big $(x - x_{nominal})^2$ values.

Procedures in the optimization include the sieve, the z_{react}, and the momentum calibration.

Survey reports are needed to accurately tell the values of the target position, the sieve slit position, the spectrometer angle and its mispointing values.

A trick is worth mentioned in the calibration of the all four TCS variables: to select equal amount of events for each calibrated sampele. For example, for a 7-foil carbon target, there are always more events in the central foils than the side foils. It is worthwhile to select equal amount of (such as 2000) events for each foil to conducd the calibration. In this way the optimization is not biased in any certain region of the detector acceptance.

3.4.1 Sieve Calibration

The sieve calibration is to calibrate the direction of the trajectory of a particle, or θ_{tg} and ϕ_{tg}.

In Hall A each HRS is equipped with a set of sieve collimators placed around 1.1 m away from the target center along the spectrometer center ray. The sieve is a stainless steel sheet with a pattern of 49 holes (7×7), spaced 25 mm apart vertically and 12.5 mm apart horizontally. Two of the holes, one in the center and one displaced two rows vertically and one horizontally, are 4 mm in diameter. The rest of the holes are 2 mm in diameter. The bigger holes were designed to clearly tell the orientation of the sieve plate during calibration (see fig. 3.5). The positions of the sieve holes represent the direction of a trajectory. The optimization procedure uses the reconstruction of a sieve pattern to calibrate the direction of a trajectory. The direction is described by θ_{tg} and ϕ_{tg}. The reconstructed sieve pattern is compared with the nominal sieve pattern to find the minimum.

A $E_{beam} = 2.425$ GeV run with the sieve plate in and a 7-foil carbon target was used to calibrate θ_{tg} and ϕ_{tg}, and the outcome database is demonstrated to work on a run of 1st pass beam ($E_{beam} = 1.245$ GeV). A 7-foil carbon target is a target made of 7 ^{14}C foils, each foil equally spaced over a total length of 40 cm. The reason of using a 7-foil carbon target is because this target gives out a clear position of the reaction point along the $\hat{z}$ direction, and the unrastered beam used in this run can reduce the uncertainty in the beam position.
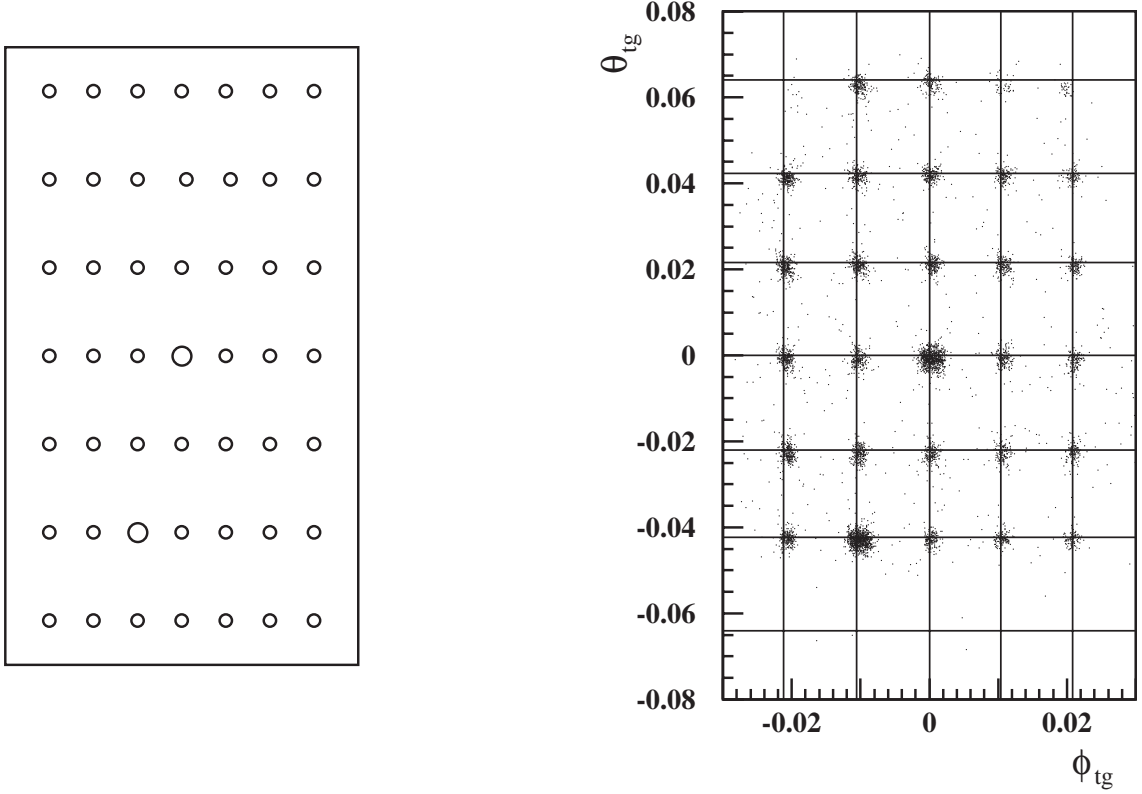
Figure 3.5: Geometric (left) and reconstructed (right) configurations of the sieve slit. The large holes, which allow for an unambiguous identification of the orientation of the image at the focal plane, can be clearly identified in the right figure. The reconstruction shown here is a demonstration from the Hall A NIM paper [19]; it is not the work of optics in this thesis.

The calibration work is finished for both HRS's. Figure 3.6 shows the HRS-L sieve pattern in a run 3483 with $E_{beam} = 2.425$ GeV after calibration, and fig. 3.7 shows the result of the same matrix in run 1454 with $E_{beam} = 1.245$ GeV. Figure 3.8 shows the HRS-R sieve pattern in run 20366 with $E_{beam} = 1.245$ after calibration.
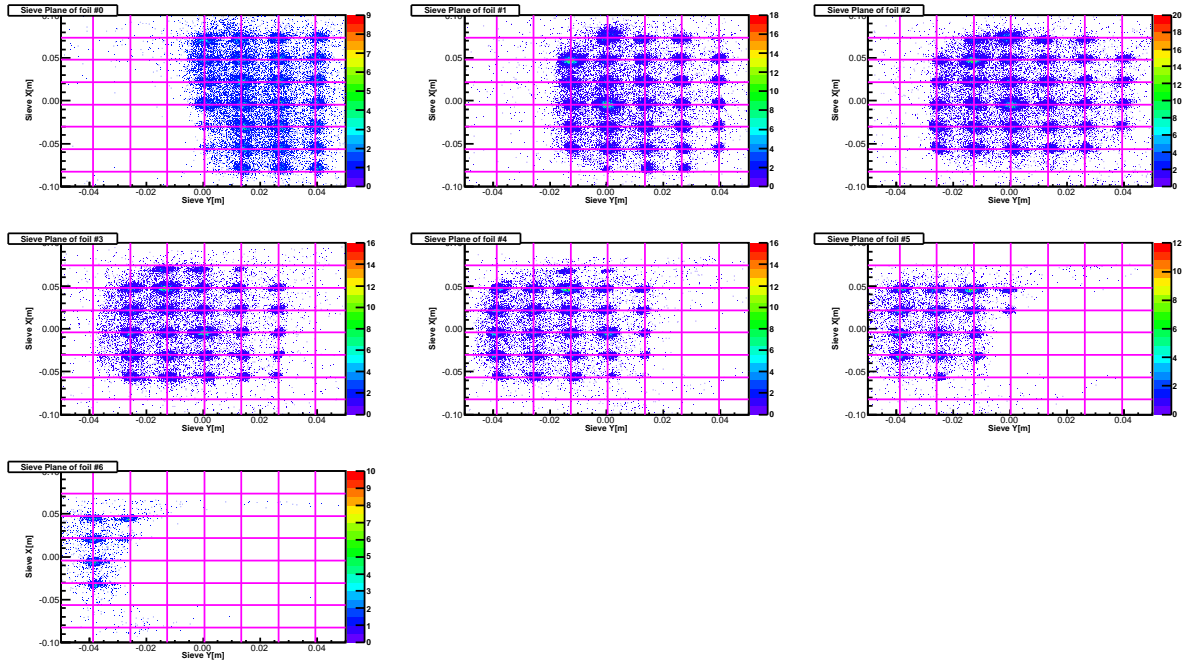
Figure 3.6: A reconstructed sieve pattern of run 3483 with $E_{beam} = 2.425$ GeV on a 7-foil carbon target, and the HRS-L angle at $12.5°$. The patterns labeling from 0 to 6 represent the events from the most upstream foil to the most downstream foil.
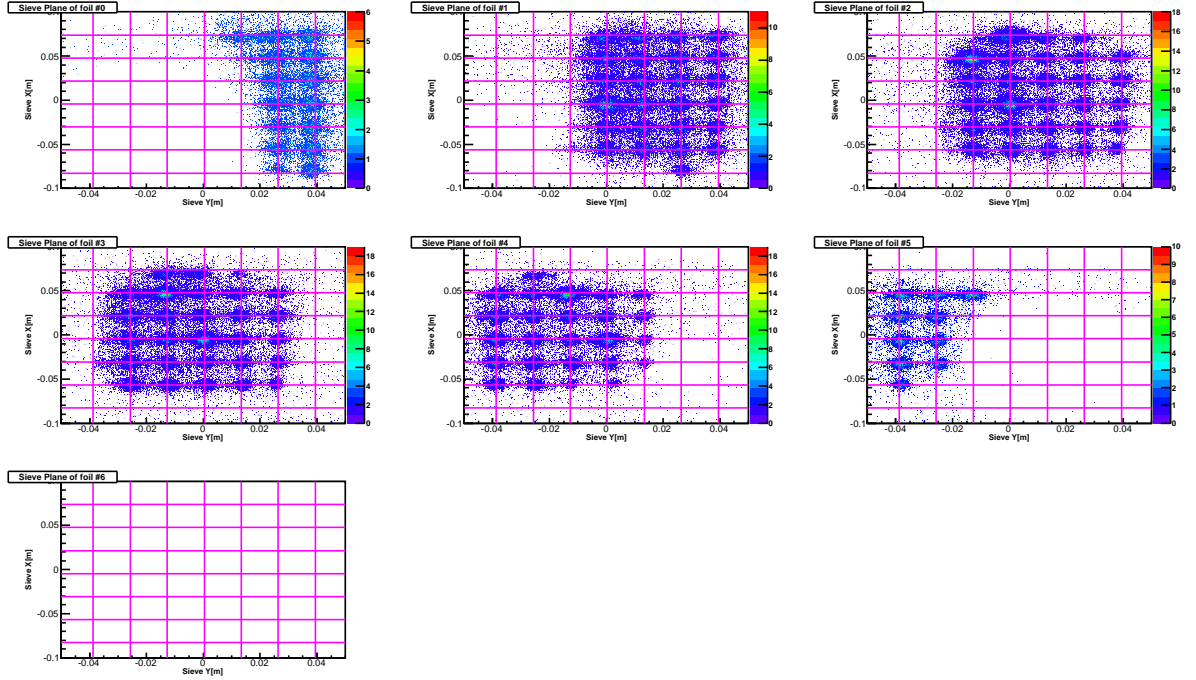
Figure 3.7: A reconstructed sieve pattern of run 1454 with $E_{beam} = 1.245$ GeV on a 7-foil carbon target, and the HRS-L angle at $17°$. The patterns labeling from 0 to 6 represent the events from the most upstream foil to the most downstream foil.
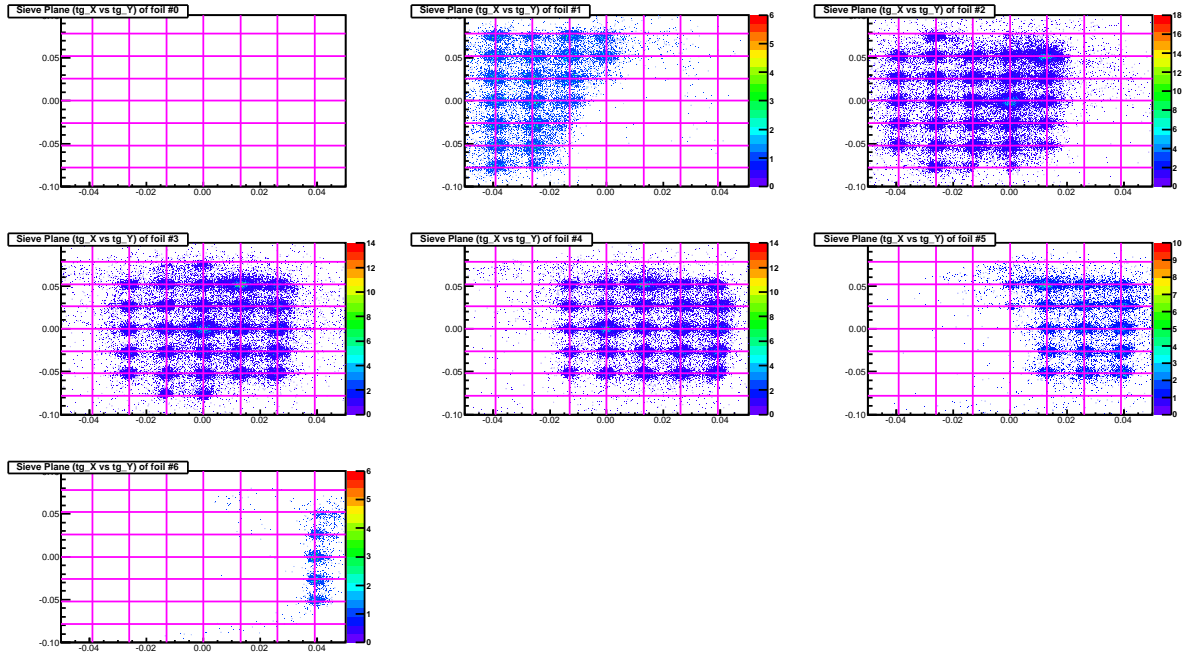
Figure 3.8: A reconstructed sieve pattern of run 20366 with $E_{beam} = 1.245$ GeV on a 7-foil carbon target, and the HRS-R angle at 17°. The patterns labeling from 0 to 6 represent the events from the most upstream foil to the most downstream foil.

3.4.2 z_{react} Calibration

The z_{react} is given by eq. (3.1), which refers to the z coordinate of the reaction position, or the reaction position along the direction of the beamline. It is closely associated with the y_{tg} reconstruction since the y_{tg} is almost the projection of z_{react} on the y axis of the TCS, as shown in fig. 3.2. This calibration is taken from runs on the 7-foil carbon target.

The calibrated matrix is applicable for HRS-L from $E_{beam} = 1.245$ to 3.606 GeV, and the spectrometer central angle from 12.5° to 17°, as shown in fig. 3.9, 3.10, 3.11, 3.12, 3.13. The matrix of HRS-R also applies universally from $E_{beam} = 1.245$ to 3.606 GeV, and the spectrometer central angle from 16° to 18°, as shown in fig. 3.14, 3.15, 3.16, 3.17, 3.18. In these plots the blue lines represent the nominal positions of the 7 carbon foils. The peaks to the left of the most upstream foil (left foil) are caused by the events from the BeO target window.
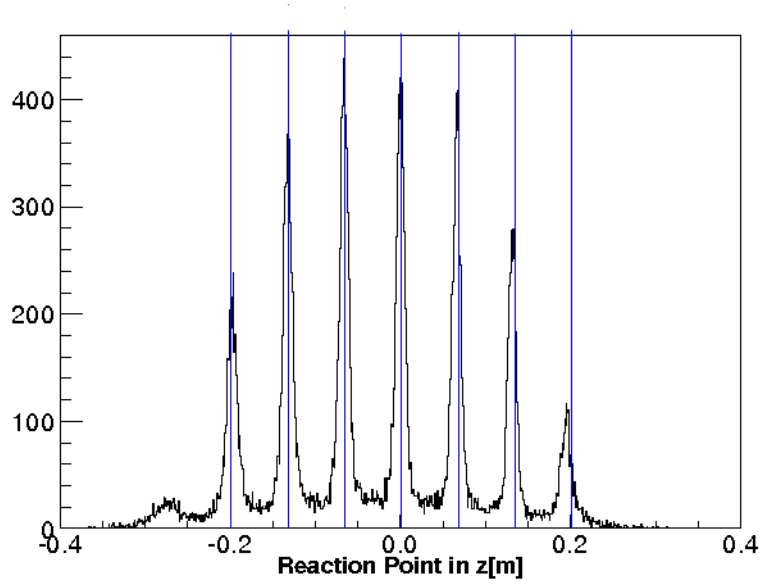
Figure 3.9: A reconstructed 7-foil carbon target at $E_{beam} = 1.245$ GeV and the HRS-L central angle at 17°.
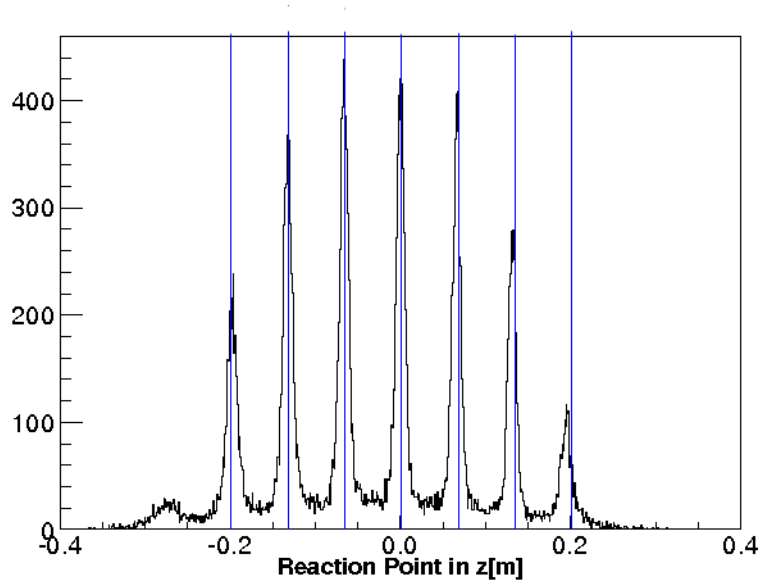
Figure 3.10: A reconstructed 7-foil carbon target at $E_{beam} = 3.606$ GeV and the HRS-L central angle at 17°.
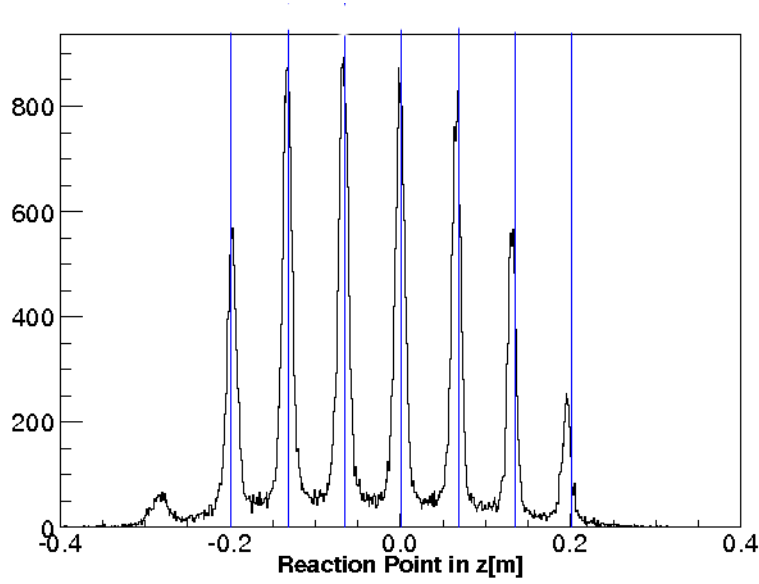
Figure 3.11: A reconstructed 7-foil carbon target at E_{beam} = 2.425 GeV and the HRS-L central angle at 17°.
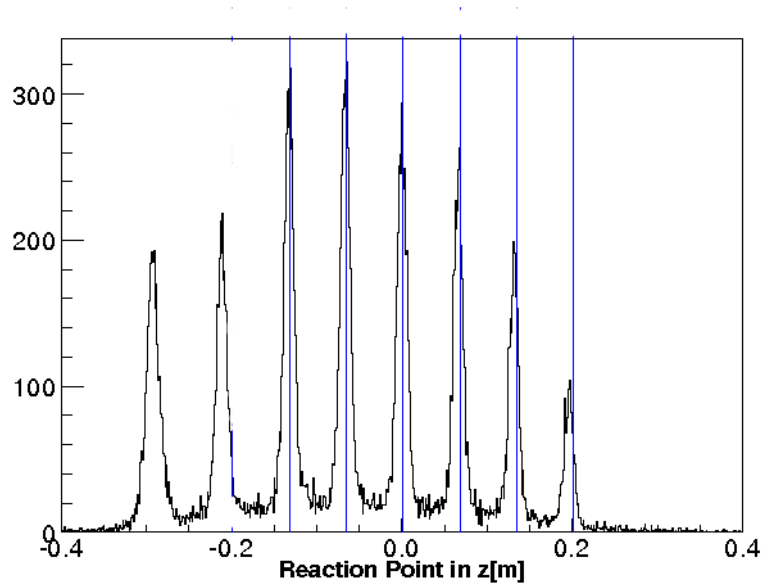
Figure 3.12: A reconstructed 7-foil carbon target at E_{beam} = 2.425 GeV and HRS-L angle at 14.5°. Note that the most upstream foil was mistakenly displaced in the experiment and its nominal position is not shown.
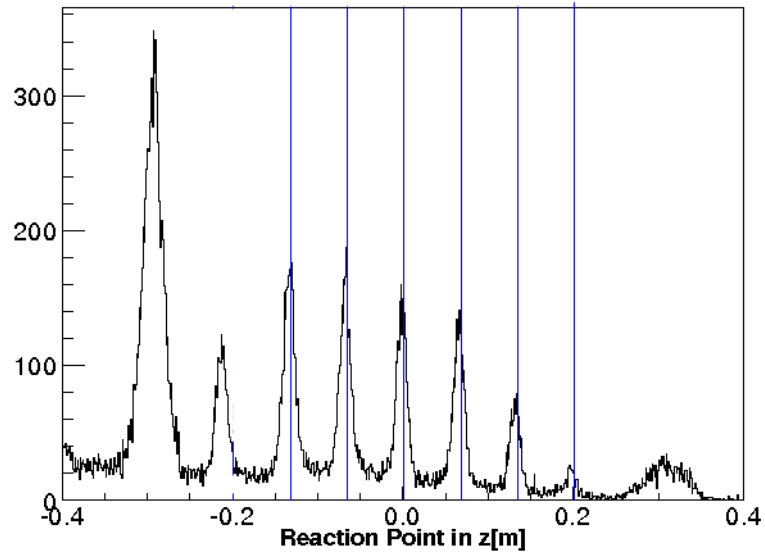
Figure 3.13: A reconstructed 7-foil carbon target at $E_{beam} = 2.425$ GeV and HRS-L angle at 12.5°. Note that the most upstream foil was mistakenly displaced in experiment and its nominal position is not shown.
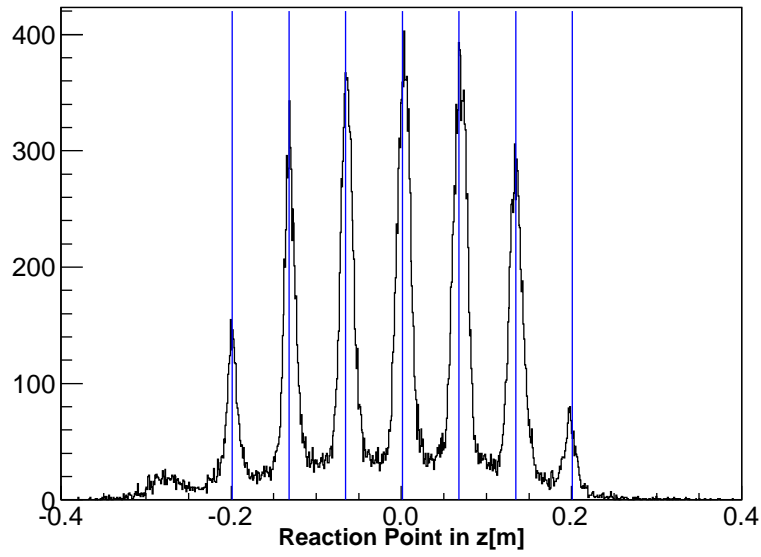
Figure 3.14: A reconstructed 7-foil carbon target at $E_{beam} = 1.245$ GeV and the HRS-R central angle at 17°.
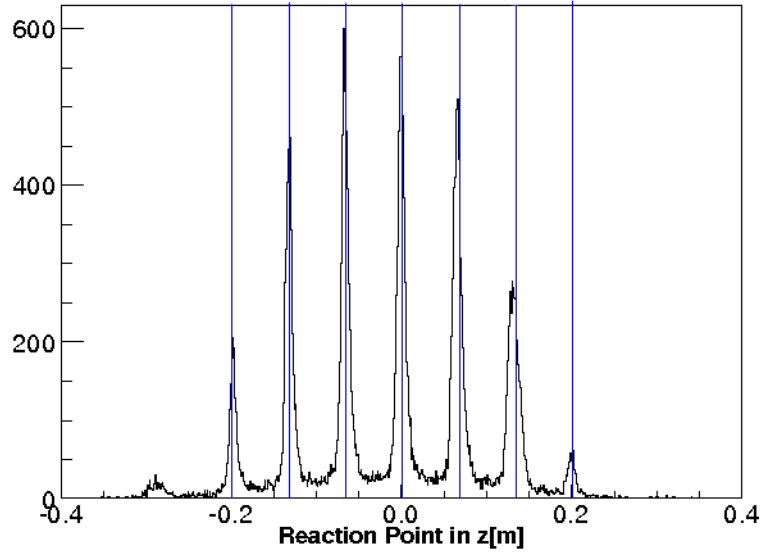
Figure 3.15: A reconstructed 7-foil carbon target at $E_{beam} = 2.425$ GeV and the HRS-R central angle at 17°.
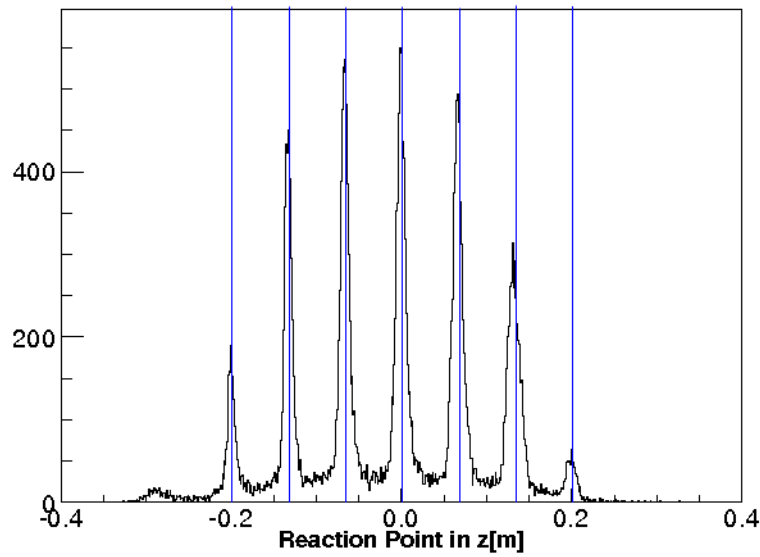
Figure 3.16: A reconstructed 7-foil carbon target at $E_{beam} = 3.606$ GeV and the HRS-R central angle at 17°.
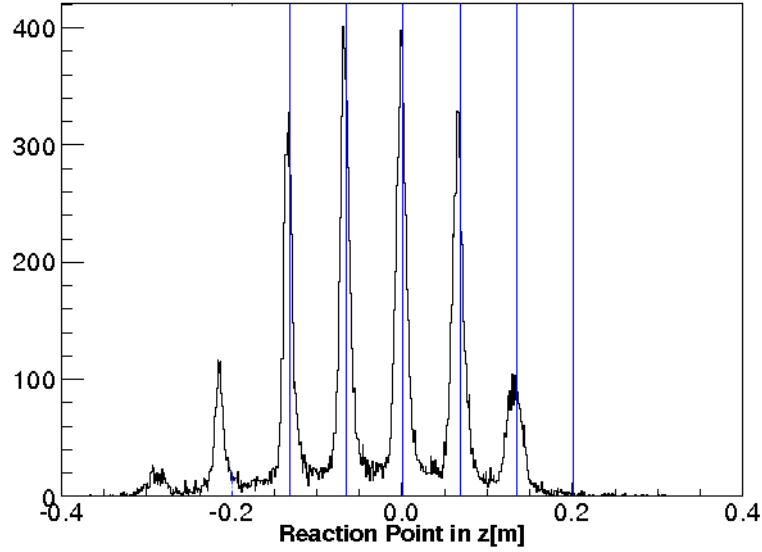
Figure 3.17: A reconstructed 7-foil carbon target at E_{beam} = 2.425 GeV and HRS-R central angle at 16°. Note that the most upstream foil was mistakenly displaced in the experiment and its nominal position is not shown. Particles scattering from the most downstream foil were blocked by the Helmholtz coils for the target, hence there is no events reconstructed for this foil.
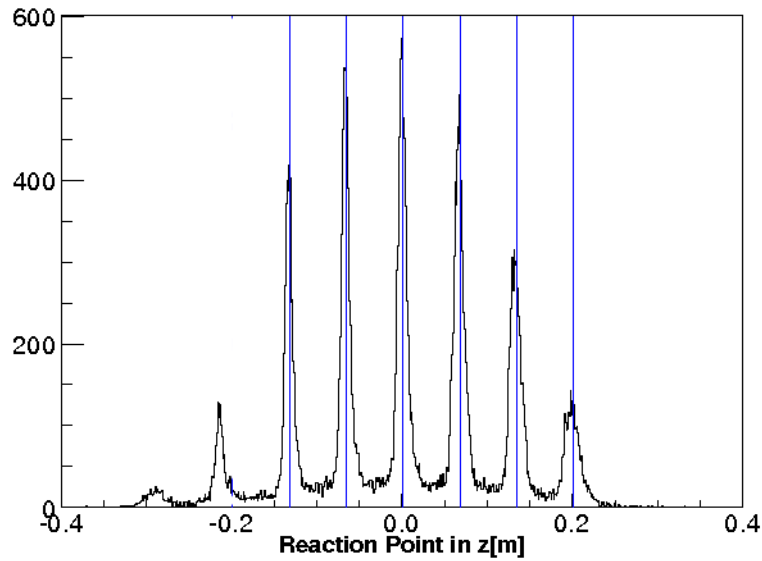
Figure 3.18: A reconstructed 7-foil carbon target at E_{beam} = 2.425 GeV and HRS-R central angle at 18°. Note that the most upstream foil was mistakenly displaced in the experiment and its nominal position is not shown.

3.4.3 Momentum Calibration

Formulism

The momentum calibration is based on the rigorous elastic electron-nucleon scattering formula, in which the scattering electron momentum $p(M, \theta)$ is:

$$p(M, \theta) = E' = \frac{E}{1 + E/M(1 - \cos(\theta))} \tag{3.11}$$

where E, E' are the incident and scattering electron energy, respectively, and M is the target or nucleon mass, θ is the scattering angle. This formula can be used to calibrate the momentum of the outgoing electron from electron-nuclei elastic scattering.

In the experiment $dp = \frac{p(M,\theta) - p_0}{p_0}$ is actually calibrated, where p_0 is the HRS momentum setting.

Due to the finite angular acceptance of the HRS, the scattering angle of an event is not really identical to the spectrometer central angle θ_0. A modified momentum dp_{kin} is thus introduced and is defined as

$$dp_{kin} = dp - \frac{p(M, \theta_{scat}) - p(M, \theta_0)}{p_0} \tag{3.12}$$

where θ_{scat} (the scattering angle in physics) can be calculated as

$$\theta_{scat} = \arccos(\frac{\cos \theta_0 - \phi_{tg} \sin \theta_0}{\sqrt{1 + \theta_{tg}^2 + \phi_{tg}^2}}) \tag{3.13}$$

Equation (3.12) removes the dependence of momentum on the spectrometer acceptance, and all calibrated momenta dp_{kin} are equal to the case as if θ_{tg} and ϕ_{tg} were 0.

Elastic Carbon Scattering, dp_{kin} Calibration

The momentum of an electron scattering off a carbon nuclei can be calculated by eq. (3.11). The scattering peaks represent different carbon excited states. The scattering from the 1st excited state was chosen in the calibration since it has the biggest cross section. 3 momentum settings (-3%, 0%, 3%) of the HRS were taken consecutively to cover the momentum acceptance. This is called the δ-scan, or momentum scan. The calibration was done with $E_{beam} = 1.245$.

The outcome of the scan is in fig. 3.19 for the HRS-L and fig. 3.20 for the HRS-R. The three plots correspond to the 3 momentum settings, and the green lines in the plots from right to left represent nominal scattering momentum from ground state of carbon, 1st excited, 2nd excited state, etc., respectively, and the peaks represent the according scattering dp_{kin}.

Hydrogen Elastic Scattering, dp vs ϕ_{tg} Check

After the δ-scans on carbon target was done, similar scans were undertaken on hydrogen elastic scattering for fine tuning. Runs were taken with the reference cell filled with H_2 gas. From eq. (3.11), when the target mass and the beam energy are de-
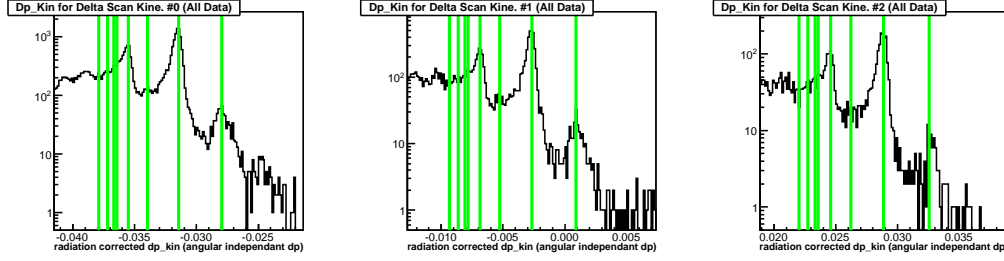
Figure 3.19: δ-scan on a carbon target, HRS-L at $E_{beam} = 1.245$ and the HRS central angle at $17°$.
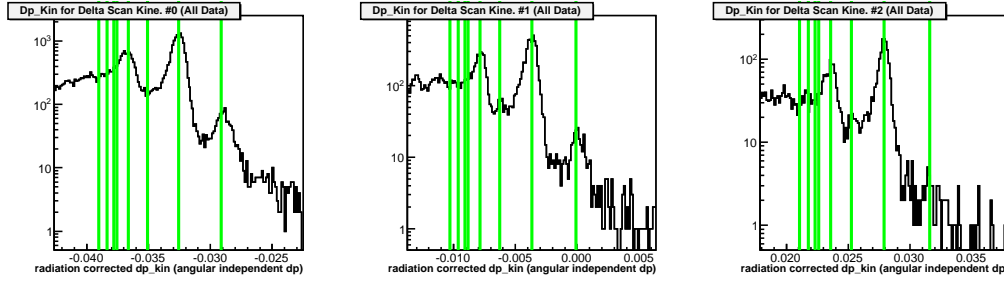
Figure 3.20: δ-scan on a carbon target, HRS-R at $E_{beam} = 1.245$ and the HRS central angle at $17°$.

termined, there is a clear dependence of the scattering momentum on the scattering angle, dominated by ϕ_{tg}. This theoretical dependence is shown in the black lines in fig. 3.21 to fig. 3.24.

The δ-scan covered 3 dp points: -3%, 0%, and 3% at $E_{beam} = 1.245$. Figure 3.21 for HRS-L and fig. 3.22 for HRS-R show the outcome of this calibration. The three plots correspond to the 3 momentum settings, and the black line is the theoretical dependence of the scattering momentum on ϕ_{tg}.

Similar δ-scans were also undertaken when $E_{beam} = 2.425$, with dp ranging between -2% and 2%. Figure 3.23 shows the scan results of HRS-L and fig. 3.24 shows the scan results of HRS-R.
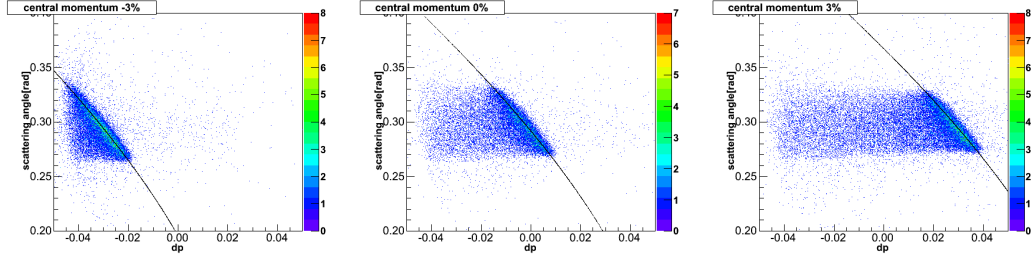
Figure 3.21: δ-scan of the hydrogen elastic scattering on HRS-L, $E_{beam} = 1.245$ and the HRS central angle at 17°.
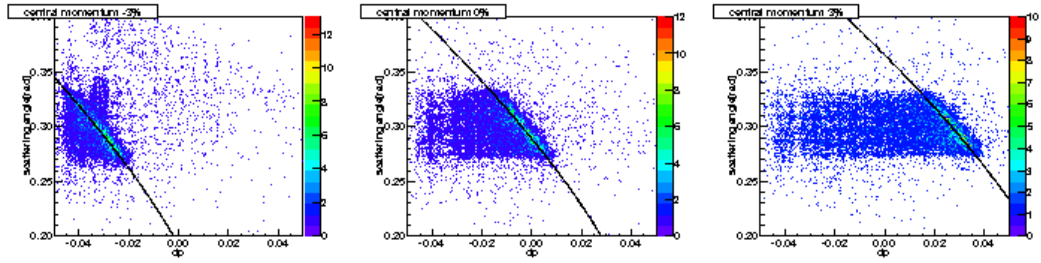
Figure 3.22: δ-scan of the hydrogen elastic scattering on HRS-R, $E_{beam} = 1.245$ and the HRS central angle at 17°.
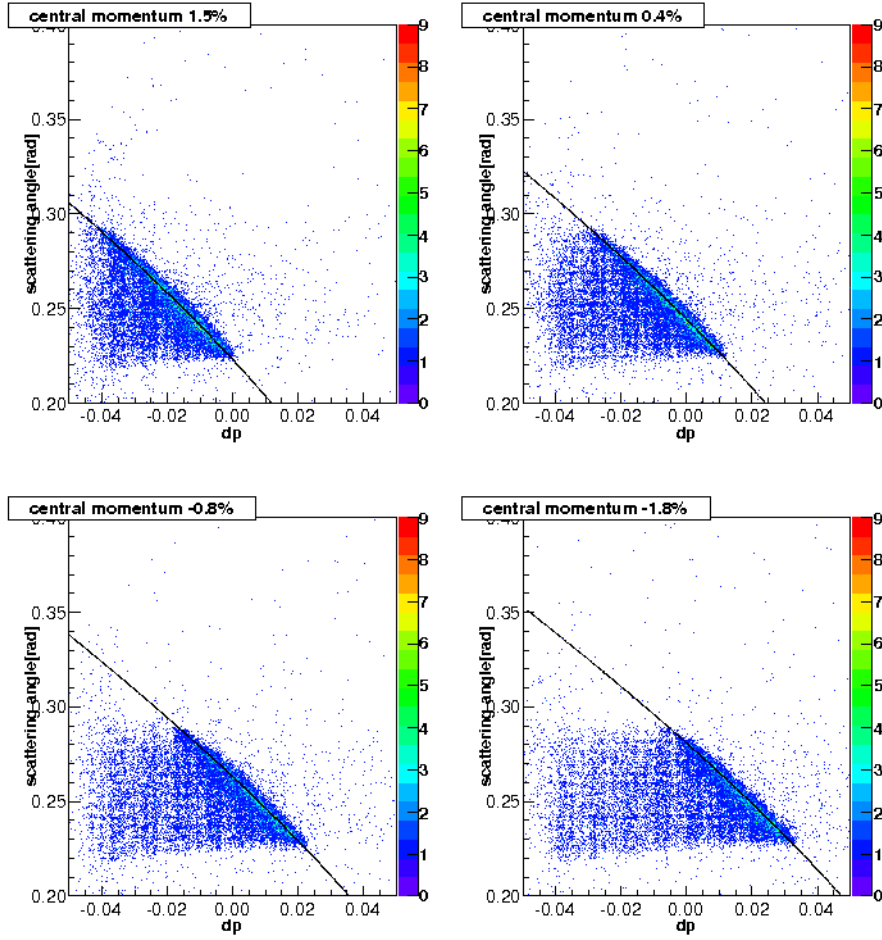
Figure 3.23: δ-scan of the hydrogen elastic scattering on HRS-L, $E_{beam} = 2.425$ and the HRS central angle $14.5°$.
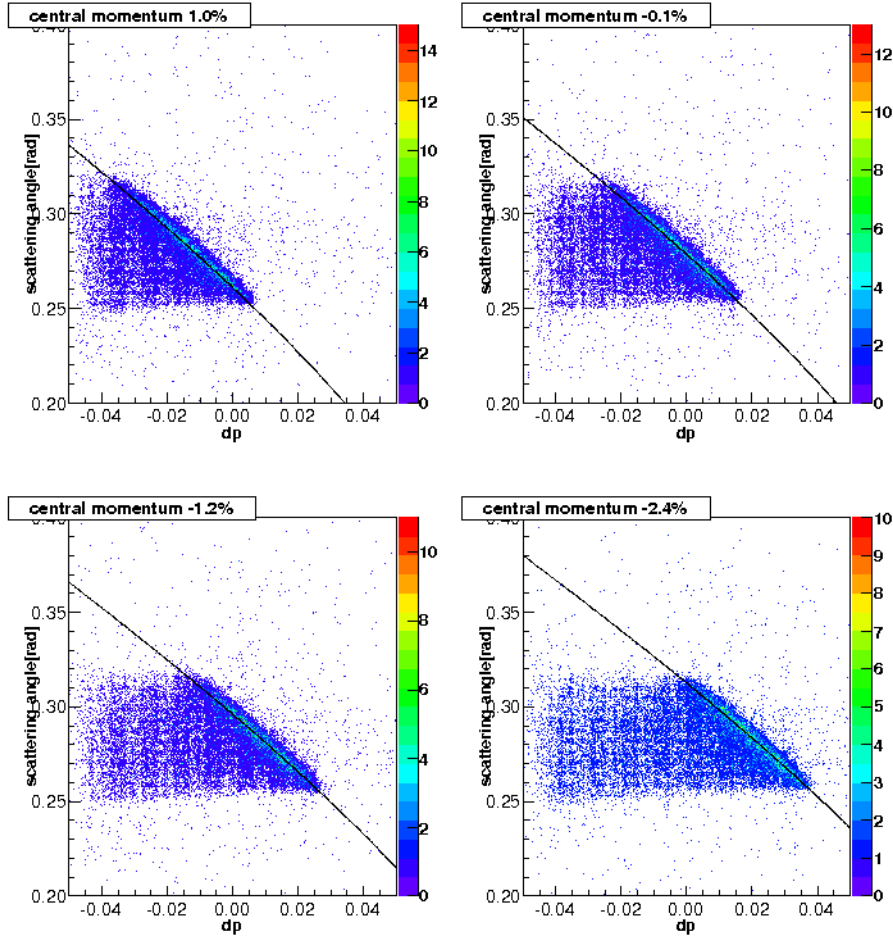
Figure 3.24: δ-scan of the hydrogen elastic scattering on HRS-R, $E_{beam} = 2.425$ and the HRS central angle at $16°$.

3.4.4   Resolutions

The resolutions from the optimization are generalized in table 3.1. The resolutions in the table are the standard deviation σ of the Gaussian fit of peaks in the corresponding target variables.

For z_{react}, the σ just corresponds to the σ of each peak of the carbon foils, since the width of each target foil is negligible compared to the resolution.

For momentum, the σ corresponds to the width of the peak of the 1st excited state in electron-carbon scattering, or the 2nd peak from right in fig. 3.19 and fig. 3.20. Physical widths of the excited peaks are not taken into account, hence the σ here can be taken as an upper limit of the resolution of the momentum.

For θ_{tg} and ϕ_{tg}, the resolution is calculated by (FWHM of angular resolution)^2+(hole_radius/L)^2= of reconstructed sieve hole)^2, where the FWHM is short for Full-Width at Half-Maximum. L is the distance from the target center to the sieve plate. Small sieve holes (2 mm in radius) are used in this calculation to deduce uncertainties in the estimate of error.

Table 3.1: HRS optics resolution

Reconstructed variable	Resolution
z_{react}	6 mm
δ (dp/p)	2×10^{-4}
θ_{tg} (out-of-plane)	1.5 mrad
ϕ_{tg} (in-plane)	0.5 mrad

3.5 Avoidance of Over-optimization

Over-optimization refers to the fact that the optimization performs too well at the points used for optmization, while unrealistic effects exist in areas not used for optimization. From the theory of optimization, all data points can be perfectly fit in a polynomial if the order of the polynomial is greater than the number of degrees of freedom, or the number of data points in this case. In the case of over-optimization all data points perfectly fall on the fitted curve, but the curve shapes unrealistically to cover every fitted point.

This work successfully avoided optimization by

1)Higher-order matrix elements are eliminated as much as possible and the orders of the matrices are kept no higher than the succesful matrices used before (such as the matrices in Hall A E89044 experiment). High-order matrix elements were added onto and taken off from the matrices one by one to make sure that each of the elements are indispensable in the reconstruction.

2)The applicability of the matrices at different kinematics also reduces the possibility of over-optimization. The applicability at different kinematics is equivalent to testing the optimization at data points not used in optimization. If all kinematics are satisfied by one matrix, the matrix should not be over-optimized at high probability.

Chapter 4

Analysis

4.1 Analysis Overview

The physical asymmetry is defined as

$$A_{phys}^{qe} = \frac{\sigma_+^{qe} - \sigma_-^{qe}}{\sigma_+^{qe} + \sigma_-^{qe}} \tag{4.1}$$

where A_{phys}^{qe} stands for quasi-elastic asymmetry, σ_+^{qe} and σ_-^{qe} mean cross sections of beam plus and minus helicty states, respectively. The subscript qe stands for quasi-elastic.

The experimental raw asymmetry A_{raw}^{qe} is

$$A_{raw}^{qe} = \frac{Y_+^{qe} - Y_-^{qe}}{Y_+^{qe} + Y_-^{qe}} \times \frac{1}{P_b P_t R} \tag{4.2}$$

$$= A_{exp}^{qe} \times \frac{1}{P_b P_t R} \tag{4.3}$$

where Y_+^{qe} and Y_-^{qe} mean the yields of beam plus and minus helicty states respectively. P_b and P_t represent beam and target polarization, respectively, with values less than 1, and R is the dilution factor, with values between 90% and 1. The dilution factor R relates how much the measured asymmetry is decreased, by the effects of the yield of N_2 gas in the target cell, the yield of the empty target and the yield of the elastic ^{3}He tail. The dilution factor is majorly contributed from the N_2, and the contribution from other factors are negligible, as will be shown in following sections.

The yields Y_+^{qe} and Y_-^{qe} are normalized by the charge in the corresponding helicity states and the detector livetime, e.g.

$$Y_\pm^{qe} = \frac{N_\pm}{Q_\pm T_\pm} \tag{4.4}$$

where $N_\pm$ is the counts, $Q_\pm$ and $T_\pm$ are the charge and the livetime of each helicity state.

However, A_{raw}^{qe} is the not the same as A_{phys}^{qe} due to radiative effects (with the magnitude $\sim 10\%$). Theoretical models are used to calculate the radiative correction.

4.2   Hall A Analyzer

The Hall A Standard Analyzer is a C++ and ROOT based analyzing tool which reads in from raw data files and fills the event variables in ROOT trees. It has modules to incorporate the standard instruments in Hall A such as the beamline, the target, the scaler, and the HRS's (including their trackings). Version 1.5.12 released on Mar 12, 2010 is used in analysis in the thesis.

4.3   Event Cuts

Event cuts in filtering the quasi-elastic events include:

cuts on target variable acceptances:

$$\text{TCut gold} = \text{"ExTgtCor\_R.dp>-0.04 \&\&ExTgtCor\_R.dp<0.04"};$$

$$\text{TCut target} = \text{"ReactPt\_R.z>-0.16 \&\& ReactPt\_R.z<0.16"}$$

$$\text{TCut sieve} = \text{"ExTgtCor\_R.ph<0.03 \&\&ExTgtCor\_R.ph>-0.025 \&\&}$$

$$\text{abs(ExTgtCor\_R.th)<0.06"};$$

cut on trigger type (this cut imposes HRS-R triggered events only):

$$\text{TCut eventtype} = \text{"(D.evtypebits\&2)==2"};$$

cuts on track quality:

TCut track = "R.tr.n==1&&R.vdc.u1.nhit>3&&R.vdc.u1.nhit<7

&&R.vdc.u2.nhit>3 &&R.vdc.u2.nhit<7&&R.vdc.v1.nhit>3

&&R.vdc.v1.nhit<7&&R.vdc.v2.nhit>3 &&R.vdc.v2.nhit<7";

cut on target helicity being valid:

TCut cut = "he3R.IsSpinValid==1";

cuts on pion rejection:

"R.cer.asum_c>400&&R.ps.e>100&&R.sh.e>100&&(R.ps.e+R.sh.e*2.)>2800."

The meanings of the strings in the expressions of the cuts are listed in table 4.1.

Table 4.1: Cut String Variables

variable name [unit]	meaning
ExTgtCor_R.dp	dp, or momentum fraction defined in Chapter 3
ReactPt_R.z [m]	reaction point in z (beamline) axis
ExTgtCor_R.ph [rad]	ϕ_{tg}, in-plane scattering angle
ExTgtCor_R.th [rad]	θ_{tg}, out-of-plane scattering angle
D.evtypebits	event type bits
R.tr.n	number of tracks found in HRS-R
R.vdc.u1.nhit	number of hits in u1 plane in HRS-R
he3R.IsSpinValid	a flag testifying whether the target spin is valid
R.cer.asum_c	ADC channel in Cerenkov detector
R.ps.e	ADC channel in pre-shower detector
R.sh.e	ADC channel in shower detector

It is meaningful to see that preshower and shower need to be used in combination with Cerenkov detector to cut away pions. Figure 4.1 and fig. 4.2 plotted the

preshower versus shower ADC channels. It is seen that pions still persist on the lower-left corner of fig. 4.1 with only Cerenkov cut, whereas they vanish in fig. 4.2 with both Cerenkov and preshower/shower cut.
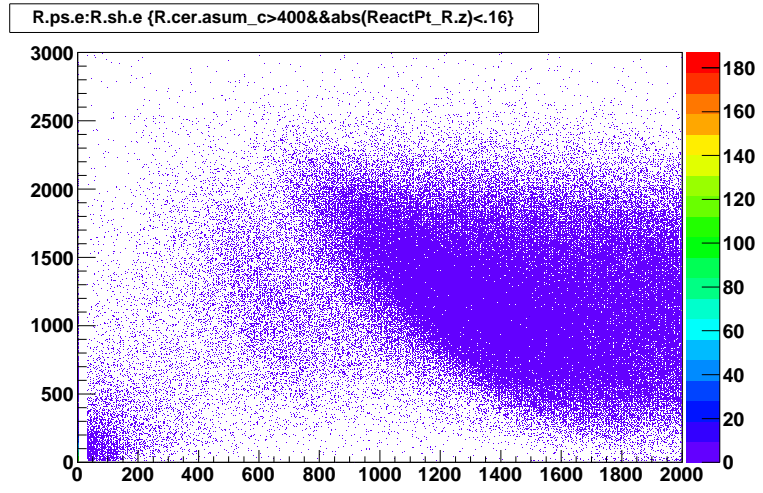
Figure 4.1: Preshower vs shower ADC channels with only Cerenkov cut.
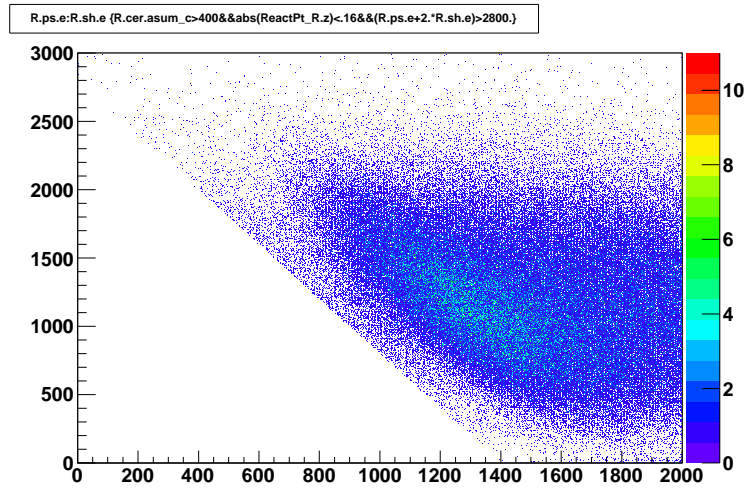
Figure 4.2: Preshower vs shower ADC channels with both Cerenkov and preshower/shower cut.

The physical acceptance selected from the cuts above is shown in fig. 4.3. Labeling plot 1 to 4 for the plots on the first row, and 5 to 8 for the plots in the second row, each plot represents:

Plot 1: momentum fraction dp cut. The violet part is to be analyzed.

Plot 2: z_{react} cut. The violet part is to be analyzed.

Plot 3: θ_{tg} and ϕ_{tg}, without any cuts.

Plot 4: θ_{tg} and ϕ_{tg} with acceptance cuts.

Plot 5: Q^2 with acceptance cuts.

Plot 6: ω with acceptance cuts.

Plot 7: Bjorken x with acceptance cuts.

Plot 8: physics θ and ϕ with acceptance cuts. Note that physics θ is directly associated with ϕ_{tg}, and physics ϕ is directly associated with θ_{tg}.
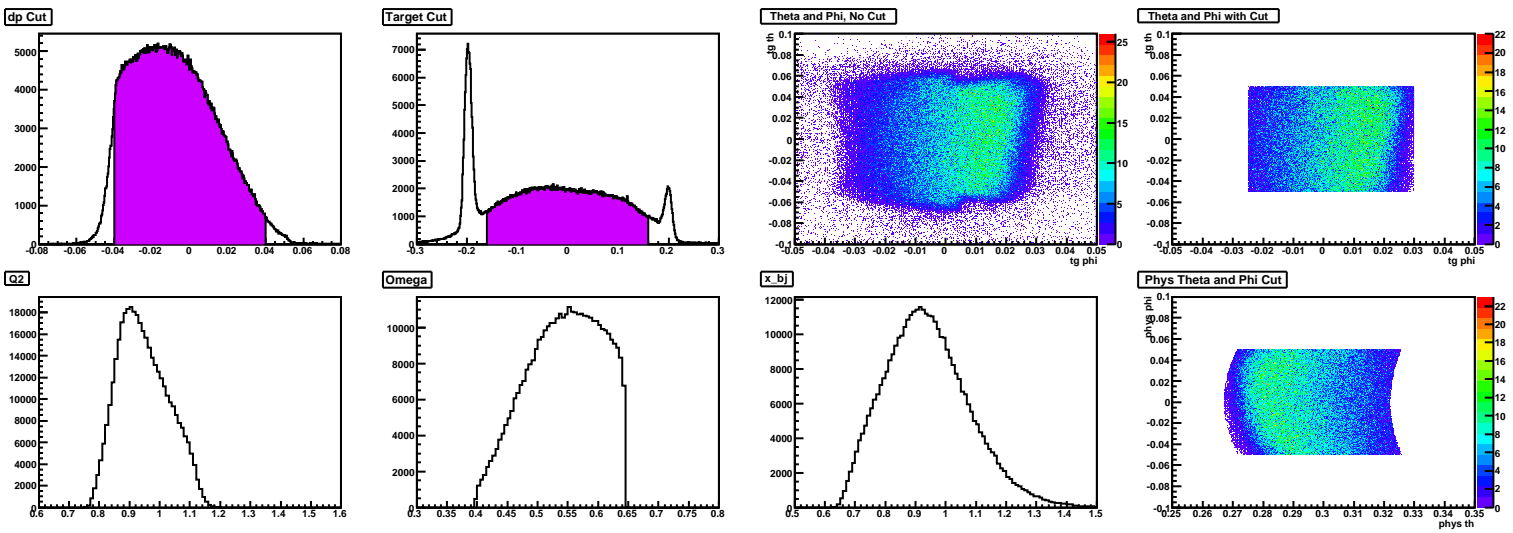
Figure 4.3: Detector acceptance and cuts.

4.4   Beam and Target Polarization

4.4.1   Beam Polarization

The results from the Møller measurements are used for analyzing Experiment E05102. Each Møller measurement has an uncertainty around 2% largely contributed by systematic uncertainties.

Since there was no direct Møller measurement during the run period of this thesis, the beam polarization is obtained by the Hall A beam polarization and the corresponding Hall B beam polarizations. More specifically, if there are two Hall B Møller measurements P_{B1} and P_{B2} at time t_1 and t_2, correspondingly, and one Hall A Møller measurement P_{A1} at time t_1, the beam polarization P_{A2} in Hall A at time t_2 can be derived from

$$P_{A2} = P_{A1} \cdot \frac{P_{B2}}{P_{B1}} \tag{4.5}$$

given that the two Møller measurements in each individual hall had the same beam energy.

In the analysis t_1 is on April 30, 2009, and t_2 is on June 12, 2009. $P_{B1}=(87.527\pm1.54)\%$, $P_{B2}=(85.279\pm1.48)\%$, and $P_{A1}=(84.1\pm2.0)\%$. The beam energies in Hall A were 3.606 GeV and those in Hall B were 5.979 GeV at both t_1 and t_2. Hence it can be derived that the beam polarization P_{A2} during the runs of this thesis was $P_{A2}=(82\pm3)\%$.

4.4.2 Target Polarization

The run-by-run target polarization NMR calibration at the pumping chamber was finished by Yawei Zhang [27], as shown in fig. 4.4. ^{3}He polarization in the pumping chamber is actually shown in the plot, while there is $\sim 1 - 2\%$ drop from the polarization in the pumping chamber to that in the target cell. This polarization drop needs to be calibrated by water calibration and the project is still ongoing.

From the plot it is seen that the target polarization ranges between 55% and 60% during the majority of the run period, and the longitudinal polarized target is observed to have a higher polarization than the transverse polarized target.

The uncertainty of the polarization signal is expected to be around 4% relatively in Yawei Zhang's target analysis[28], majorly contributed by the constant κ_0 ($\sim 3.0\%$ uncertainty) in Section 2.7, and ^{3}He number density ($\sim 2.7\%$ uncertainty)
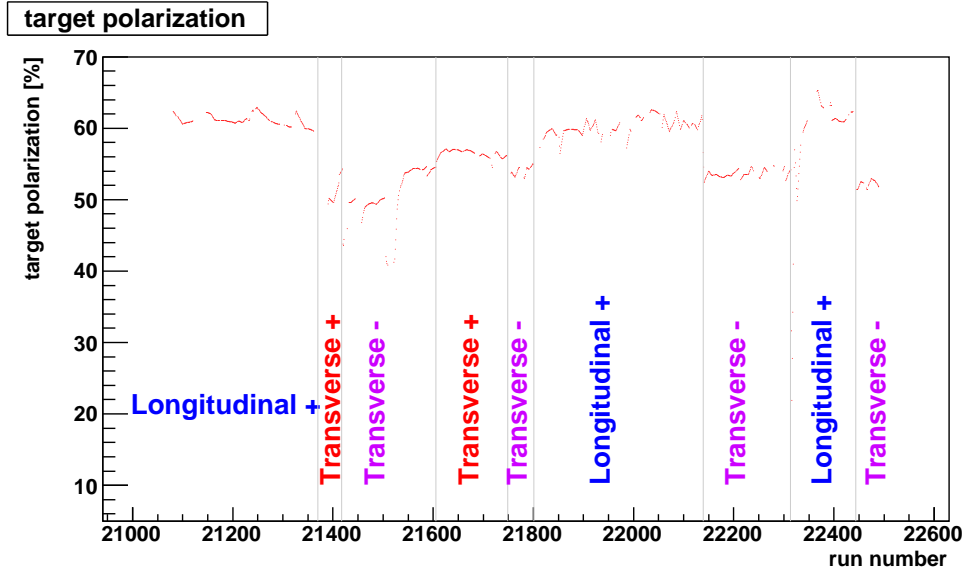
Figure 4.4: Run by run target polarization. Target calibration record is on [29].

4.5   Direction of Target Polarization

The direction of the target polarization is calibrated by Compass calibration, or the calibration of the magnetic field generated by 3 coils in 3 directions. The work is done by Andrej Leban [30] and Miha Mihovilovic [31] from the University of Ljubljana.

The currents in the 3 coils generating the magnetic field can be read from their EPICS variables named "DDM45_1disp1_read", "DDM45_2disp1_read", and "DDM45_3disp1_read", and the direction of the magnetic field is calculated accordingly from its generating currents.

The final calibrated direction of the target polarization in the kinematics of this thesis is in table 4.2. Note that the minus sign refers to the right side of the beam, seeing from top of the hall. 0 degree means parallel to the downstream of the beam.

Table 4.2: Directions of target polarization

orientation of polarization	exact direction angle (in degrees)
transverse	-90.5±0.3
longitudinal	-0.2±0.3

4.6 Dilution Factor

4.6.1 Introduction

Around 1% of nitrogen gas N_2 (by number density) is added into the ^{3}He production cell to absorb unwanted photons emitted from Rb decay process which would in turn depolarize the ^{3}He target. The N_2 gas is expected to produce a negligible false asymmetry but will increase the total yield by a couple of percent. The measured asymmetry is thus decreased or "diluted".

The original definition of dilution factor f_{N_2} is

$$f_{N_2} = 1 - \frac{Y_{N_2} - Y_{empty}}{Y_{total} - Y_{empty}} \tag{4.6}$$

where Y_{N_2}, Y_{total} and Y_{empty} are the yield of N_2, the total yield, and the yield of the empty target cell, respectively. The yield Y is defined as

$$Y = \frac{N}{Q \cdot T_{live}} \tag{4.7}$$

where N is the number of counts and Q and T_{live} are the charge collected and the livetime of the detector.

With different beam energies the ratio of cross sections may differ, so the dilution factor is also a function of beam energy.

2 methods can be used to extract the dilution factor: the pressure curve method

and the quasi-elastic tail matching.

4.6.2   Pressure Curve Method

Mechanism

The reference target cells in the experiment were identical in shape and size to the production target cells, and they were filled with N_2 gas or pure ^{3}He for calibration purposes. When different pressures of N_2 were filled in the reference cell, their yields can be measured correspondingly. After subtracting the yield from the empty target, the pure yield of N_2 is expected to be proportional to the N_2 pressure. This is observed in fig. 4.5, in a set of N_2 pressure curve runs in the e'd experiment with $E_{beam} = 2.425$ GeV.
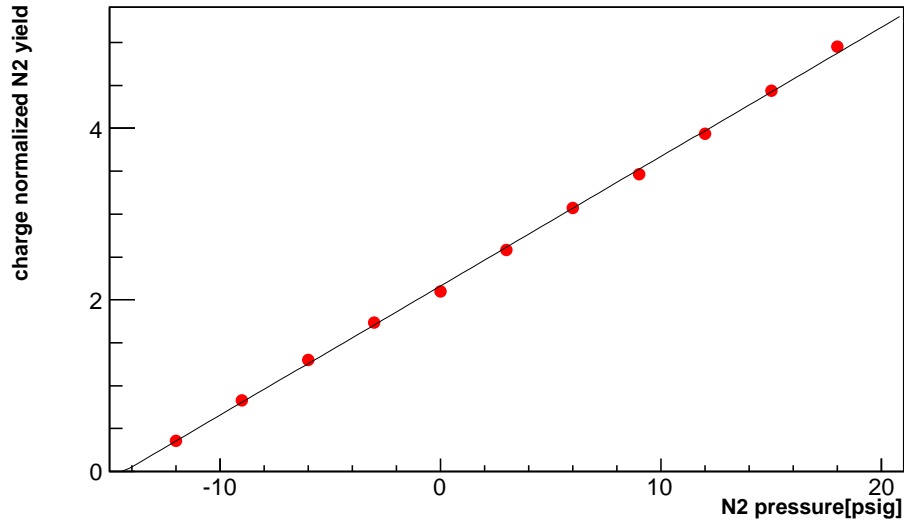
Figure 4.5: Normalized N_2 yield vs N_2 pressure in $E_{beam} = 2.425$ GeV kinematics. The pressures are in unit of psig, or gauged psi, with vacuum pressure being -14.7 psig and 1 atm being 0 psig.

Once the relationship between Y_{N_2} and N_2 pressure is known, one can get the Y_{N_2} in a production cell given the N_2 pressure in the production cell. More specifically, if denoting the slope of fig. 4.5 as k, while k represents the yield of N_2 in a reference cell $Y_{N_2}^{ref}$ divided by N_2 pressure $P_{N_2}^{ref}$ in a reference cell, i.e.,

$$k = \frac{Y_{N_2}^{ref}}{P_{N_2}^{ref}} \tag{4.8}$$

the yield of N_2 in a production cell is

$$Y_{N_2}^{prod} = k \cdot P_{N_2}^{prod} = \frac{Y_{N_2}^{ref}}{P_{N_2}^{ref}} \cdot P_{N_2}^{prod} \tag{4.9}$$

Equation (4.6) is actually used to calculate the yield of N_2 in a production cell and f_{N_2}.

The slope k can be obtained by fitting the pressure curve with a few pressure data points. When the pressure curve is not available, i.e. not many data points were taken at different N_2 pressures, at least 1 data point should have been taken to determine the slope, by forcing the linear fit pass the point where 0 pressure meets 0 yield. Bigger uncertainties exist in this method due to the uncertaities in the calibration of the "0 pressure".

In this experiment only runs with $E_{beam} = 2.425$ GeV had N_2 pressure curves. The dilution factor of the runs with $E_{beam} = 1.245$ or $E_{beam} = 3.606$ GeV are obtained from their single N_2 pressure data points.

Number Density Calibration

In this thesis gas density is in the unit of amagat, 1 amg $= 2.686\ 7774 \times 10^{25}$ m^3 $=$ 44.614 981 mol/m^3 is the Loschmidt constant. When working with the gas density in the target, it is important to differentiate the "filling density" and the cell density. Due to the temperature gradience between the pumping chamber and the target cell, the gas density in a target cell is not the same as the gas density initially filled with, or the "filling density". When density, temperature, volume are denoted as n, T and V, respectively, and underscripts p and t denote the pumping chamber and the target cell, the relationships of density can be roughly described as

$$n_p = \frac{n_0}{1 + \frac{V_t}{V_{tot}}\left(\frac{T_p}{T_t} - 1\right)} \tag{4.10}$$

$$n_t = \frac{n_0}{1 + \frac{V_p}{V_{tot}}\left(\frac{T_t}{T_p} - 1\right)} \tag{4.11}$$

where V_{tot} refers to the total volume.

By the equation above the N$_2$ filling density and the cell density are calculated and shown in table 4.3. Here the Dominic cell refers to the target cell in Ay experiment, and the Moss cell refers to that in e'd experiment. The measurement is done by a JLab group [29].

The N$_2$ pressure in the reference cell p^{ref} is calculated by its temperature T^{ref} and its number density η^{ref} from eq. (4.12). The temperatures are measured by the

Table 4.3: N_2 density measurements

	Dominic (amg)	Moss (amg)
Filling density	0.116±0.010	0.113±0.010
Cell density	0.152±0.014	0.1494±0.014

temperature sensors (RTDs). Normal temperatures in the experiment were 38-39^0C.

$$p^{ref} = \eta^{ref} \cdot p_0 \frac{T^{ref}}{T_0} \tag{4.12}$$

where p_0=14.7 psi is 1 atmosphere and T_0=273.15K.

Results

By the pressure curve method the dilution factor f_{N_2} is shown in table 4.4. The biggest uncertainty is contributed by the pressure gauge reading and the uncertainty of the N_2 density in the production cell.

Table 4.4: Results of N_2 dilution factor by pressure curve method in e'd experiment, or Moss cell

beam energy (GeV)	dilution factor (%) measured by HRS-L	dilution factor (%) measured by HRS-R
1.245	98±2	96±2
2.425	96±2	96±2
3.606	96±2	96±2

4.6.3   Quasi-elastic Tail Matching

This method requires accepting ^{3}He elastic events. Theoretically, pure ^{3}He should produce negligible events beyond the ^{3}He elastic peak, or at $x_{Bjorken} > 3$. The definition of $x_{Bjorken}$ can be found in Section 4.8. However, non-trivial amount of events can be observed beyond ^{3}He elastic peak in the experiment. These events are believed to be the quasi-elastic peak generated by ^{14}N. The shape of the event distribution at this Bjorken x region is observed to be the same with the shape of the pure N_2 runs.

Based on this one can match the shape of the tail of a production run with a pure N_2 run, and get the dilution factor by looking at the difference under the ^{3}He quasi-elastic peak. This difference is directly associated with dilution factor near the ^{3}He quasi-elastic peak.

Results of this method can be shown in fig. 4.6, with the kinematics of a $E_{beam} = 2.425$ GeV in a HRS-L run. Labeling the 6 plots in this figure as 1 to 6 from left to right in the first row, and from left to right in the second row, the meanings of each plot are explained below.

Plot 1 shows the tail matching, where the green represents a pure N_2 run and the black represents a production run. Two event distributions have similar shape at $x_{Bjorken} > 3$. It is interesting to see that the ^{3}He elastic peak is not sitting right at $x_{Bjorken} > 3$, but at $x_{Bjorken} = 2.8$. This observation can be explained by the ratiative effects of the ^{3}He elastic events, and the left-skewness of the significantly large quasi-elastic events below the ^{3}He elastic peak.

Plot 2 shows the difference between the black and the green in plot 1, which is the difference between the event distribution of a production run and a scaled pure N_2 run. This difference is expected to be made of pure ^{3}He events.

Plot 3 actually plots 1-f_{N_2}, or the ratio of the yield of N_2 to the total yield (green curve to black curve) in plot 1.

In plot 4, the green curve represents the difference between a production cell yield and a scaled pure N_2 run, and the black curve represents a pure ^{3}He run. They are supposed to match. Actually the shapes have a little difference which can be seen in the subtraction of the two shapes in Plot 5. This difference can be explained by the radiative effects or energy loss. The energy loss in the black curve is less than that in the green curve, hence the green curve is skewed more to the left than the black curve. Thus in Plot 5 the subtraction of green from black is negative at smaller $x_{Bjorken}$ and positive at bigger $x_{Bjorken}$.

Plot 5 shows the difference of the black and the green in Plot 4, in order to make sure that the sum of N_2 yield and ^{3}He run is the total yield. A difference in the number of events (4000 out of 300,000) around the quasi-elastic peak can be seen and have been explained above.

Plot 6 is the result of the dilution factor, with uncertainties estimated to be 2% due to mismatched events.
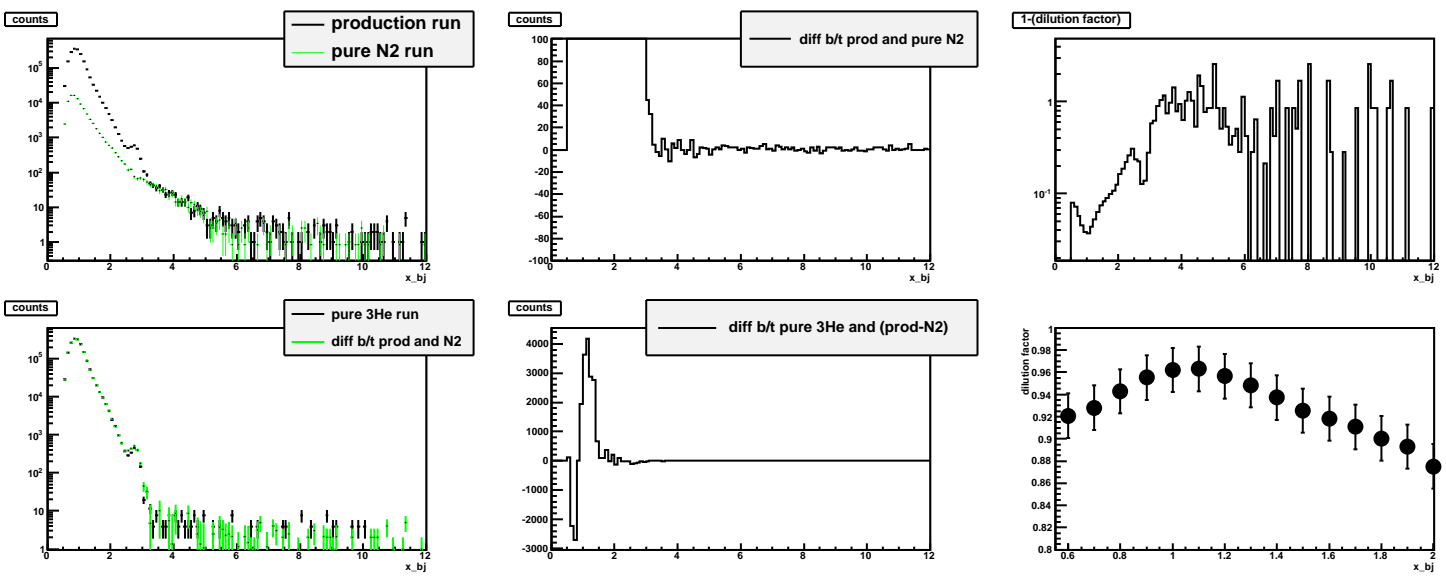
Figure 4.6: Tail matching in a pure N_2 run, a production run, and a pure ^{3}He run.

This tail matching method gives out the dilution factor to be $\sim (96\pm2)\%$ around quasi-elastic peak with $E_{beam} = 2.425$ GeV. The dilution factors of different $x_{Bjorken}$ bins are listed in table 4.5. Uncertainties are mostly contributed by the mismatched counts, and the counts from the empty target.

Table 4.5: Dilution factor f_{N_2} by tail matching method

Bjorken x	Dilution factor f_{N_2}(%)
0.6	$(92.0\pm2)\%$
0.7	$(92.7\pm2)\%$
0.8	$(94.2\pm2)\%$
0.9	$(95.5\pm2)\%$
1.0	$(96.2\pm2)\%$
1.1	$(96.3\pm2)\%$
1.2	$(95.6\pm2)\%$
1.3	$(94.8\pm2)\%$
1.4	$(93.7\pm2)\%$
1.5	$(92.5\pm2)\%$
1.6	$(91.8\pm2)\%$
1.7	$(91.1\pm2)\%$
1.8	$(90.0\pm2)\%$
1.9	$(89.3\pm2)\%$
2.0	$(87.5\pm2)\%$

4.6.4 Empty Target Dilution

An empty target refers to a target with vacuum inside. Ideally an empty target should have zero yield within the analytical acceptance cut. However, small counts persists due to the impurity of vacuum and the reconstructed tails of target windows by optics, as shown in fig. 4.7. After applying the cuts of track quality and pion exclusion, the yield of the empty target is less than 0.3% of production yield and thus has negligible effects on the final asymmetry.
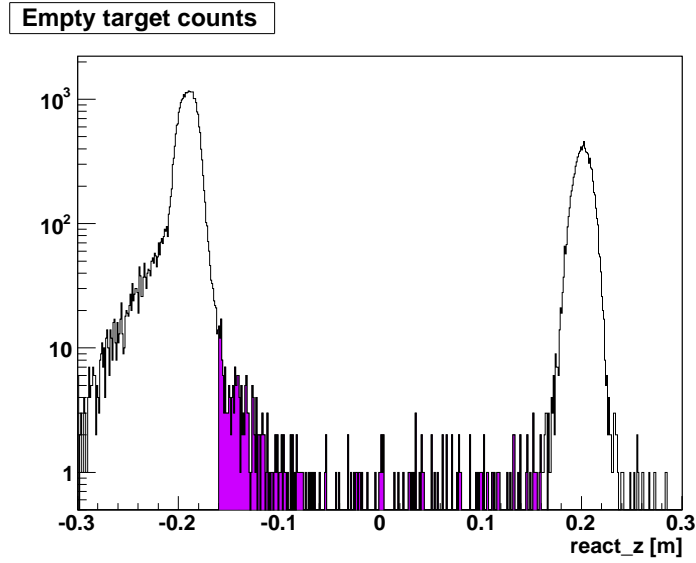
Figure 4.7: The yield of the empty cell on a plot of z_{react}. Black: the yield of the empty cell. Violet: with all acceptance cuts. Note that the extra material to the left of the upstream target window is studied to be ^{4}He coolant jet.

4.6.5 ^{3}He Elastic Tail Dilution

While the quasi-elastic ^{3}He events sit mostly around $x_{Bjorken}=1$ region, the elastic ^{3}He peak sits around $x_{Bjorken}=3$, and the elastic events has some tail extending under the

quasi-elastic peak which can create a false asymmetry. The elastic tail is strengthened by the radiative effects. This elastic tail affects the measured asymmetry in two ways: it dilutes the measured asymmetry and it brings in its own asymmetry to be the false asymmetry. The former is analyzed in this subsection and the latter will be analyzed in the next section.

Figure 4.8 shows the plot of dp_kin of a run with $E_{beam} = 2.425$ and $Q^2=0.26$ $(GeV/c)^2$. It is seen that the magnitude of the elastic peak is around 1/1000 of the quasi-elastic peak. And one can naively estimate that the magnitude of the elastic tail is less than 1/10 of the magnitude of the elastic peak, or less than 1/10000 of the magnitude of the quasi-elastic peak at this kinematics.

One can estimate the elastic cross section in the kinematics of this thesis ($Q^2=1$ $(GeV/c)^2$) by comparing with the kinematics mentioned in the last paragraph. The ^{3}He form factors at $Q^2=1$ $(GeV/c)^2$ decrease by more than a factor of 10 from $Q^2=0.26$ $(GeV/c)^2$ (A.Amroun et $al.$ [32]). The proton and neutron form factors either keep approximately the same or even increase between the two kinematics. So it is estimated that the ratio of the elastic tail to the quasi-elastic peak decrease by more than a factor of 10 from at $Q^2=1$ $(GeV/c)^2$, resulting this ratio to be less than 1/100000. It is concluded that this ratio has negligible effects in the dilution factor.
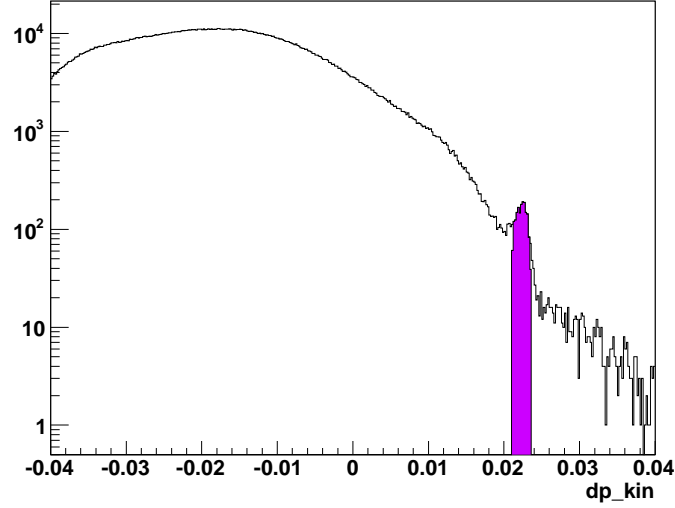
Figure 4.8: The ^{3}He elasic (violet) and the quasi-elastic events plotted by dp_kin at Q^2=0.26 $(\text{GeV/c})^2$.

4.7   Radiative Correction

Radiative correction is undertaken by the Fortran code radcor.f. The original version of the code was based on the formalism by Mo and Tsai [33]. The code was later implemented by Miller [34], and then implemented in JLab Hall A E94010 experiment. The peaking approximation is made by the formalism of Stein, *et al.* [35]. Details of the code are included in [36]. This code can do radiative correction in the polarized and unpolarized cross sections in the case of inclusive inelastic electron scattering from ^{3}He target. The outcome of the code was later compared with formalism in POLRAD [37], the so-called co-variant method. It is found [36] that the two methods are just marginally different.

Radcor.f uses experimental raw cross sections as the input, and it builds up the Born cross section (either polarized or unpolarized) models and radiates this Born

cross section to obtain a radiated cross section. The radiated cross section obtained is compared with raw cross section input. The Born cross section model is then adjusted to reduce the difference in the comparison. This procedure is iterated 10 times and it converges to the final model of Born cross section. The final convergence has the variation of chi-square less than 5%.

Radcor.f only deals with cross sections. In order to do corrections in the asymmetry measurements in E05102, procedures below are taken:

- an unpolarized radiated cross section model is required to create the difference in the polarized cross sections for the radcor.f input;

- with input from above, radcor.f iterates to find the difference between the "unfolded" Born cross sections in 2 helicity states;

- this difference should be further divided by unpolarized Born cross section to obtain the Born asymmetry, or asymmetry without radiative effects;

Since there is no direct cross section measurements in E05102, rough unpolarized cross sections (either radiated or unradiated) are extrapolated from the data in E94010 and eq. (1.12). This does not seem rigorous but it brings in a negligible uncertainty to the final result considering the magnitude of correction in the asymmetries ($\sim 10\%$). The uncertainty is further reduced in the physics extraction in Chapter 5, since only the ratio of asymmetries is needed in the extraction.

Table 4.6 shows the magnitude of the correction in asymmetries. The correction is also shown in the next section in fig. 4.11 and fig. 4.12.

The uncertainties in the radiative correction provided by radcor.f is estimated to be 20% [38] relatively to reflect variations from different models. After including the procedure of extrapolation of cross sections (polarized and unpolarized) described above, one can over-estimate this uncertainty to be 50% relatively without losing much accuracy in final results, as shown in the next chapter.

Table 4.6: Magnitudes of radiative corrections

Bjorken x	Long. correction(%)	Tran. correction(%)
0.924	14±7	13±7
0.976	8±4	11±6
1.035	8±4	10±5
1.066	10±5	11±6

4.8   Raw Asymmetry Results

In the results plotted the horizontal axis represents $x_{Bjorken}$. The scaling variable $x_{Bjorken}$ is defined as $x_{Bjorken} = \frac{Q^2}{2M\omega}$, where Q^2 is the square of the four-momentum transfer, M is the mass of the struck nucleon and ω is the difference of energy between the incoming electron and the outgoing electron.

Figure 4.9 and fig. 4.10 show the measured asymmetries with beam half-wave plate in and out, for transverse and longitudinal target polarization, or transverse and transverse-longitudinal asymmetry, respectively. This asymmetry is not modified by the target or beam polarization, or any other corrections. (Note that since

target polarization is aligned parallel or perpendicular with beamline, the measured asymmetries are not pure transverse or transverse-longitudinal as in the formulas. Instead, the asymmetries include an angular rotation from the pure transverse or transverse-longitudinal case. For easy referencing, in this paper $A_{T'}$ refers to the asymmetry when the polarization of the target is perpendicular with the beamline, and $A_{TL'}$ refers to the asymmetry when the polarization of the target is parallel with the beamline)

Figure 4.11 and fig. 4.12 show the corrected asymmetry along with all corrections near the quasi-elastic peak. Table 4.7 and table 4.8 show the tabulated asymmetries.

The statistical uncertainty of a raw asymmetry δA_{raw} is given by

$$\delta A_{raw} = \frac{2\sqrt{N^+ N^-}}{(N^+ + N^-)^{3/2}} \simeq \frac{1}{\sqrt{N}} \tag{4.13}$$

Where N^+ and N^- represent number of counts in the positive and negative helicity states, respectively.

The systematic uncertainties are dominated by the beam and target polarization, the dilution factor, and radiative correction. Details about systematic uncertainties will be displayed in the next section.
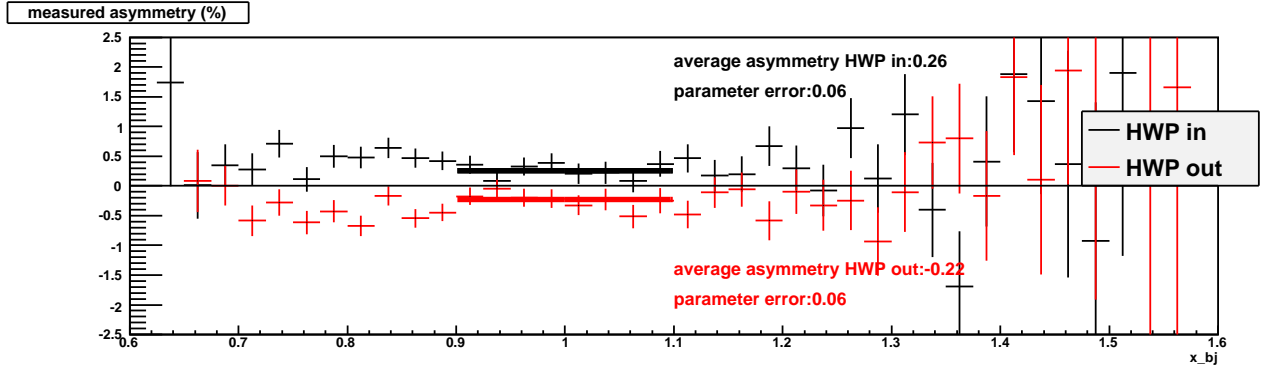
Figure 4.9: Measured transverse-longitudinal asymmetry $A_{TL'}$ without any correction (polarization, dilution factor, or radiative correction)
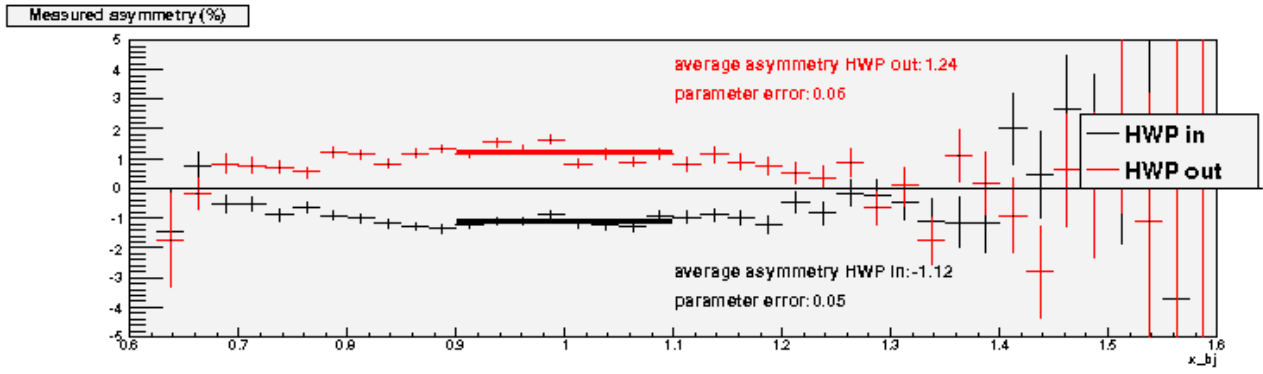
Figure 4.10: Measured tranverse asymmetry $A_{T'}$ without correction (polarization, dilution factor, or radiative correction)
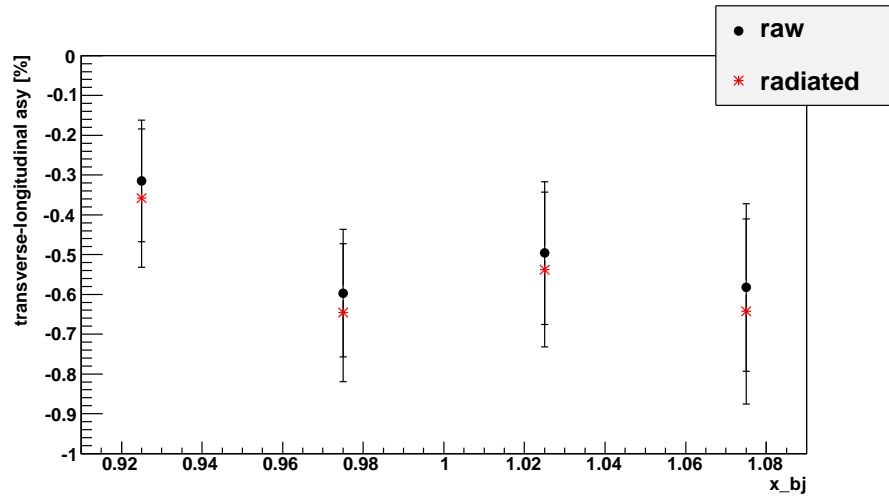
Figure 4.11: Tranverse-longitudinal raw asymmetry (before radiative correction) and asymmetry after radiative correction near quasi-elastic peak. Uncertainties are statistical only.
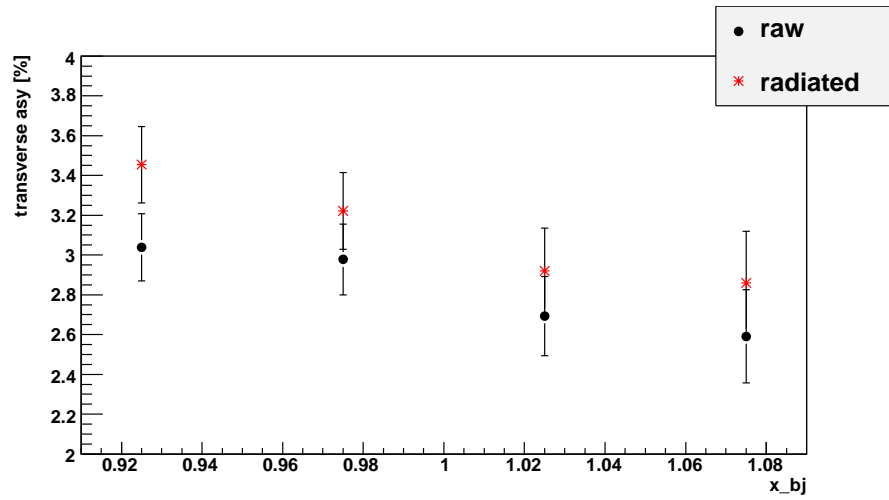
Figure 4.12: Tranverse raw asymmetry (before radiative correction) and asymmetry after radiative correction near quasi-elastic peak. Uncertainties are statistical only.

Table 4.7: Transverse-longitudinal asymmetry: before and after radiative correction.

	Before radiative correction	After radiative correction
Bjorken x	Asym± stat ± syst (%)	Asym± stat ± syst (%)
0.925	-0.32±0.15±0.02	-0.35±0.17±0.02
0.975	-0.60±0.16±0.03	-0.66±0.18±0.05
1.025	-0.50±0.18±0.03	-0.55±0.20±0.04
1.075	-0.58±0.21±0.03	-0.64±0.23±0.05

Table 4.8: Transverse asymmetry: before and after radiative correction.

	Before radiative correction	After radiative correction
Bjorken x	Asym± stat ± syst (%)	Asym± stat ± syst (%)
0.925	3.04±0.17±0.17	3.35±0.19±0.23
0.975	2.98±0.18±0.16	3.29±0.20±0.23
1.025	2.69±0.20±0.15	2.97±0.22±0.21
1.075	2.59±0.23±0.14	2.86±0.26±0.20

4.9 Analysis of Systematic Uncertainties

Below are major parts contributing to systematic uncertainty of the measurements:

- beam polarization ($\sim 3\%$);

- target polarization ($\sim 4\%$);

- dilution factor ($\sim 2\%$);

- radiative correction (less than 5%).

Negligiable uncertainties are discussed below.

- The uncertainties in the asymmetry caused by the beam position and beam current in different helicity states are negligible, due to the stability of the beamline which can be used to make ppm (parts per million) level measurements such as HAPPEX experiment [39].

- About the uncertainties caused by the elastic ^{3}He events: from section 4.6.5 it is seen that the ratio of the yield of ^{3}He elastic to the yield of ^{3}He quasi-elastic under the quasi-elastic peak is less than 1/100000. Considering that the ^{3}He elastic asymmetry at this kinematics is around 4-5%, whereas the quasi-elastic asymmetry at this kinematics is around 0.6-3%, it is concluded that the false asymmetry caused by ^{3}He elastic is negligible.

- The uncertainties caused by the asymmetric DAQ (Data Acquisition System) livetime is negligible. These are analyzed in section 4.9.1.

- The detector inefficiency is reasonably assumed to be helicity-independent.

The uncertainties from kinematics are not taken into account here. They will be considered in the final physical (G_E^n) extraction.

4.9.1   Livetime Asymmetry

The livetime (LT) is defined as a percentage number in eq. (2.4), and the deadtime (DT) is defined as $DT = 1 - LT$. When the event rate is not high and and there are few stacked events (events that coincide to happen in the same time window), the

deadtime can be calculated by the event length t_{event} and the event rate R_{event}:

$$DT = t_{event} \times R_{event} \qquad (4.14)$$

The linearity is also observed in previous experiments ([40]).

The DT in the experiment is $\sim 5\%$. Based on the linearity above, the DT fluctuates with the event rate at a level of a couple of percent (the level of cross section asymmetry). This level of DT fluctuation brings in less than 0.1% (relative) in the livetime asymmetry, hence the false asymmetry of livetime is believed to be a negligible effect in the final results.

Chapter 5

The Extraction of G_E^n

In the case of inclusive quasi-elastic scattering of polarized electrons from ^3He, $^3\vec{H}e(\vec{e}, e')$, the formula for the asymmetry (eq. 1.22) can be written in terms of ^{3}He response functions as

$$A = \frac{\Delta}{\Sigma} = -\frac{\cos \theta^* v_{T'} R_{T'}^{^3He} + \sin \theta^* \cos \phi^* v_{TL'} R_{TL'}^{^3He}}{v_L R_L^{^3He} + v_T R_T^{^3He}} \tag{5.1}$$

where $R^{^3He}$'s are the ^{3}He response functions and the v's are kinematics factors. The subscripts $T'(TL')$ represent transverse (transverse-longitudinal). θ^* and ϕ^* represent the direction of the target spin with respect to $\vec{q}$. These angles are defined in Chapter 1 cited from Donnelly and Raskin [7].

In the case of transverse target spin orientation, or $\theta^* = 0$, the asymmetry

$$A_{T'} = -\frac{\sigma_{Mott} v_{T'} R_{T'}^{^3He}}{\Sigma} \tag{5.2}$$

whereas in the case of longitudinal target spin orientation when $\theta^* = \pi/2$ and $\phi* \simeq 0$, the asymmetry

$$A_{TL'} = -\frac{\sigma_{Mott} v_{TL'} R_{TL'^{3}He}}{\Sigma} \tag{5.3}$$

Different models can be used to calculate the ^{3}He response functions. These include full Faddeev calculations and Plane-Wave Impulse Approximation (PWIA) calculations. To match the statistical uncertainty of this measurement, the extraction of G_E^n/G_M^n in this dissertation will focus on the PWIA method provided by Salme' *et al.*, as described in the next section.

5.1 Salme's Extraction and Its Validity

5.1.1 Formalism of the Extraction

The theoretical layout of the extraction is elaborated on in [4]. This calculation takes into account the relativistic kinematics and currents, and employs the Argonne V18 NN interaction potential and the Hoehler [41] or Krumpelmann [42] nucleon form factor parametrizations. Based on the Plane-Wave Impulse approximation (PWIA, described in the next section) the struck nucleon is repreesnted by a plane wave, and the interaction between the nucleons in the spectator pair is treated exactly by including the Nucleon-Nucleon and the Coulomb interaction between the proton-proton pairs. The prescription for the off-energy-shell electromagnetic nucleon currents by T. De Forest [43] is applied in the calculation. Relativisic corrections include (i) the

relativistic electron-nucleon cross section; (ii) the relativistic energy conservation.

In this calculation [4] the ^{3}He transverse(longitudinal) responses $R_{T'(TL')}^{^3He}$ near quasi-elastic peak can be written as

$$R_{T'}^{^3He} = \frac{Q^2}{2qM}\{2[G_M^p]^2 H_{T'}^p + [G_M^n]^2 H_{T'}^n\} \tag{5.4}$$

$$R_{TL'}^{^3He} = -\sqrt{2}\{2G_M^p G_E^p H_{TL'}^p + G_M^n G_E^n H_{TL'}^n\} \tag{5.5}$$

where $H_{T'(TL')}^{n(p)}$ represents the neutron (proton) contribution to the $T'(TL')$ response functions. These functions in general contain ^{3}He structure within PWIA and the ratios of nucleon form factors. Values of these functions can be seen in fig. 5.1.
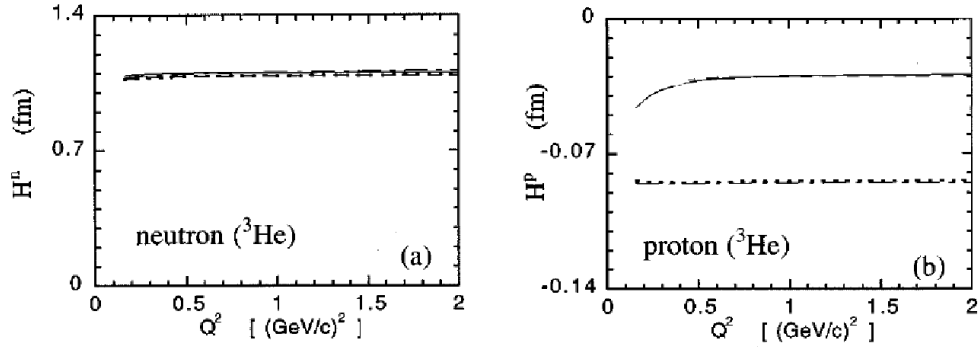
Figure 5.1: Left: $H_{T'(TL')}^n$ in ^{3}He response functions. All curves have been obtained using the Av14 plus Coulomb interaction and the nucleon form factors of [8]. Solid line: $H_{T'}^n(Q^2, \nu_{peak})$; dot-dashed line: $H_{TL'}^n(Q^2, \nu_{peak})$. Right: same as left but for protons

By getting the ratio of eq. (5.3) and eq. (5.2) and inserting eq. (5.4) and eq. (5.5),

the unpolarized cross sections Σ and σ_{Mott} cancel and the outcome is

$$\frac{A_{TL'}}{A_{T'}} = -\frac{v_{TL'}\sqrt{2}\{2G_M^p G_E^p H_{TL'}^p + G_M^n G_E^n H_{TL'}^n\}}{v_{T'}\frac{Q^2}{2qM}\{2[G_M^p]^2 H_{T'}^p + [G_M^n]^2 H_{T'}^n\}} \tag{5.6}$$

Using the measured $A_{T'}$ and $A_{TL'}$ and the world's data for G_M^p, G_M^n, and G_E^p, the value of G_E^n can be extracted.

5.1.2 Discussion of FSI, MEC, and Off-shell Prescription

The Plane Wave Impulse Approximations (PWIA) are:

1) a single nucleon within the target nucleus totally absorbs the energy and momentum of the virtual photon;

2) the "quasi-free" assumption is valid and final-state interactions and other current exchanges are ignored. The outgoing nucleon is treated as plane wave;

3) the target nucleus can be described as a collection of independent particles.

The PWIA doesn't include FSI or MEC. FSI, or the Final State Interaction, describes the interaction between the knocked-out nucleon and the spectator nucleons. The MEC stands for the Meson Exchange Currents in the reaction.

There has been abundant research to study the magnitude of FSI and MEC effects in PWIA. Generally, these two effects are small in the kinematics of the work described in this dissertation.

The scaling variable $x_{Bjorken}$ is defined as $x_{Bjorken} = \frac{Q^2}{2M\omega}$, where Q^2 is the square of the four-momentum transfer, M is the mass of the struck nucleon and ω is the

difference of energy between the incoming electron and the outgoing electron. When $x_{Bjorken}$ is near 1, the stuck nucleon has a momentum of almost zero before absorbing the virtual photon. After absorbing the photon it has a momentum almost equal to that of the virtual photon. Therefore, its kinetic energy is relativistic.

The FSI and MEC effects in $^3\vec{H}e(\vec{e}, e'n)$ were studied by Laget [44] and were found to significantly affect the asymmetries at low Q^2 but to become negligible at $Q^2 > 0.3$ $(\text{GeV}/\text{c})^2$. The work of Miller *et al.* [45] gave additional support to the conclusion that the spin-dependent FSI's are negligible at $Q^2 > 0.3$ $(\text{GeV}/\text{c})^2$.

The effects of FSI's are estimated from the difference between the relativistic PWIA calculation [4] and the nonrelativistic Faddeev calculation with FSI and relativistic corrections included [40]. In [40], the transverse asymmetries $A_{T'}$ were measured between $Q^2 = 0.1$ - 0.6 $(\text{GeV}/\text{c})^2$. In the comparison [46] the FSI corrections to $A_{T'}$ decrease with the increase of Q^2. The estimated uncertainties in the extracted values for $A_{T'}$ due to the neglect of the FSI effects in PWIA are 9.0% and 3.6% for Q^2 of 0.3 and 0.4, respectively, and on the order of 1 to 2% for values of Q^2 between 0.5 and 0.6 $(\text{GeV}/\text{c})^2$ based on an extrapolation beyond a Q^2 value of 0.4 $(\text{GeV}/\text{c})^2$. The decrease of the contribution from FSI's was also shown in previous studies [47][48][49]. Salme' *et al.* also estimated that the effects of FSI's vanish at least as $1/q$, where q is the electron momentum transfer. [50]

The effect of MEC on asymmetries also drops exponentially as Q^2 increases based on Golak's full calculation[51]. In the analysis of the transverse asymmetries $A_{T'}$

between $Q^2 = 0.1$ - 0.6 $(\text{GeV/c})^2$ [46], it was found that the uncertainty due to neglecting the MEC effect in PWIA for $A_{T'}$ at the top of the quasielastic peak was 3.6%, 2.4%, 1.0%, and 1.0% for Q^2 of 0.3, 0.4, 0.5, and 0.6 $(\text{GeV/c})^2$, respectively.

Indeed, it was shown in [46] that the experimental transverse asymmetries $A_{T'}$ differ from PWIA calculation by $\sim$50% at $Q^2 = 0.1$ - 0.2 $(\text{GeV/c})^2$ and the difference is less than one $\sigma \sim 5\%$ at $Q^2 = 0.5$ - 0.6 $(\text{GeV/c})^2$. This difference $\sim 5\%$ can be taken to be the upper limit of the contribution of FSI and MEC in the measurements presented in this dissertation.

As noted previously, the prescription for off-shell cross sections of T. De Forest [43] was applied in the extraction method of work presented here. It is found [52] that different prescriptions produce negligible variations.

5.2 Analysis in the Ratio of Asymmetry $A_{TL'}/A_{T'}$ and its Results

As mentioned in section 4.8 the target polarization of E05102 was not aligned parallel or perpendicular to $\overrightarrow{q}$. Instead, it was aligned with respect to the beam direction and has $\sim 24^0$ with respect to $\overrightarrow{q}$. Here denoting the transverse asymmetry by $A_{T'}$ when target polarization was perpendicular to the beamline (almost parallel with $\overrightarrow{q}$), and the longitudinal asymmetry by $A_{TL'}$ when target polarization was parallel to the beamline (almost perpendicular with $\overrightarrow{q}$), experiment analysis gives out

$$A_{TL'}/A_{T'} = -0.18 \pm 0.032(\text{stat}) \pm 0.011(\text{syst})$$

About systematic uncertainties:

• The target polarization allows $\sim 0.6\%$ uncertainty. The NMR measurements are calibrated by EPR measurements, and the ratio of target polarization eliminates the uncertainty in EPR constants (such as κ_0 and ^{3}He number density in 4.4.2) Only the frequency shift $d\nu$ in EPR measurements will remain in the final uncertainty and it is estimated as $\sim 0.6\%$ uncertainty in Yawei Zhang's target analysis[28].

• Uncertainty in the beam polarization is less than 3% due to polarization fluctuation. Since what matters is the fluctuation of the beam polarization (not the absolute value of the beam polarization), the systematic uncertainty in the ratio is less than the uncertainty in the absolute value of the beam polarization.

• Dilution factor cancels in the ratio and is expected to bring negligible error

• Uncertainty in radiative correction is estimated to be 5%. Previous analysis gives out the uncertainty in radiative correction around 5%. Since the uncertainty is positively correlated in the ratio of asymmetries, hence the uncertainty of the ratio of asymmetries is also estimated to be 5%.

5.3   The Extraction of G_E^n Analysis and Results

The general idea in the extraction of G_E^n is to generate a theoretical ratio of asymmetries, and to match it with the experimental one. The theoretical ratio of asymmetries is calculated at each point over the acceptance by eq (5.1), and is later averaged over

the whole experimental acceptance.

G^n_M is input by Kelly's parameterization [3]. G^p_M and G^p_E are input parameters by J.J.Kelly [3], while forcing the fit to pass the most updated measurement from J.Arrington [53]. In [53] $G^p_M/G_D = 0.9413 \pm 0.0122$ and $G^p_E/G_D = 1.0456 \pm 0.0042$ at $Q^2 = 0.979$ $(\text{GeV/c})^2$.

Kelly's parameterization [3] is like

$$G(Q^2) \propto \frac{\displaystyle\sum_{k=1}^{n} a_k \tau^k}{1 + \displaystyle\sum_{k=1}^{n+2} b_k \tau^k} \tag{5.7}$$

where $G(Q^2)$ represents form factors. In the parameterization both numerator and denominator are polynomials in $\tau = Q^2/4m_p^2$.

Various parameterizations of proton form factors (J. Arrington and I. Sick [54][55]) vary within 2% and mostly have uncertainties less than 2% at kinematics of interest in this thesis.

Since G^n_E is the unknown parameter being extracted and it also varies with Q^2, it is evaluated by its central value at $Q^2 = 0.95$ $(\text{GeV/c})^2$ and a linear extrapolation slope, e.g.,

$$\frac{G^n_E(Q^2)}{G_D} = \left.\frac{G^n_E}{G_D}\right|_{Q^2=0.95 \ (\text{GeV/c})^2} + a \cdot Q^2 \tag{5.8}$$

By Kelly's dipole parameterization of G_E^n [3]:

$$G_E^n(Q^2) = \frac{A\tau}{1 + B\tau} G_D(Q^2) \tag{5.9}$$

where the dipole form factor is given by $G_D(Q^2) = (1 + Q^2/\Lambda^2)^{-2}$ with $\Lambda^2 = 0.71$ $(\text{GeV/c})^2$, $A = 1.70 \pm 0.04$, and $B = 3.30 \pm 0.32$. Given these parameters, the value of a in eq. (5.8) is

$$a = (0.135 \pm 0.007) \ (\text{GeV/c})^{-2}$$

Longitudinal and transverse asymmetries were calculated for every point within the acceptance of the detectors, given the kinematics variables and G_M^p, G_M^n, and G_E^p of the corresponding event. The ratio of asymmetries is computed from a weighted average over the acceptance. Different $G_E^n|_{Q^2=0.95 \ (\text{GeV/c})^2}$'s have been used as the input, and each was used to generate a ratio of asymmetries to match the experimental one. The plot of the generated asymmetry and the input $G_E^n|_{Q^2=0.95 \ (\text{GeV/c})^2}$ is shown in fig. 5.2. The generated asymmetry has systematic uncertaintiess included in table 5.1:

The final G_E^n for an average $Q^2 = 0.95 \ (\text{GeV/c})^2$ is

$$G_E^n/G_D = 0.226 \pm 0.041(\text{stat}) \pm 0.016(\text{syst}) \tag{5.10}$$

Table 5.1: Sources of systematic uncertainty in the simulated ratio of asymmetries

contribution	uncertainty	$A_{TL'}/A_{T'}$
G_E^p	2%	2%
G_M^p/μ_p	2%	2%
G_M^n/μ_n	1.25%	5%
in-plane angle, including θ_{tg} and HRS survey	<2 mrad	$< 0.1\%$
out-of-plane angle, including ϕ_{tg} and HRS survey	<2 mrad	$< 0.1\%$
in-plane target polarization angle, correlated with θ^*	0.3^o	3%
out-of-plane target polarization angle, correlated with ϕ^*	0.3^o	$< 0.1\%$
beam and scattering electron energy	$< 0.2\%$	$< 0.1\%$
total		6%

or,

$$G_E^n = 0.0414 \pm 0.0077(\text{stat}) \pm 0.0032(\text{syst}) \tag{5.11}$$

Here the statistical uncertainty is determined by the number of events and the systematic uncertainty contains the effects of radiative corrections, the uncertainty in generated theoretical ratio of asymmetries (table 5.1), and the uncertainty in the ratio of experimental asymmetries (eq. 5.2). This result is shown in fig. 5.3, along with selected world data.

5.4   Conclusion

In conclusion, an unprecedented technique for measuring G_E^n by inclusive polarized $^3\vec{H}e(\vec{e}, e')$ has been presented. The final result is shown in eqs. (5.10, 5.11). The ex-
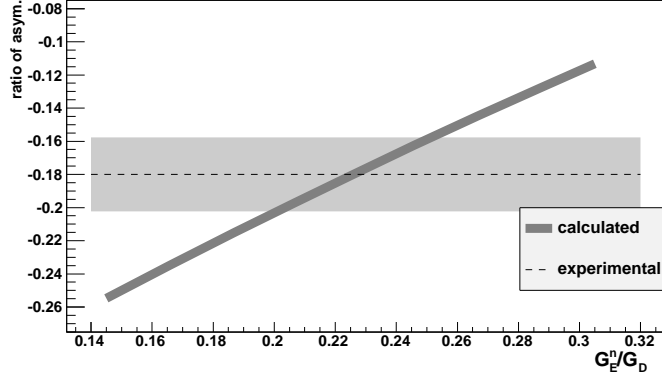
Figure 5.2: Ratio of asymmetries at different input G_E^n/G_D's. Solid: theoretical, the width represents the uncertainty in the calculation). Dotted: experimental, with statistical and systematic uncertainties from the measurement

tracted result agrees well with the world data, showing the feasibility of this extraction technique. One can recall the discrepancy in the proton form factor measurements when the polarization transfer method was introduced in Jefferson Lab [56] for the first time. The agreement between the results of this measurement with those of previous measurements gives us greater confidence in the accuracy of all measurements of G_E^n.

5.5 Comments and Outlook

This method of extracting G_E^n by the ratio of asymmetries has advantages compared to other methods of extracting G_E^n.

First, this method demonstrates its advantage at higher Q^2, e.g. $Q^2 > 1$ $(\text{GeV/c})^2$. From world data as shown in fig. 1.7 [3], all other form factors decrease at $Q^2 > 1$ $(\text{GeV/c})^2$ while in the same region G_E^n increases. Hence, G_E^n in the higher Q^2 region
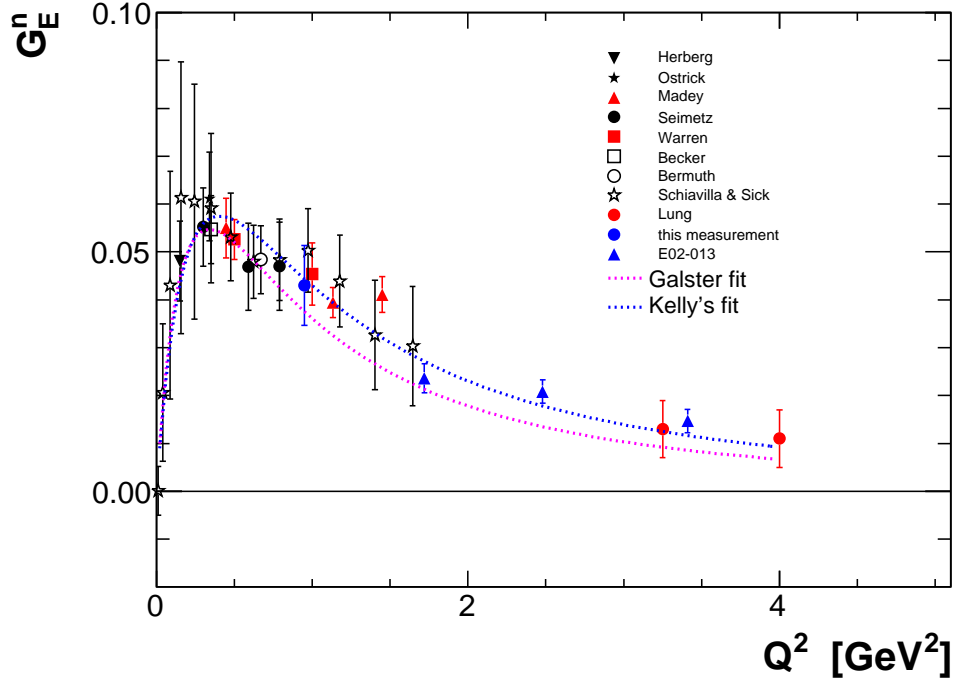
Figure 5.3: G_E^n value from this measurement, with world data and parameterization.

dominates the ^{3}He structure and errors from the contribution of protons decrease.

Second, as mentioned before, this method has small sensitivity to systematic errors. Dilution factors will cancel out when N_2 gas brings negligible false asymmetry, and the beam and target polarizations only matter by their relative magnitude. When the beam and target polarization are calibrated, one always needs to calibrate a constant offset and the slope to map the electronic signals with the polarization number. The offset is usually small, and the polarization number is largely affected by the slope coefficient. The ratio of asymmetry method automatically avoids the dependence on the slope coefficient.

Third, this method proves great potential in saving beam time. The parallel and

the perpendicular polarization data were each taken in less then 30 hours of quality beam time with a beam current of $\sim$13 μA. Due to the magnitudes of $A_{TL'}$ and $A_{T'}$, the statistical error dominates in the $A_{TL'}$ case. By multiplying the beam time by 4 in the $A_{TL'}$ case and keeping the beam time the same for $A_{T'}$, the resulting uncertainty in G_E^n could be cut by half using a total of 150 hours of beam. This requires a 6-day running of continuous beam, or approximately 12-day running in total.

Further theory support will greatly help in increasing the accuracy of the extraction. Right now asymmetries at the quasi-elastic peak are obtained using a weighted averaging around the peak. Further theoretical calculations aimed at determining asymmetries at different kinematics bins around the quasi-elastic peak can provide a way to better match the measured asymmetries with the theoretical calculations.

Bibliography

[1] S. Platchkov *et al.*, Nucl. Phys. **A510**, 740 (1990).

[2] C. E. Jones-Woodward *et al.*, Phys. Rev. **C44**, 571 (1991).

[3] J. J. Kelly, Phys. Rev. **C70**, 068202 (2004).

[4] A. Kievsky, E. Pace, G. Salme, and M. Viviani, Phys. Rev. **C56**, 64 (1997), nucl-th/9704050.

[5] F. Halzen and A. D. Martin, New York, Usa: Wiley (1984) 396p.

[6] A. S. Raskin and T. W. Donnelly, Ann. Phys. **191**, 78 (1989).

[7] T. W. Donnelly and A. S. Raskin, Annals Phys. **169**, 247 (1986).

[8] S. Galster *et al.*, Nucl. Phys. **B32**, 221 (1971).

[9] R. G. Arnold, C. E. Carlson, and F. Gross, Phys. Rev. **C23**, 363 (1981).

[10] T. Eden *et al.*, Phys. Rev. **C50**, 1749 (1994).

[11] J. J. Kelly, Adv. Nucl. Phys. **23**, 75 (1996).

[12] M. Meyerhoff *et al.*, Phys. Lett. **B327**, 201 (1994).

[13] S. Riordan *et al.*, (2010), 1008.1738.

[14] F. R. P. Bissey, A. W. Thomas, and I. R. Afnan, Phys. Rev. **C64**, 024004 (2001), nucl-th/0012081.

[15] B. Blankleider and R. M. Woloshyn, Phys. Rev. **C29**, 538 (1984).

[16] A. K. Thompson *et al.*, Phys. Rev. Lett. **68**, 2901 (1992).

[17] R. Alley *et al.*, Nucl. Instrum. Meth. **A365**, 1 (1995).

[18] D. Marchand, Ph.D thesis, University of Blaise Pascal, Clermont-Ferrand (1997).

[19] J. Alcorn *et al.*, Nucl. Instrum. Meth. **A522**, 294 (2004).

[20] W. Barry, JLab-TN-90-246 (1990); JLab-TN-91-087 (1991). .

[21] K. Unser, IEEE Trans. Nucl. Sci. **28**, 2344 (1981).

[22] A.A.Kresnin, Sov.Phys.JETP 5 288 (1957).

[23] M. Baylac *et al.*, Phys. Lett. **B539**, 8 (2002), hep-ex/0203012.

[24] Hall A EPICS page , http://www.jlab.org/accel/documents/epics_doc.html (2010).

[25] N. Liyanage, Optics calibration of the Hall A high-resolution spectrometers using the new C++ optimizer, JLab-TN-02-012 (2002).

[26] J. Huang, HRS optics optimizer , http://www.jlab.org/~jinhuang/HRSOptics/ (2009).

[27] Y. Zhang, Target polarization calibration, http://www.jlab.org/~yawei/ (2010).

[28] http://www.jlab.org/~yawei/documents/analysisnotes/epr.pdf .

[29] http://hallaweb.jlab.org/wiki/index.php/Eed_Target_Calibration_List .

[30] A. Leban, http://www.jlab.org/~miham/e05102/MeetingNo29/Andrej_TargetReport.pdf .

[31] M. Mihovilovic, http://www.jlab.org/~miham/e05102/MeetingNo30 .

[32] A. Amroun *et al.*, Nucl. Phys. **A579**, 596 (1994).

[33] L. W. Mo and Y.-S. Tsai, Rev. Mod. Phys. **41**, 205 (1969).

[34] G. Miller, Inelastic Electron Scattering at Large Angles, SLAC-R-129 (1971).

[35] S. Stein *et al.*, Phys. Rev. **D12**, 1884 (1975).

[36] K. Slifer, Karl Slifer's Ph.D thesis (2004).

[37] I. V. Akushevich and N. M. Shumeiko, J. Phys. **G20**, 513 (1994).

[38] E94010, K. Slifer *et al.*, Phys. Rev. Lett. **101**, 022303 (2008), 0803.2267.

[39] The HAPPEX collaboration, Parity-violating electroweak asymmetry in $\vec{e}$p scattering, http://hallaweb.jlab.org/experiment/HAPPEX/HAPPEXII/docs/long_happex.pdf (2004).

[40] W. Xu, Ph.D thesis, MIT (2002).

[41] G. Hoehler, Nucl. Phys. B114, 505 (1976).

[42] M. Gari and W. Krumpelmann, Phys. Lett. **B173**, 10 (1986).

[43] J. T.De Forest, Nucl. Phys. A392, 232 (1983).

[44] J. M. Laget, Phys. Lett. **B273**, 367 (1991).

[45] M. A. Miller *et al.*, Phys. Rev. Lett. **74**, 502 (1995).

[46] Jefferson Lab E95-001, W. Xu *et al.*, Phys. Rev. **C67**, 012201 (2003), nucl-ex/0208007.

[47] J. Arrington *et al.*, Phys. Rev. Lett. **82**, 2056 (1999), nucl-ex/9811008.

[48] O. Benhar *et al.*, Phys. Rev. **C44**, 2328 (1991).

[49] O. Benhar, Phys. Rev. Lett. **83**, 3130 (1999), nucl-th/9908086.

[50] E. Pace, G. Salme, and G. B. West, Phys. Lett. **B273**, 205 (1991).

[51] J. Golak, G. Ziemer, H. Kamada, H. Witala, and W. Gloeckle, Phys. Rev. **C63**, 034006 (2001), nucl-th/0008008.

[52] J. A. Caballero, T. W. Donnelly, and G. I. Poulis, Nucl. Phys. **A555**, 709 (1993).

[53] private communication with John Arrington .

[54] J. Arrington and I. Sick, Phys. Rev. **C76**, 035201 (2007), nucl-th/0612079.

[55] J. Arrington, K. de Jager, and C. F. Perdrisat, (2011), 1102.2463.

[56] Jefferson Lab Hall A, M. K. Jones *et al.*, Phys. Rev. Lett. **84**, 1398 (2000), nucl-ex/9910005.